Forschungszentrum Karlsruhe
Technik und Umwelt

Wissenschaftliche Berichte
FZKA 6020

On the Thermodynamic Efficiency of Energy Conversion During the Thermal Interaction Between Hot Particles, Water and Steam

A. Bejan, N. Dan, D. G. Cacuci, W. Schütz
Institut für Reaktorsicherheit
Projekt Nukleare Sicherheitsforschung

Juni 1998

Forschungszentrum Karlsruhe
Technik und Umwelt
Wissenschaftliche Berichte
FZKA 6020

ON THE THERMODYNAMIC EFFICIENCY OF ENERGY CONVERSION DURING THE THERMAL INTERACTION BETWEEN HOT PARTICLES, WATER AND STEAM

A. Bejan*, N. Dan*, D. G. Cacuci and W. Schütz

Institut für Reaktorsicherheit
Projekt Nukleare Sicherheitsforschung

*Duke University, Durham, North Carolina, USA

Forschungszentrum Karlsruhe GmbH, Karlsruhe

1998

Als Manuskript gedruckt
Für diesen Bericht behalten wir uns alle Rechte vor

Forschungszentrum Karlsruhe GmbH
Postfach 3640, 76021 Karlsruhe

Mitglied der Hermann von Helmholtz-Gemeinschaft
Deutscher Forschungszentren (HGF)

ISSN 0947-8620

Abstract

This is a fundamental analytical and numerical study of the thermodynamic aspects of energy conversion during the sudden thermal interaction between melt particles that are initially dispersed through a body of saturated liquid water. The study is constituted as a sequence of models that proceed from the simplest toward the more complex. In the first model it is shown that the immediate thermal contact between water and hot surface leads to high supercritical pressures, and prevents the formation of steam at the interface. The pressure decays, and steam forms as the time increases. Steam is incorporated in the second model, where each melt particle is a sphere coated by a steam annulus and immersed in water. The mixture expands in one direction, away from a plane wall, and the calculated efficiency is in the range $10^{-1} - 10^{-3}$. This conclusion is reinforced by a subsequent model, where the mixture expands in a space with cylindrical or spherical symmetry. The mixture occupies only a portion of the water volume, and expands against the remaining body of water. In the final phase of the study the heat transfer irreversibility of the process is isolated and calculated by assuming that the thermal interaction occurs in the absence of fluid motion. Exergy analysis shows that the second-law (exergetic) efficiency is approximately equal to the ratio of melt mass divided by the water mass in the local mixture, m_m/m_w, when this ratio is considerably smaller than 1. The effect of fluid motion and fluid-flow irreversibility is included in the final model, which accounts for the escape of the expanding mixture through cracks in the confining vessel. Overall, the study shows how the heat-transfer irreversibility reduces the efficiency to values much smaller than 1, and places a new emphasis on the local measurement of the mass ratio m_m/m_w in future experimental studies.

Zum thermodynamischen Wirkungsgrad der Energiekonversion während der thermischen Wechselwirkung zwischen heißen Partikeln, Wasser und Dampf

Zusammenfassung

Es handelt sich bei der vorliegenden Arbeit um eine fundamentale analytische und numerische Untersuchung der thermodynamischen Aspekte der Energiekonversion bei einer plötzlichen thermischen Wechselwirkung von heißen Schmelzepartikeln, die in der Anfangsphase mit einer Vorlage von gesättigtem Wasser vermischt sind. Die Untersuchung ist aufgebaut als eine Folge von Modellen, die vom einfachsten Fall bis zu komplexen Fällen fortschreitet. Im ersten Modell wird gezeigt, daß der plötzliche thermische Kontakt zwischen Wasser und heißer Oberfläche zu hohen superkritischen Drücken führt und so die Dampfbildung in der Wechselwirkungszone verhindert. Der Druck fällt dann ab, und es kommt zur Dampfbildung mit zunehmender Zeit. Im zweiten Modell ist der Dampf bereits enthalten; hier wird jede Schmelzepartikel dargestellt als eine von einem Dampffilm umgebene Kugel innerhalb der Wasservorlage. Die Mischung expandiert in eine Richtung, weg von einer ebenen Wand, und der berechnete Wirkungsgrad liegt im Bereich von 10^{-1} bis 10^{-3}. Dieses Ergebnis wird untermauert durch ein weiteres Modell, bei dem die Mischung räumlich in Zylinder- oder Kugelgeometrie expandiert. Hierbei füllt die Mischung nur einen Teil des Wasservolumens aus und expandiert gegen die verbleibende Wassermenge. In der abschließenden Phase der Untersuchung wird die Irreversibilität des Wärmeübergangs bei diesem Prozeß gesondert betrachtet und zunächst unter der Annahme berechnet, daß die thermische Wechselwirkung ohne Bewegung der Flüssigkeit erfolgt. Eine Exergie-Analyse zeigt, daß der exergetische Wirkungsgrad (Wirkungsgrad der Energiekonversion) nach dem 2. Hauptsatz näherungsweise gleich ist dem Verhältnis aus Schmelzemasse und Wassermasse in der lokalen Mischungszone m_m/m_w, falls dieses Verhältnis deutlich kleiner ist als 1. Der Effekt der Flüssigkeitsbewegung und der Irreversibilität des Flusses ist im abschließenden Modell berücksichtigt; dies ist von Bedeutung für das Ausströmen der expandierenden Flüssigkeit durch Risse in dem umschließenden Behälter. Insgesamt zeigt die vorliegende Untersuchung, wie die Irreversibilität des Wärmeüberganges den Wirkungsgrad der Energiekonversion auf Werte reduziert, die erheblich kleiner als 1 sind. Erneut wird die Notwendigkeit betont, daß bei zukünftigen Experimenten das lokale Massenverhältnis m_m/m_w bestimmt werden sollte.

Contents

1 Introduction 1

2 Interaction between a hot surface and water at supercritical pressures 2
  2.1 Phenomenological model 2
  2.2 Mathematical model 6
  2.3 Numerical method 8
  2.4 Results 13
  2.5 Closing Comments 19

3 Expansion of a mixture of hot particles, steam and liquid water 21
  3.1 Mathematical formulation 21
  3.2 Numerical method 27
  3.3 Energy conversion 31
  3.4 Discussion 33

4 Evolution of a finite-size mixture immersed in a water pool 40
  4.1 Mathematical formulation 40
  4.2 Method of solution 42
  4.3 Results in cylindrical coordinates 45
  4.4 Energy conversion 49
  4.5 One-dimensional configurations 53
  4.6 Closing comments 54

5 Irreversibility due to sudden heat transfer in a stationary mixture 55
  5.1 Model 58
  5.2 Efficiency 59
  5.3 The small melt fraction limit 64
  5.4 The effect of the choice of dead state 66
  5.5 The effect of melt superheat 68

6 Efficiency of melt-water interaction when the mixture expands with flow resistance 70
  6.1 Model 70
  6.2 Solution 72
  6.3 Efficiency 73
  6.4 Results 74

7 Conclusions 75
  Publications 87
  References 87

List of Figures

1 The interface between molten material and water under the assumption that a steam layer (δ) is present. 3

2 Spherically symmetric model of molten material surrounded by single-phase water at supercritical pressures. 5

3 (a) Boundary condition treatment in the case of ideal gas and Riemann invariants. (b,c) The ghost cell and the staggered grid for the Roe upwind approximate Riemann solver. 10

4 The water pressure (a), temperature (b), radial velocity (c) and density (d) distributions in the vicinity of the hot surface (R_S = 10 mm, ideal gas, spherical coordinates). 14

5 The pressure history at the surface (R_S = 10 mm, ideal gas, spherical coordinates), and the effect of the initial interface pressure. 15

6 The effect of the system size (R_S) on the water pressure, temperature, velocity and density distributions (ideal gas, $\bar{t}$ = 0.0874). 16

7 The effect of the system size on the pressure history at the surface (ideal gas). 17

8 The water pressure (a), temperature (b), radial velocity (c) and density (d) distributions in the vicinity of the hot surface (R_S = 10 mm, real gas, cartesian coordinates). 18

9 Comparison between real-gas and ideal-gas simulations with R_S = 10 mm in cartesian coordinates. 20

10 Comparison between the real-gas and ideal-gas simulations of the pressure history at the surface (R_S = 10 mm, cartesian coordinates). 21

11 (a) Spherical elemental system and (b) time when adjacent steam layers touch. 22

12 One-dimensional layer occupied by the expanding mixture. 24

13 The four-layer structure of the elemental system of Fig. 11a. 25

14 The effect of the assumed constant pressure $\tilde{P}$ on the history of the outer steam radius, for the dimensions listed in Table 1. 26

15 The steam-water interface velocity in the elemental system of Fig. 14. 30

16 The heat released by the molten material in the elemental system of Fig. 14. 31

17 The mixture density history corresponding to the elemental system (Fig. 14). 32

18 The evolution of the local mixture velocity. 34

19 The effect of the mass fraction of molten material on the evolution of the thickness of the one-dimensional mixture layer. 35

20 The effect of the mass fraction of molten material on the kinetic energy of the mixture sample of initial volume L_0^3. 35

21 The effect of the mass fraction of molten material on the energy conversion efficiency. 36
22 The effect of the thickness of the mixture layer on the energy conversion efficiency. 36
23 The effect of the size of the molten droplet on the evolution of the thickness of the mixture layer. 37
24 The effect of the size of the molten droplet on the energy conversion efficiency. 38
25 The effect of the assumed constant elemental pressure on the energy conversion efficiency. 39
26 Two-dimensional space in which a cylindrical mixture volume is immersed in a water pool. 41
27 The time-evolution of the mixture density. 46
28 The triangular meshes tried (a, c, d), and the one used (b). 48
29 The deformed mesh at the time t = 4 ms, for $r_m = 0.5$ mm, $R_m = 10$ mm, $H_m = 10$ mm, $R_p = 40$ mm and $H_p = 40$ mm. 49
30 The velocity distribution in the mixture and water domain when the steam annuli touch (Fig. 11b). 50
31 The velocity potential (top) and velocity vector (bottom) for the state described in Fig. 30. 51
32 The time-evolution of the total kinetic energy. 52
33 The time-evolution of the heat released from one hot sphere. 54
34 The energy conversion efficiency for the systems described by Figs. 30-33. 55
35 The effect of the size of the water pool on the energy conversion efficiency. 56
36 One-directional configurations: (a) vertical expansion, and (b) radial expansion. 56
37 The effect of water pool size on efficiency in the configuration of Fig. 36a. 57
38 The effect of mixture volume size on efficiency in the configuration of Fig. 36b. 57
39 The constant-volume mixing of specified amounts of water (m_w) and molten material (m_m). 59
40 The temperature variation at constant density in compressed liquid water. 60
41 The pressure variation at constant density in compressed liquid water. 61
42 The entropy variation at constant density in compressed liquid water. 62
43 The specific internal energy of liquid water in the final state (e), as a function of the mass ratio. 63
44 The exergetic efficiency as a function of the mass ratio. 64
45 The effect of the choice of dead state temperature on the exergetic efficiency. 67
46 Accuracy test for the efficiency formula (138). 69

47 The small effect of the melt superheat ($T_i > T_m$) on the exergetic efficiency. 69
48 Model of expanding melt-water mixture with flow resistance at the outlet. 71
49 The ejection velocity as a function of time and hot particle size. 76
50 The specific kinetic energy as a function of time and hot particle size. 76
51 The energy conversion efficiency as a function of time and hot particle size. 77
52 The effect of the mass fraction on the ejection velocity. 77
53 The effect of the mass fraction on the specific kinetic energy. 78
54 The effect of mass fraction on the mixture temperature. 78
55 The effect of the mass fraction on the mixture pressure. 79
56 The effect of the mass fraction on the energy conversion efficiency. 79
57 The effect of the area reduction ratio on the ejection velocity. 80
58 The effect of the area reduction ratio on the specific kinetic energy. 80
59 The effect of the area reduction ratio on the mixture pressure. 81
60 The effect of the area reduction ratio on the energy conversion efficiency. 81
61 The effect of the system size on the ejection velocity. 82
62 The effect of the system size on the specific kinetic energy. 82
63 The effect of the system size on the mixture pressure. 83
64 The effect of the system size on the energy conversion efficiency. 83
65 Model in which the water content expands isentropically and adiabatically beyond the thermal mixing modeled in Fig. 39. 85
66 The energy conversion efficiency according to the model of Fig. 65. 86

Nomenclature

a	function, Eq. (148)
a	constant, N / m^2K
a_1, a_2, a_3	functions, Eq. (57)
A	area, m^2
$\mathbf{A}$	Jacobian matrix, Eq. (20)
A, A_1, B, C, D, E	dimensionless groups, Eqs. (56), (59)–(61) and (64)
$\bar{\mathbf{A}}$	Roe averaged matrix, Eqs. (21, 22)
b	constant, Eq. (150)
B	base length, m
B	dimensionless group, Eq. (4)
B	limiter function, Eqs. (27, 28)
c	constant, Eq. (154)
c	speed of sound, m/s
c_p	specific heat at constant pressure, J/ kg K
$\bar{c}_m$	equivalent specific heat, Eq. (118)
e	specific energy, J / kg
e_t	specific total energy, J / kg
$\tilde{e}$	energy per unit volume, $\bar{\rho}\,\bar{e}$
$\mathbf{F}$	flux vector, Eq. (11)
h	heat transfer coefficient, W/m^2K
h	specific enthalpy, J / kg
h_{fg}	latent heat of vaporization, J / kg
h_{sf}	latent heat of solidification, J / kg
h_t	specific total enthalpy, J / kg
H_m	mixture height, m
H_p	pool height, m
k	thermal conductivity, W / m K
k_m	steam thermal conductivity evaluated at T_m
k_s	solid thermal conductivity, W / m K
k_v	vapor thermal conductivity, W / m K
$\tilde{K}$	specific exergy factor, Eq. (137)
KE	mixture kinetic energy inventory, Eqs. (65) and (156)
KE_l	kinetic energy per unit mass of mixture, Eq. (159)
L	mixture layer thickness, m
L_0	initial mixture layer thickness, m
L_2	euclidean norm
m	mixture mass sample, kg

m_m	mass of molten material, kg
m_m	mass of one molten sphere, kg
m_s	mass of steam
m_w	mass of liquid water, kg
m_{w0}	initial mass of water, kg
M	dimensionless water mass, Eq. (150)
n_{el}	number of finite elements adjacent to each node
N	number of elemental systems
N_a	shape (interpolation) functions
$\tilde{p}$	pressure ratio, Eq. (150)
P	pressure, bar
P_i	interfacial pressure, bar
P_0	atmospheric pressure, bar
q	heat transfer rate, Eqs. (60, 61)
q_{cond}	conduction heat transfer rate
q_{rad}	radiation heat transfer rate, Eq. (60)
q''	heat flux, $W / m^2 K$
Q	heat released by molten material, Eqs. (66, 68)
$\mathbf{Q}$	vector, Eq. (11)
r	radial direction, Fig. 13
r_c	radius of finite element, m
r_m	radius of melt droplet, m, Fig. 11
r_s	outer radius of steam annulus, m, Fig. 11
R	outer radius, m
R	ideal gas constant, J/ kg K
R_m	radius of mixture domain, m
R_p	pool radius, m
R_s	surface radius, m
R_v	ideal gas constant of steam, J / kg K
s	specific entropy, J/kg K
S	source term
$\bar{S}$	geometry parameter, Eq. (13)
t	time, s
T	temperature, K
T_m	hot surface temperature, K
T_m	solidification temperature, K
T_0	saturation temperature at P_0, K
T_s	saturation temperature, K

T_s	surface temperature, K
T_s	temperature of steam-water interface, K
u	radial velocity, m/s
u	specific energy, J/kg
v	specific volume, m^3/kg
v_{fg}	specific volume change during vaporization, m^3 / kg
v_r	radial velocity, m/s
v_z	axial velocity, m/s
V	velocity, m/s
V	volume of mixture sample
V_m	volume of molten material
V_s	volume of steam
V_w	volume of liquid water
W	work, J
x	cartesian coordinate, Fig. 1
$\mathbf{X}$	matrix of right-side eigenvalues, Eq. (25)
γ	ratio of specific heats, c_p / c_v
δ	steam thickness, m
$\Delta\mathbf{Y}$	vector, Eq. (26)
ε	mass fraction of molten material
ε_m	melt surface emissivity
ε_s	emissivity of the steam-water interface
η	conversion efficiency
θ	temperature ratio, Eq. (148)
κ	pressure derivative, Eq. (33)
λ	solid thickness, m
λ_j	eigenvalues
μ	adjusted mass ratio, Eq. (124)
ξ	specific nonflow exergy, J/kg
Ξ	nonflow exergy, J
π	product, Eq. (12)
ρ	density, kg / m^3
ρ_m	density of hot material, kg/ m^3
ρ_0	water density at P_0 and T_0, kg / m^3
ρ_s	solid density, steam density, kg / m^3
ρ_v	vapor density, kg / m^3
ρ_w	water density, kg/ m^3
$\bar{\rho}_s$	volume averaged density of steam

σ	area reduction ratio
σ	Stefan-Boltzmann constant, Table 1
$\bar{\sigma}$	product, Eq. (12)
τ	dimensionless time, Eq. (148)
τ_e, τ_i	temperature ratios, Eq. (124)
Φ	velocity potential function
Φ_t	time derivative of Φ
χ	pressure derivative, Eq. (33)
$\overline{(\ )}$	cell averages
$\overline{(\ )}$	dimensionless variables, Eqs. (15) - (16)
$(\ )_e$	equilibrium
$(\ )_i$	initial
$\overset{\frown}{(\ )}$	Roe averages
$(\tilde{\ })$	dimensionless variables, Eqs. (51), (52), (56), (61), (64) and (68).
$(\ )_L$	left
$(\ )_m$	melt
$(\ )_s$	solid, steam
$(\ )_*$	dead state
$(\ )_R$	right

1 INTRODUCTION

The sudden contact between two liquids at markedly different temperatures (e.g. water in contact with a molten metal, molten salt, magma, or oil) is a problem of fundamental importance in engineering and the environment [1]. In particular, this problem is relevant to the study of hypothetical accidents in light water nuclear reactors: according to a scenario in which the flow of cooling water to the reactor core is interrupted, the fuel and cladding could melt, and the molten material could flow into the reactor cavity where it could come into direct contact with water. The interaction between a very hot material and water is of great interest because it may trigger and energize steam explosions [2] that can cause containment failure with subsequent release of radioactivity into the environment.

Reviews of current progress in this research field are provided by Corradini et al. [3] and Berthoud [4]. According to the scenario described by Berthoud [4], for a large scale steam explosion to occur the molten material must first mix coarsely with the coolant (water). This "premixing" phase is characterized by a time scale of 1s and a melt length scale of 1cm. In the second phase, the premixed state may be destroyed by a sudden event (a trigger), leading to a fine fragmentation and dispersion of the molten material. This sudden thermal contact is accompanied by rapid heat transfer, pressurization, wave propagation, and expansion.

The work described in this report was conducted in three distinct phases. In the first, we focused on the sudden interaction of a small droplet of the finely fragmented molten material and water. The main objective was to determine the pressure and time scales of the thermal and mechanical effects, and the time-evolution of the interaction in the earliest stages. This work is described in Section 2.

In the second phase, we considered a one-dimensional layer containing a uniform mixture of fine hot particles, steam and liquid water. The mixture expands because of the volumetric generation of steam. At the same time, the mixture is accelerated away from the surfaces with which it comes in contact. The mixture is modeled as a conglomerate of spherical drops of molten material that are distributed uniformly throughout a finite-size body of water. Steam annuli develop around the spherical drops as time increases. The focus of this study was on the efficiency of energy conversion during the expansion of the mixture (Section 3).

We continued the study of expanding melt-and-water mixtures by conducting numerical simulations in three additional geometries (Section 4): cylindrical mixture volume immersed in a cylindrical water pool, plane mixture layer held under a layer of pure water, and hemispherical mixture volume at the bottom of a much larger water pool. The objective was to document the relation between the conversion efficiency, the various dimensions of the system (particles, mixture volume, water pool), and the directions in which the mixture expands.

One result that emerges several times in Sections 3 and 4 is that the conversion efficiency is generally low, in the 10^{-3}–10^{-2} range. The time and motion (expansion) scales are also small. This led to redefining the melt-water interaction problem in Section 5: we assumed that the mixture does not move, hence all the irreversibility is due to the transfer of heat across large temperature differences. In this third phase of our work we used the method of exergy analysis, and were able to verify further the origin of the low efficiencies determined numerically in the second phase.

2 INTERACTION BETWEEN A HOT SURFACE AND WATER AT SUPERCRITICAL PRESSURES

2.1 Phenomenological Model

The first step in the modeling of the thermal interaction between molten material and water is to assess whether a vapor film (steam) is present from the beginning between the solidifying material and the liquid water. For this purpose, consider the one-dimensional geometry shown in Fig. 1, where molten material at the solidification temperature (T_m) makes contact at the time $t = 0$ with a body of water at atmospheric pressure (P_0) and saturation temperature (T_0). During the first infinitesimal time step Δt, the material develops a solid crust of thickness λ. The next step is to examine if during Δt the water space develops a thin layer of vapor of thickness δ.

Energy conservation requires that the latent heat of solidification released by the molten material during Δt be matched by the latent heat of vaporization of water, i.e.,

$$\rho_s \, h_{sf} \, \lambda = \rho \, h_{fg} \, \delta, \tag{1}$$

where h_{sf} and h_{fg} are the latent heats of the material (solidification) and, respectively, water (evaporation). At the very beginning, i.e., at $t = 0^+$, the temperature distribution is linear across both λ and δ, so the continuity of heat through the solid-vapor interface is

$$k_s \frac{T_m - T_s}{\lambda} = k_v \frac{T_s - T_0}{\delta}, \tag{2}$$

where k_s and k_v are the thermal conductivities of the solid material and steam. The solid-vapor surface temperature T_s is obtained by eliminating the ratio λ / δ from Eqs. (1) and (2); this leads to

$$\frac{T_s}{T_0} = \frac{1 + B\, T_m / T_0}{1 + B}, \tag{3}$$

where B is the dimensionless group of properties

$$B = \frac{k_s \rho_s h_{sf}}{k_v \rho h_{fg}}. \qquad (4)$$

The order of magnitude of B is found by substituting in Eq. (4) the properties of the solidified material and water. The molten material consists approximately of a mixture of $Al_2 O_3$ (87% by weight), FeO (5%), MgO (5%) and Fe (3%), cf. Huber et al. [5], with the following properties: ρ_s = 3770 kg / m^3, h_{sf} = 1090 kJ / kg at T_m = 2313 K, and k_s = 6 W / m K. For the properties of water we take ρ = 1000 kg / m^3, h_{fg} = 2260 kJ / kg at T_0 = 373 K, and k_v = 0.1 W / m K (steam at 1000 K). Substituting these values into Eq. (4) shows that B = 109 >> 1. Using this value of B in Eq. (3) leads to the conclusion that the interface temperature is essentially the same as the solidification temperature, $T_s = 2295 \text{ K} \cong T_m$.

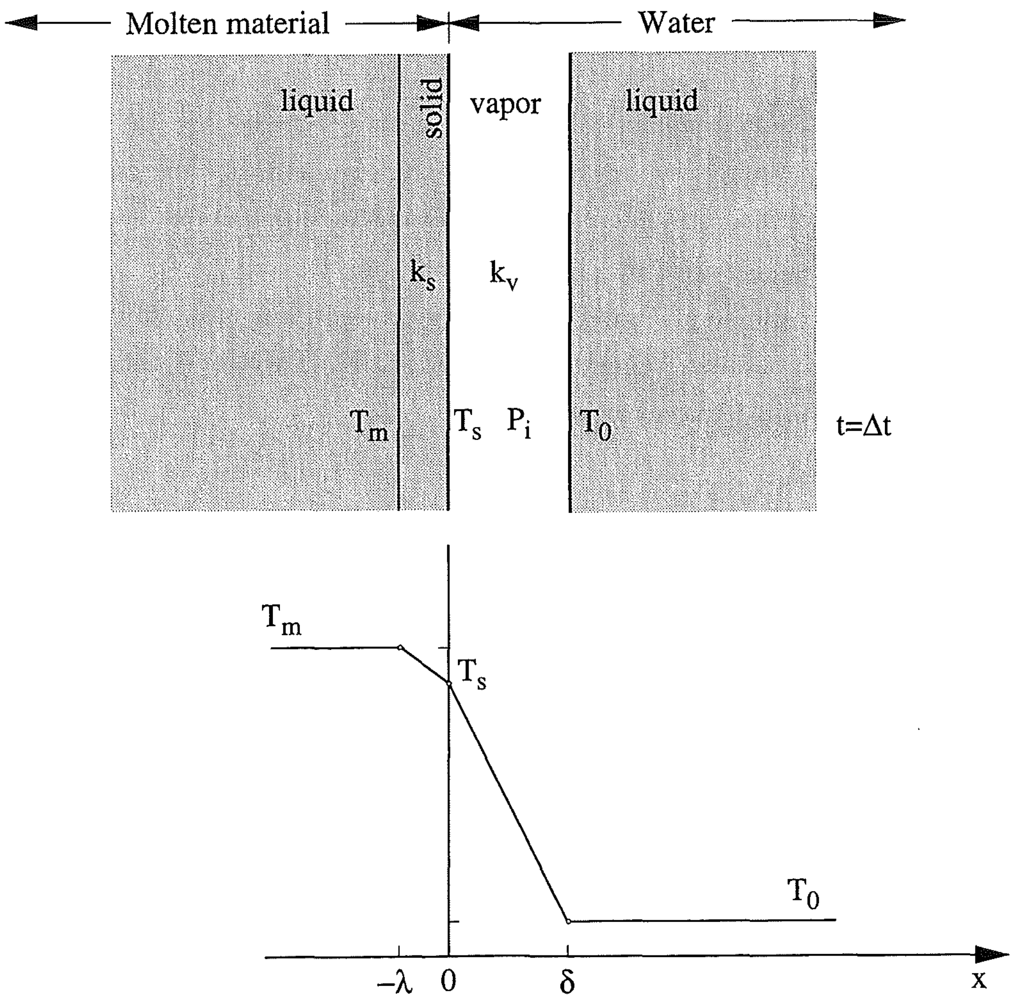

Figure 1. The interface between molten material and water under the assumption that a steam layer (δ) is present.

To estimate the initial interface pressure P_i, we note that at $t = 0^+$ (i.e., before the body of water moves to the right in Fig. 1) the steam layer of thickness δ must contain the same mass as a liquid water layer of thickness δ

$$\int_0^\delta \rho_v(x)\, dx = \rho\delta. \tag{5}$$

On the left side of this equation we model the steam as an ideal gas, $\rho_v = P_i / R_v T(x)$ with $R_v = 0.46$ kJ / kg K, and with linear temperature distribution

$$T(x) = T_s - (T_s - T_0)\frac{x}{\delta}. \tag{6}$$

Equations (3) through (6) can be combined to obtain

$$P_i = \rho\, R_v (T_m - T_0) \frac{B}{1+B} \ln\left(\frac{1 + BT_m / T_0}{1+B}\right). \tag{7}$$

Substituting the respective numerical values into Eq. (7) yields $P_i = 1.6 \times 10^4$ bars. This pressure estimate is almost two orders of magnitude greater than the critical pressure of water (221 bars) and therefore invalidates the original assumption that at $t = 0^+$ the surface of the molten material is coated by a layer of steam (Fig. 1).

The preceding estimate of P_i was based on the simplifying assumption that the steam-water interface temperature remains at $T_{sat} = 373$ K. If we relax this assumption and account for the Clausius - Clapeyron relation

$$\frac{dP_i}{dT_{sat}} = \frac{h_{fg}}{T_{sat} v_{fg}}, \tag{8}$$

then T_{sat} will rise as the steam pressure rises. Linearizing Eq. (8) by setting $h_{fg} / (T_{sat}\, v_{fg}) = a$ (where a = constant) and integrating the resulting expression leads to

$$P_i - P_0 \cong a (T_{sat} - T_0), \tag{9}$$

where $a \cong 0.0026$ bars/K and $T_0 = 373$ K. Furthermore, we may assume that $P_i \gg P_0$ and therefore neglect P_0 on the left side of Eq. (9). Eliminating P_i between Eqs. (7) and (9) yields a transcendental equation for T_{sat} that can be solved numerically to obtain $T_{sat} = 1890$ K. The steam pressure P_i that corresponds to this value of T_{sat} is approximately 400 bars, cf. Eqs. (7) or (9). Once again, the interface pressure is supercritical, which shows that the assumption made so far, cf. Fig. 1, is physically implausible.

The preliminary analysis presented above suggests the model shown in Fig. 2. This model no longer contains steam at the interface between the solidifying material and water. The interfacial water is initially single-phase liquid, and, because of mass conservation [c.f., Eq. (5)] its pressure is initially supercritical but then decays in time, as the liquid water is accelerated outward.

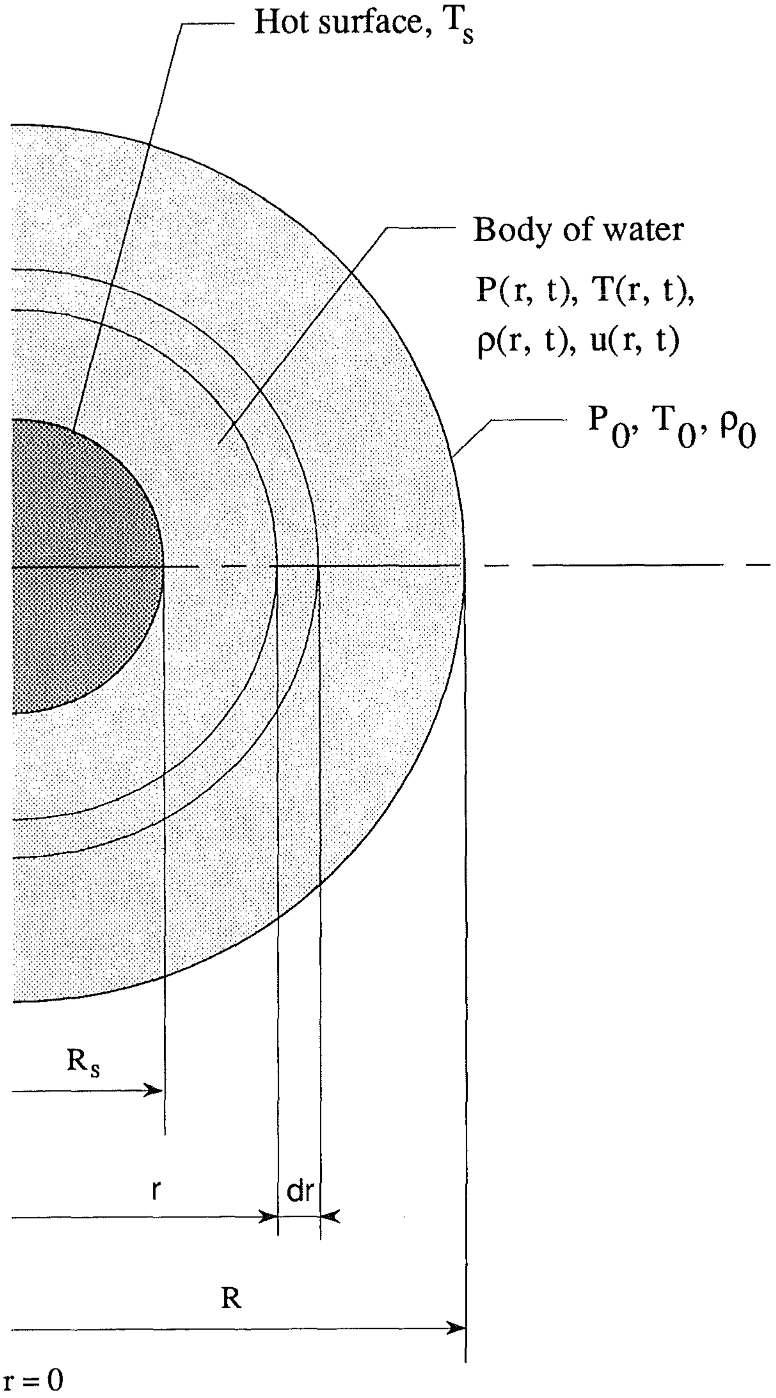

Figure 2. Spherically symmetric model of molten material surrounded by single-phase water at supercritical pressures.

Although Fig. 2 depicts a spherically symmetric geometry, the mathematical model described in the next section covers not only this geometry but also the plane (cartesian) geometry depicted in Fig. 1. The molten material (liquid and solid) is assumed isothermal at the constant temperature $T = T_s$ of the interface $r = R_s$. At the time $t = 0$, the surface makes contact with a body of water of outer radius R at atmospheric pressure P_0 and saturation temperature T_0. The water remains a single-phase liquid throughout the time-dependent heat and fluid flow processes modeled in the following.

2.2 Mathematical Model

The dimensionless equations for the conservation of mass, momentum and energy in cartesian or spherical coordinates are

$$\frac{\partial \mathbf{Q}}{\partial \bar t} + \frac{\partial \mathbf{F}}{\partial \bar r} = 0, \tag{10}$$

where

$$\mathbf{Q} \equiv \begin{bmatrix} \bar\sigma \\ \bar\sigma\,\bar u \\ \bar\sigma\,\bar e_t \end{bmatrix}; \qquad \mathbf{F} \equiv \begin{bmatrix} \bar\sigma\,\bar u \\ \bar\sigma\,\bar u^2 + \bar\pi \\ \bar\sigma\,\bar u\,\bar h_t \end{bmatrix}, \tag{11}$$

$$\bar\sigma \equiv \bar\rho\,\bar S; \qquad \bar\pi \equiv \bar P\,\bar S; \tag{12}$$

and where $\bar S$ is defined as,

$$\bar S = \begin{cases} 1, \text{ for cartesian coordinates} \\ \bar r^2, \text{ for spherical coordinates} \end{cases} \tag{13}$$

In the momentum equation, $\bar u$ represents the dimensionless radial velocity of the water. In the energy equation, $\bar e_t$ and $\bar h_t$ represent the total specific energy and the total enthalpy, respectively, i.e.,

$$\bar e_t = \bar e + \frac{1}{2}\bar u^2; \qquad \bar h_t = \bar e_t + \frac{\bar P}{\bar\rho}. \tag{14}$$

The dimensionless variables appearing in Eqs. (11) through (14) are defined as follows:

$$\bar r \equiv \frac{r}{R_s}; \qquad \bar R \equiv \frac{R}{R_s}; \qquad \bar u \equiv \frac{u}{(P_0/\rho_0)^{1/2}}; \qquad \bar t \equiv \frac{t}{R_s}\left(\frac{P_0}{\rho_0}\right)^{1/2}; \tag{15}$$

$$\bar h_t \equiv \frac{h_t}{(P_0/\rho_0)^{1/2}}; \qquad \bar\rho \equiv \frac{\rho}{\rho_0}; \qquad \bar T \equiv \frac{T}{T_0}; \qquad \bar P \equiv \frac{P}{P_0}. \tag{16}$$

In Eqs. (15) and (16), ρ_0 is the water density at the outer radius R (where, by assumption, $P = P_0$ and $T = T_0$).

Equations (10) and (11) have the same form as the quasi-one-dimensional homogeneous Euler equations for flow through a channel of non-constant cross-section $\bar{S}$, written in conservative form [6]. The quantities of interest for our phenomenological model are the pressure, density, and velocity waves that propagate away from the interface. Since these waves involve time scales that are much shorter than the time scales for viscous and diffusion effects, the latter can be neglected. Thus, in the momentum equation, the viscous diffusion terms are neglected in accordance with the numerical study of Huang and Bau [7]. Furthermore, the thermal diffusion terms are neglected in the energy equation everywhere except at the R_s interface.

The initial conditions state that the interface is isothermal and the water body is motionless and isobaric at $\bar{t} = 0$, i.e.,

$$\begin{aligned} \bar{T} &= \bar{T}_s, && \text{at } \bar{t} = 0 && \text{and} && \bar{r} = 1; \\ \bar{u} &= 0, && \text{at } \bar{t} = 0 && \text{and} && 1 < \bar{r} < \bar{R}; \\ \bar{P} &= \bar{P}_i, && \text{at } \bar{t} = 0 && \text{and} && \bar{r} = 1; \end{aligned} \qquad (17)$$

where $\bar{P}_i$ is the initial interface pressure whose numerical value of 1.28×10^4 is discussed in the opening paragraph of the next section. The corresponding boundary conditions are

$$\begin{aligned} \bar{T} &= \bar{T}_s, && \text{at} && \bar{r} = 1; \\ \bar{T} &= 1, && \text{at} && \bar{r} = \bar{R}; \\ \bar{u} &= 0, && \text{at} && \bar{r} = 1 \text{ and } \bar{r} = \bar{R}; \\ \bar{P} &= 1, && \text{at} && \bar{r} = \bar{R}; \end{aligned} \qquad (18)$$

The isothermal surface condition at $\bar{r} = 1$ is justified by the numerical example given after Eq. (4), which showed that the interface temperature is not changed appreciably by the sudden contact with water. As we will show in section 2.4 , this condition is also justified by the brevity of the process simulated numerically, because during such a short time ($\sim 10^{-6}$ s) the solidification of the molten material ($\bar{r} < 1$) is insignificant.

2.3 Numerical Method

Our numerical work was guided by the literature on the simulation of heat and fluid flow in compressible fluids such as water at supercritical pressures. A general reference on the mathematical formulation involving real gas effects is Melnikoff and Plohr [8]. For example, Steiner and Gretler [9] studied the propagation of spherical and cylindrical shock waves in real gases. For the real gas model they used an equation of state in a general form, and in the numerical method they relied on the method of characteristics. Glaister [10] studied the flow of a real gas through a duct with variable cross-section by using an equation of state and an upwind scheme. Huang and Bau [7] described the propagation of planar thermoacoustic waves in a semi-infinite medium by using a linearized model in the limit of small perturbations. Related studies were conducted by Drikakis and Tsangaris [11], Murakami and Imashita [12], and Toumi [13].

The problem is initialized by assuming that an infinitesimally thin layer of heated water at supercritical pressure is formed at the interface before any wave propagation begins. The initial interface pressure $\bar{P}_i$ follows from an analysis identical to the one presented in Eqs. (5) through (7) except that this time the heated "gas" layer is considered to contain water at supercritical pressure and at a temperature near T_s. These considerations yield $\bar{P}_i = 1.28 \times 10^4$, and this value was used as the initial interface pressure for most of the numerical calculations reported here. The effect of using a different $\bar{P}_i$ value was also investigated (Fig. 5). The need to state the pressure condition is a characteriistic of the present model: if the effect of thermal diffusion were included in the model then the initial pressure could be computed as a part of the solution process, as shown by Huang and Bau [7]. We could not use the same method as Huang and Bau, because their approach was suited for a linear model and small pertubations. The present model is nonlinear, and the relative changes are large.

Equations (18) indicate that two types of boundary conditions are required for the computational domain depicted in Fig. 2. The far field condition does not require special treatment. To implement the wall condition of zero velocity we used a reflective wall procedure called the "ghost cell" [6, 14]. Figures 3b and 3c shows the ghost cell at the boundary $r = R_S$, with cell R on the right (i.e., on the surface facing the water). Its mirror image, cell L, is placed to the left of the boundary, and the respective unknowns are subject to the conditions

$$\begin{aligned} u_L &= -u_R; \qquad & c_L &= c_R; \\ T_L &= \ T_R; \qquad & P_L &= P_R; \end{aligned} \tag{19}$$

In Eqs. (19), c_L and c_R are the respective speeds of sound. The lower part of Fig. 3 shows the staggered grid of the Roe scheme [15, 16], where "imax" is the total number of grid points. When the heated water layer was modeled as an ideal gas, the boundary conditions were also treated by using Riemann invariants (Fig. 3a, cf. Osher and Chakravarthy [17], Hemker and Spekreijse [18]); the solution obtained this way was practically indistinguishable from that obtained using the ghost cell method.

The literature on numerical methods for solving compressible flow problems with strong interactions recommends the use of total variation diminishing (TVD) higher order upwind schemes. There is a need for an accurate representation of the waves (i.e. less dissipation) and a robust numerical scheme that is as simple as possible. These recommendations hold not only for ideal gas simulations (with both constant and variable cross-sections [6, 15, 19, 20]), but also for real gas simulations [21-26]. We tried two such schemes for solving the Euler system (10): a TVD MacCormack scheme [6], which is simple and fast, and a TVD second order flux splitting scheme based on Roe averages.

Because of the sudden thermal contact between water and the hot surface, the TVD MacCormack scheme in spherical coordinates generates spurious oscillations of non-negligible amplitude. For this reason, we solved Eq. (10) using a second order scheme with flux limiters and approximate Riemann solvers (see, e.g., Roe [15] and Sweby [19]). Equation (10) is written in nonconservative form as

$$\frac{\partial \mathbf{Q}}{\partial \bar{t}} + \mathbf{A}\,\frac{\partial \mathbf{Q}}{\partial \bar{r}} = 0, \tag{20}$$

where $\mathbf{A}$ is the Jacobian matrix of the system. Next, we introduce Roe's averaged matrix $\bar{\mathbf{A}}$ defined through the relations

$$\mathbf{F}_R - \mathbf{F}_L = \bar{\mathbf{A}}\left(\mathbf{Q}_R - \mathbf{Q}_L\right) \tag{21}$$

and

$$\bar{\mathbf{A}} = \frac{\partial \mathbf{F}}{\partial \mathbf{Q}} \quad \text{for} \quad \mathbf{Q} = \mathbf{Q}_R = \mathbf{Q}_L \tag{22}$$

Roe's method begins with a first order upwind scheme in which the numerical flux is taken as

$$\mathbf{F}^*_{i+1/2} = \mathbf{F}_i + \left(\sum_j \mathbf{X}_j\, \boldsymbol{\Phi}_{L,j}\right)^{i+1/2} = \mathbf{F}_{i+1} - \left(\sum_j \mathbf{X}_j\, \boldsymbol{\Phi}_{R,j}\right)^{i+1/2} \tag{23}$$

where

$$\boldsymbol{\Phi}_{L,j}^{i+1/2} = \left(\lambda_j^-\, \Delta \mathbf{Y}_j\right)^{i+1/2}, \qquad \boldsymbol{\Phi}_{R,j}^{i+1/2} = \left(\lambda_j^+\, \Delta \mathbf{Y}_j\right)^{i+1/2} \tag{24}$$

In Eqs. (23) and (24) the quantitites $\mathbf{X}_j$'s form the matrix of the right-side eigenvectors and are defined by $\bar{\mathbf{A}}\,\mathbf{X}_j = \lambda_j\,\mathbf{X}_j$, so that

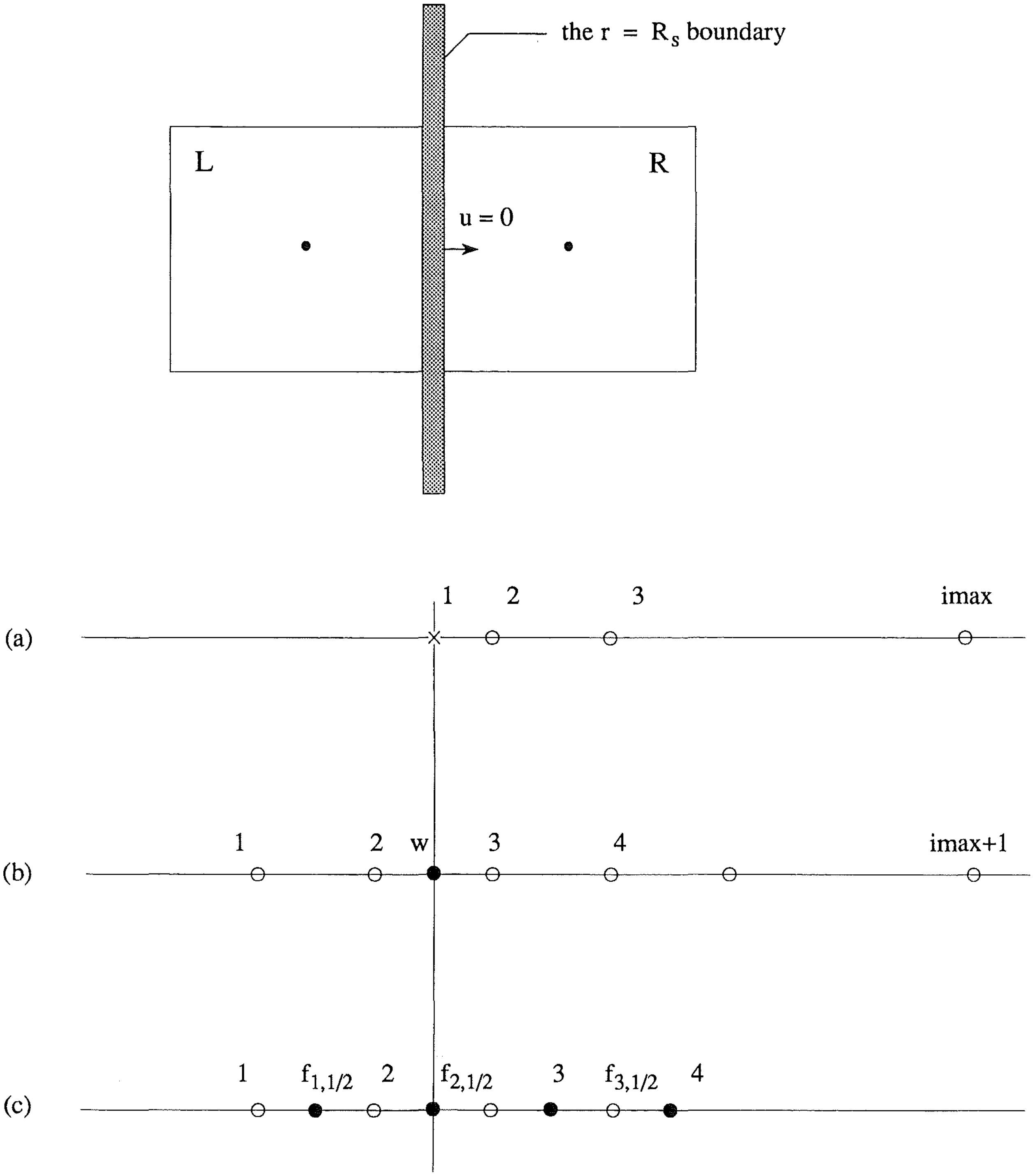

Figure 3. (a) Boundary condition treatment in the case of ideal gas and Riemann invariants. (b,c) The ghost cell and the staggered grid for the Roe upwind approximate Riemann solver.

$$\mathbf{X} = \begin{bmatrix} 1 & 1 & 1 \\ \hat{u} - \hat{c} & \hat{u} & \hat{u} + \hat{c} \\ \hat{h}_t - \hat{u}\hat{c} & K & \hat{h}_t + \hat{u}\hat{c} \end{bmatrix} \tag{25}$$

In Eq. (24) λ_j are the eigenvalues, and $\lambda_j^{\pm} = \left(\lambda_j \pm |\lambda_j|\right) / 2$ are the positive and, respectively, negative parts of the eigenvalues. The variation of the characteristic variables between the states "L" and "R" is $\Delta\mathbf{Y} = \mathbf{X}^{-1}\, \Delta\mathbf{Q}$, where

$$\Delta\mathbf{Y} = \frac{1}{\hat{c}^2} \begin{bmatrix} \frac{1}{2}\left(\Delta\bar{\pi} - \hat{\sigma}\hat{c}\Delta\bar{u}\right) \\ \hat{c}^2\, \Delta\bar{\sigma} - \Delta\bar{\pi} \\ \frac{1}{2}\left(\Delta\bar{\pi} + \hat{\sigma}\hat{c}\Delta\bar{u}\right) \end{bmatrix} \tag{26}$$

and the overbars and carets refer to cell and, respectively, Roe averages. Roe's method permits stable expansion shocks because it does not satisfy the entropy condition [6]. This feature was eliminated by using an augmented numerical diffusion for the first order scheme.

It is well known that first order accurate schemes suffer from numerical diffusion, while classical higher order schemes exhibit spurious oscillations around points of discontinuity in the solution [6, 19]. The second order TVD scheme, however, yields both high resolution and solutions without oscillations. To take advantage of these properties, we applied Roe's method to develop a second order TVD by using flux extrapolation together with the anti-diffusive flux limiters (Roe [15])

$$b_{L,j}^{i+1/2} = \frac{1}{2}\, B \left\{ \left[\left(1 - |\lambda_j| \frac{\Delta\bar{t}}{\Delta\bar{r}}\right) \Phi_{L,j}\right]^{i+3/2},\ \left[\left(1 - |\lambda_j| \frac{\Delta\bar{t}}{\Delta\bar{r}}\right) \Phi_{L,j}\right]^{i+1/2} \right\} \tag{27}$$

and

$$b_{R,j}^{i+1/2} = \frac{1}{2}\, B \left\{ \left[\left(1 - |\lambda_j| \frac{\Delta\bar{t}}{\Delta\bar{r}}\right) \Phi_{R,j}\right]^{i+1/2},\ \left[\left(1 - |\lambda_j| \frac{\Delta\bar{t}}{\Delta\bar{r}}\right) \Phi_{R,j}\right]^{i-1/2} \right\} \tag{28}$$

where B is the limiter function. We tried several limiters and found that Roe's limiters, B = max [min (|x|, 2|y|), min (2|x|, |y|), y], performed best for our problem. The second order TVD numerical flux and conservative variables [$\bar{\sigma}, \bar{\sigma}\,\bar{u}, \bar{\sigma}\,\bar{e}_t$; see vector **Q**, Eq. (11)] become:

$$\mathbf{F}^{*,\,\text{second order}}_{j,i+1/2} = \mathbf{F}^{*,\,\text{first order}}_{j,i+1/2} + \left[\mathbf{X}_j \left(b_{L,j} - b_{R,j}\right)\right]^{i+1/2} \tag{29}$$

$$\mathbf{Q}^{n+1}_{j,i} = \mathbf{Q}^{n}_{j,i} - \frac{\Delta\bar{t}}{\Delta\bar{r}} \left(\mathbf{F}^{*}_{j,i+1/2} - \mathbf{F}^{*}_{j,i-1/2}\right) \tag{30}$$

This second order TVD scheme is stable as long as the Courant - Friederich - Lewy (CFL) condition $\Delta\bar{t} < \Delta\bar{r}^2 / (|\lambda_{max}|\Delta\bar{r})$ is fulfilled (Hirsch [6]), where λ_{max} is the maximum eigenvalue and thermal diffusion was assumed negligible.

Ideal gas model. The TVD scheme was applied to two models of water behavior at supercritical pressures: ideal gas and real gas. In the ideal gas case, the quantity K in Eq. (25) was set equal to $\frac{1}{2}\hat{u}^2$. The Roe averaged matrix $\bar{\mathbf{A}}$ was constructed based on averages weighted by the square root of the densities, namely

$$\hat{\sigma} = (\bar{\sigma}_L\,\bar{\sigma}_R)^{1/2}, \qquad \hat{u} = \frac{\bar{u}_L\,\bar{\sigma}_L^{1/2} + \bar{u}_R\,\bar{\sigma}_R^{1/2}}{\bar{\sigma}_L^{1/2} + \bar{\sigma}_R^{1/2}}, \tag{31}$$

$$\hat{h}_t = \frac{\bar{h}_{t,L}\,\bar{\sigma}_L^{1/2} + \bar{h}_{t,R}\,\bar{\sigma}_R^{1/2}}{\bar{\sigma}_L^{1/2} + \bar{\sigma}_R^{1/2}}, \qquad \hat{c} = (\gamma - 1)\left(\hat{h}_t - \frac{\hat{u}^2}{2}\right). \tag{32}$$

Real gas model. The main difficulty encountered when implementing the real gas model for water is in writing the Jacobian matrix to determine the Roe-averaged state. Our approach was based on Vinokur's [21] extension of Roe's method for real gases. The equation of state to be specified is $\bar{P} = \bar{P}(\bar{\rho}, \tilde{e})$, where $\tilde{e} = \bar{\rho}\,\bar{e}$ is the internal energy per unit volume. We used the derivatives

$$\chi = \left(\frac{\partial\bar{P}}{\partial\bar{\rho}}\right)_{\tilde{e}}, \qquad \kappa = \left(\frac{\partial\bar{P}}{\partial\tilde{e}}\right)_{\bar{\rho}} \tag{33}$$

and expressed the speed of sound in terms of χ, κ and the specific enthalpy $\bar{h}$,

$$\bar{c}^2 = \chi + \kappa\,\bar{h}, \qquad \bar{h} = \frac{1}{\bar{\rho}}(\tilde{e} + \bar{P}) \tag{34}$$

Finally, in Eq. (25) we substituted $K = \hat{u}^2 / 2 - \hat{\chi} / \hat{\kappa}$, where the carets denote Roe's averaged state.

For the equation of state we used data interpolated from steam tables [27]. It is known that the discontinuous changes that occur in the vicinity of the liquid-vapor interface require a careful selection of the interpolation procedure. For example, using tensor product splines (for spline under tension [28]) to interpolate over the entire ranges of pressure and temperature becomes too expensive when the interpolation procedure is called often in the code. Therefore we used a local monotonic interpolation method [29, 30] to eliminate any possible oscillation, or to preserve the local monotonicity of the data interpolated. This algorithm constructs a C^1 monotonic piecewise cubic interpolant for monotonic data. The thermodynamic properties we interpolated this way were ρ = ρ(P, T), h = h(P, T), s = s(P, T) and c = c(P, T).

The TVD numerical scheme provides values for the conservative variables **Q**, rather than the primitive variables density, velocity and pressure. The pressure and temperature were computed at each time step by solving a system of nonlinear equations using a continuation method [31, 32]. Convergence tests were conducted by varying the number of spatial steps (divisions, mesh size) under the stability restriction CFL = 0.95 imposed by the numerical scheme, where $\mathrm{CFL} = |\lambda_{max}|\Delta\bar{t}/\Delta\bar{r}$. For example, in the case of $R_s = 10$ mm in spherical coordinates, the calculated time $\bar{t}$ when the interfacial pressure reached the critical pressure was 0.0722, 0.0874 and 0.0853 as imax was set equal to 100, 200 and, respectively, 500. The results reported in this paper were obtained using imax = 200, for which the physical size of Δr falls in the range 2.5 - 5 μm.

We tested the code for one-dimensional calculations of the Riemann problem with different initial data (cf. Hirsch [6]). Furthermore, in the limit of small perturbations, i.e. when the surface temperature was sufficiently low, we found that the results are qualitatively consistent with the simulations reported recently by Huang and Bau [7]. The code was run on a Silicon Graphics Indigo Station 4010.

2.4 Results

We simulated numerically the time-dependent water pressure, temperature, radial velocity and density in the vicinity of the hot surface. Starting with the ideal gas formulation, we carried out the numerical simulations for the heat and fluid flow process as long as the interfacial water layer remained a single phase liquid above the critical pressure. The following values were kept fixed in all the simulations: $T_s = 2300$ K, $T_0 = 373$ K, $P_0 = 10^5$ N/m^2, $P_i = 1.28 \times 10^9$ N / m^2, $R_v = 0.46$ kJ / kg K and $\gamma = 1.4$.

Ideal gas model. Figure 4 shows a representative sample of the numerical results obtained in spherical coordinates for $R_s = 10$ mm. The pressure distribution (Figure 4a) shows that the surface pressure decreases in time as the thickness of the pressurized water layer increases. The pressure curve for $\bar{t} = 0.0874 \left(\text{or } t = 2.1 \times 10^{-6}\ \text{s}\right)$ corresponds to the moment when the interface pressure ($\bar{P}$ at $\bar{r} = 1$) reaches the critical pressure ($\bar{P} = 221$).

The pressure decay phenomenon is accompanied by the formation of a high temperature wave that propagates outward (Fig. 4b) creating a layer of colder water behind it. The velocity profile is nearly triangular (Fig. 4c), with a peak that corresponds roughly to the radial position of the temperature wave. The velocity maximum increases in time. The density (Fig. 4d) is relatively high in the entire pressurized layer. The density maximum decays in time and propagates outward: its radial position is approximately the same as that of the $\bar{T}$ and $\bar{u}$ maxima.

Figure 5 reviews the pressure history at the surface $\bar{r} = 1$, showing again that the pressure decays very rapidly initially, and that the approach to the critical pressure is considerably more gradual. The curves are terminated when $\bar{P}$ is equal to the critical

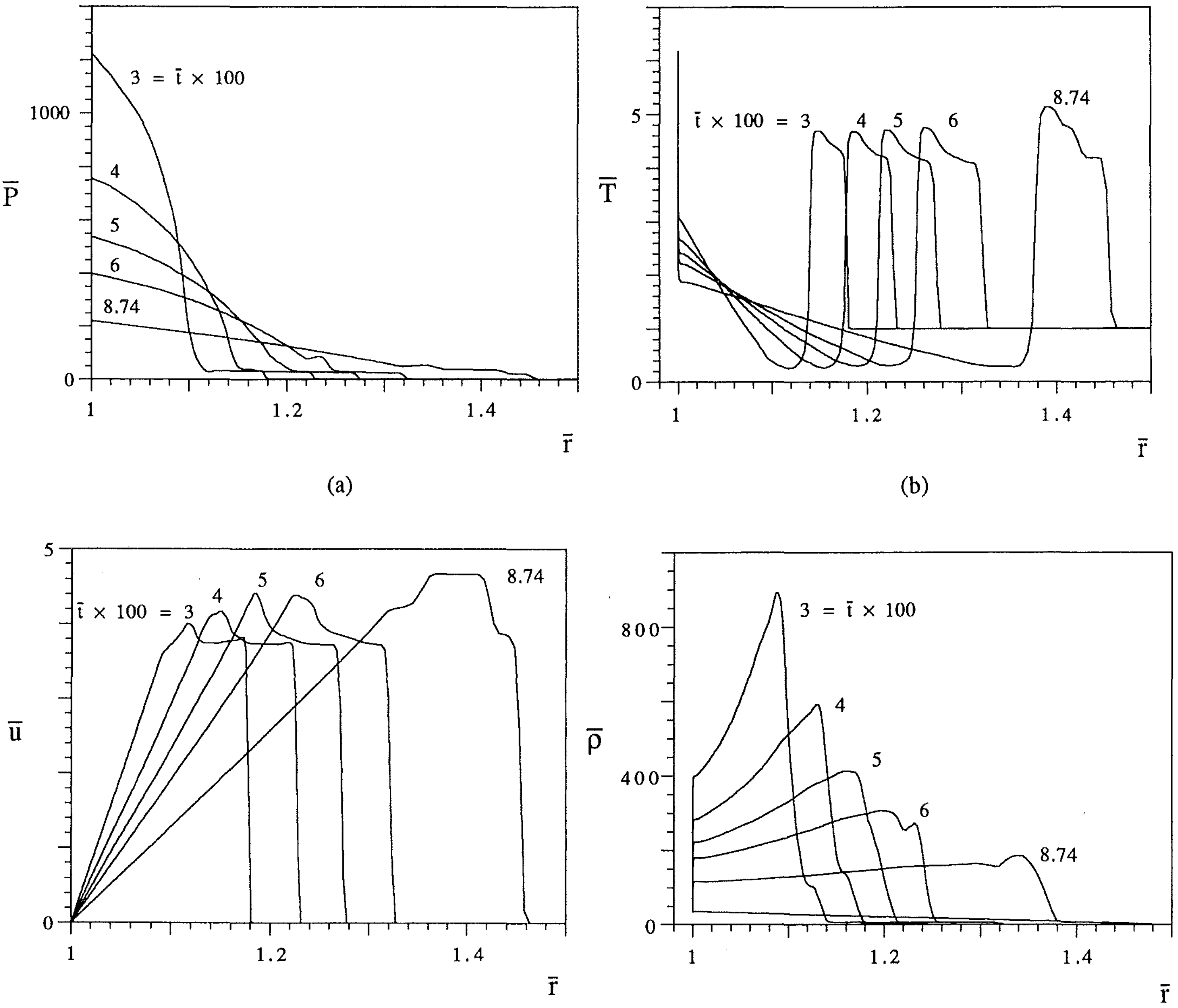

(a)

(b)

(c)

(d)

Figure 4. The water pressure (a), temperature (b), radial velocity (c) and density (d) distributions in the vicinity of the hot surface (R_S = 10 mm, ideal gas, spherical coordinates).

pressure. The two curves in Figure 5 also show the effects of changing the value of the initial pressure at the interface. The final time $\bar{t}$ (when $\bar{P}$ is equal to the critical pressure) increases slightly (from 0.0874 to 0.1) as the initial pressure $\bar{P}_i$ changes from 1.28×10^4 to 1.6×10^4.

The effect of changing the hot surface radius R_s and the system of coordinates (i.e., spherical vs. cartesian) is illustrated in Fig. 6. Spherical coordinates were used for $R_s = 1$, 5 and 10 mm, and cartesian coordinates for $R_s = 10$ mm. We found that there is practically no difference between the results for $R_s = 10$ mm in spherical and cartesian coordinates. The four frames of Fig. 6 show that the waves have larger amplitudes when the sphere radius is small ($R_s = 1$ mm). The choice between spherical and cartesian coordinates matters when the dimension of the solidifying material is small. The corresponding pressure history at the surface is shown in Fig. 7: again, the behavior at small R_s in spherical coordinates is different, as the pressure starts to decay earlier.

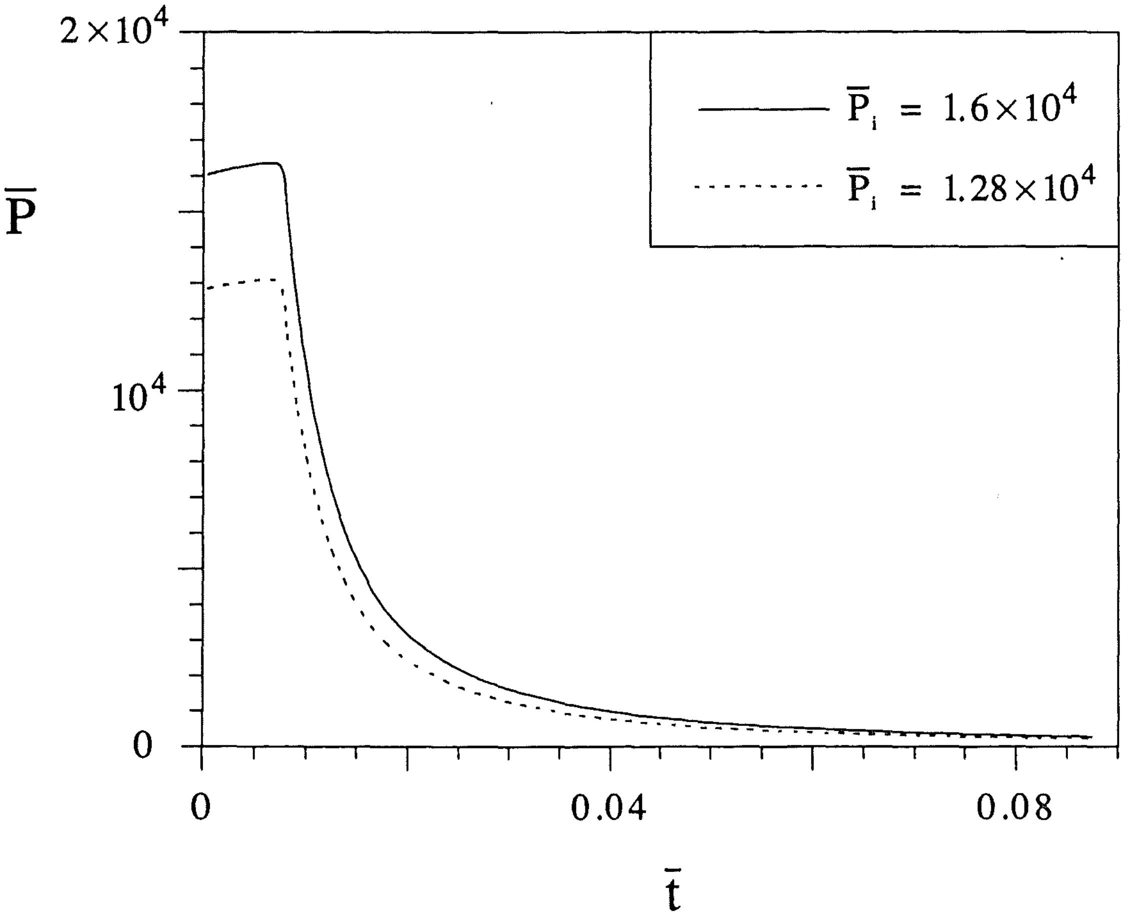

Figure 5. The pressure history at the surface (R_s = 10 mm, ideal gas, spherical coordinates), and the effect of the initial interface pressure.

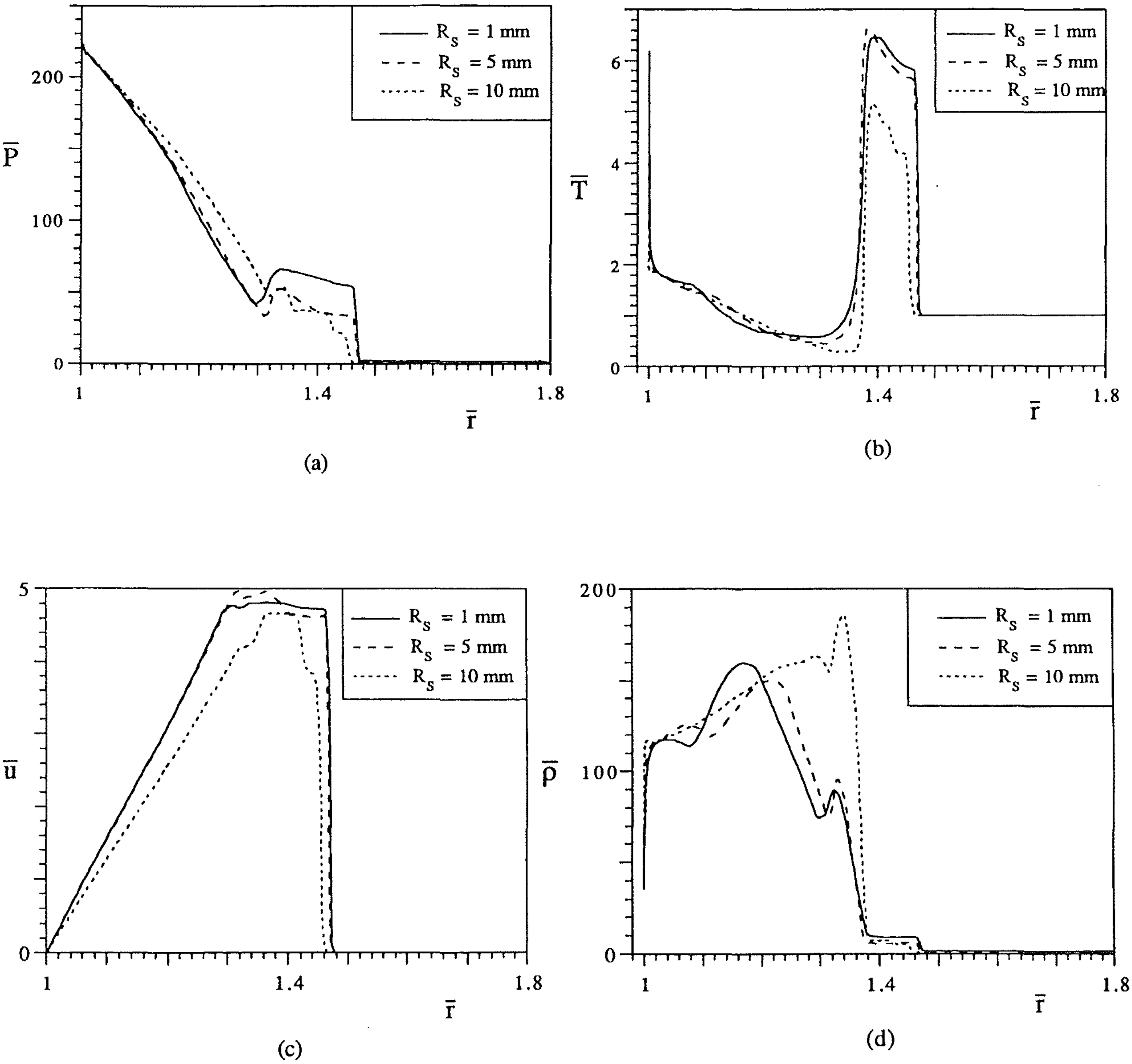

(a) (b)

(c) (d)

Figure 6. The effect of the system size (R_S) on the water pressure, temperature, velocity and density distributions (ideal gas, $\bar{t}$ = 0.0874).

Real gas model. We also performed numerical simulations using the real gas model for water, i.e. the actual properties of water at high temperatures and high pressures. Figures 8a through 8d show the evolution of pressure, temperature, velocity and density for a simulation with R_S = 10 mm, in cartesian coordinates. The features of the respective waves are similar to those shown in Figures 4a through 4d regarding both the trends and the respective orders of magnitude.

A quantitative comparison between the real-gas and ideal-gas simulations is presented in Figures 9a through 9d, where all the curves correspond to the time $\bar{t}$ = 0.0138 in simulations with R_S = 10 mm in cartesian coordinates. These figures show that the ideal-gas results anticipate within a factor of order 1 the results based on the more exact (and more expensive) real-gas modeling. Nevertheless, differences between the two sets can result. For example, in Fig. 9b the temperature behind the thermal wave is higher in the real

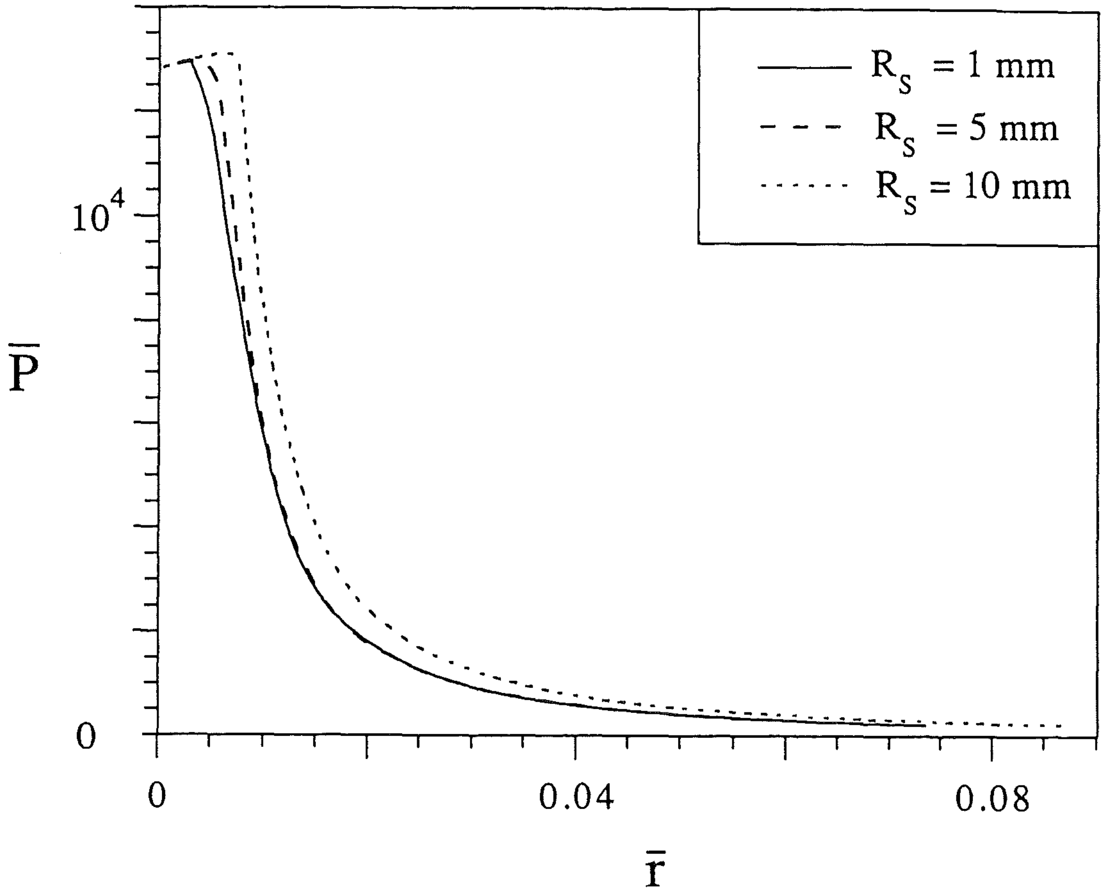

Figure 7. The effect of the system size on the pressure history at the surface (ideal gas).

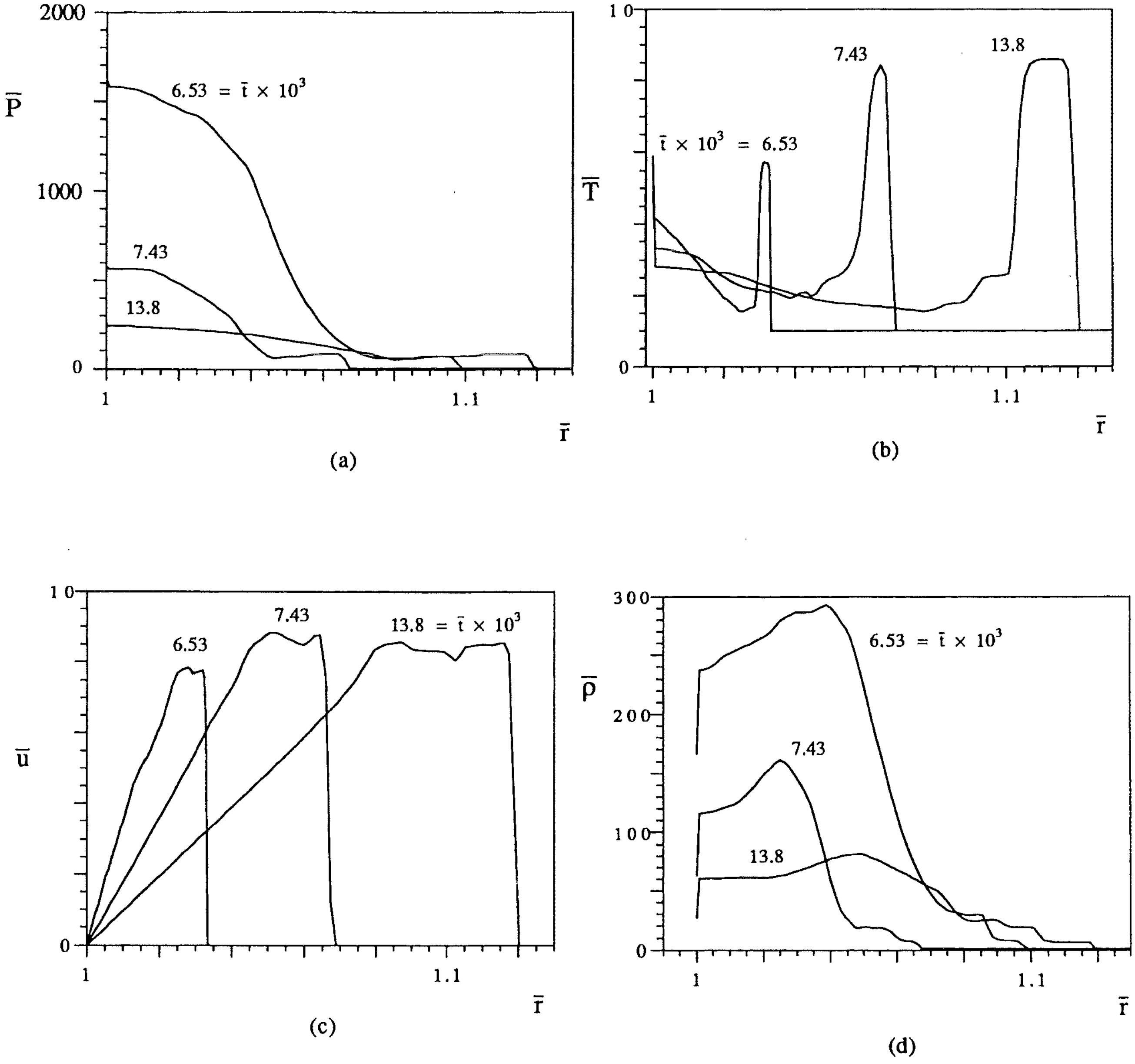

(a)

(b)

(c)

(d)

Figure 8. The water pressure (a), temperature (b), radial velocity (c) and density (d) distributions in the vicinity of the hot surface (R_S = 10 mm, real gas, cartesian coordinates).

gas case. This effect is expected since, although the wall heat flux is the same in both cases, the real-gas entropy is smaller because in a real gas there exists a pseudo-grid (grid determined by the interaction forces) between molecules. In the space occupied by the wave the ideal-gas temperature is higher because the kinetic energy of the molecules is not dissipated through intramolecular interactions.

Finally, Fig. 10 presents a comparison between the surface pressure histories produced by the real-gas and ideal-gas simulations. The ideal-gas model overestimates the time of approach to critical pressure. The ideal-gas pressure is higher (see also Fig. 9a) because at the molecular level the pressure is proportional to the number of collisions between molecules. That number is higher when attraction and repulsion forces are absent, as in an ideal gas. Furthermore, the speed of propagation of the pressure wave is higher in an ideal gas since the interaction forces in a real gas amount to a resistance that must be overcome. This is consistent with Fig. 10, which shows that the time required for the interfacial pressure to become critical is longer in the real gas case ($\overline{t} = 0.16$) as compared to the ideal gas case ($\overline{t} = 0.0874$).

The correct order-of-magnitude predictions obtained using the ideal gas model are important because the implementation of the real gas model is difficult. For example, the interpolation of water properties (this section) or the use of a real-gas equation of state (as in Steiner and Gretler [9]) requires additional numerical procedures that increase the computational time and may cause convergence problems.

2.5 Closing Comments

This numerical study has presented the thermal and fluid flow interaction between water and a hot surface, when the initial interfacial pressure is supercritical. The sudden contact generates temperature, pressure and density waves that propagate away from the surface with the same speed, which is a resultant of the characteristic speeds. Only in the limiting case of small perturbations (linear model) do the waves propagate with the speed of sound. The interfacial pressure decays in time and drops below the critical pressure at a time of order $\bar{t} \sim 0.08$, which corresponds physically to 10^{-6} s. To continue the description of this phenomenon to longer times, the single-phase water model used in this paper must be replaced by a model with phase change (steam) in the vicinity of the hot surface.

We modeled the water as a single-phase inviscid fluid that behaves either as an ideal gas or as a real gas with properties taken from steam tables. We found that the numerical results based on the ideal-gas formulation are in good qualitative agreement with the results based on the real-gas formulation. The quantitative agreement between the respective results is within a factor of order 1. This agreement is relevant to future work on extending to longer times the study of the interaction between water and a hot surface, because the modeling of water at high T and P as an ideal gas is considerably more cost efficient. We

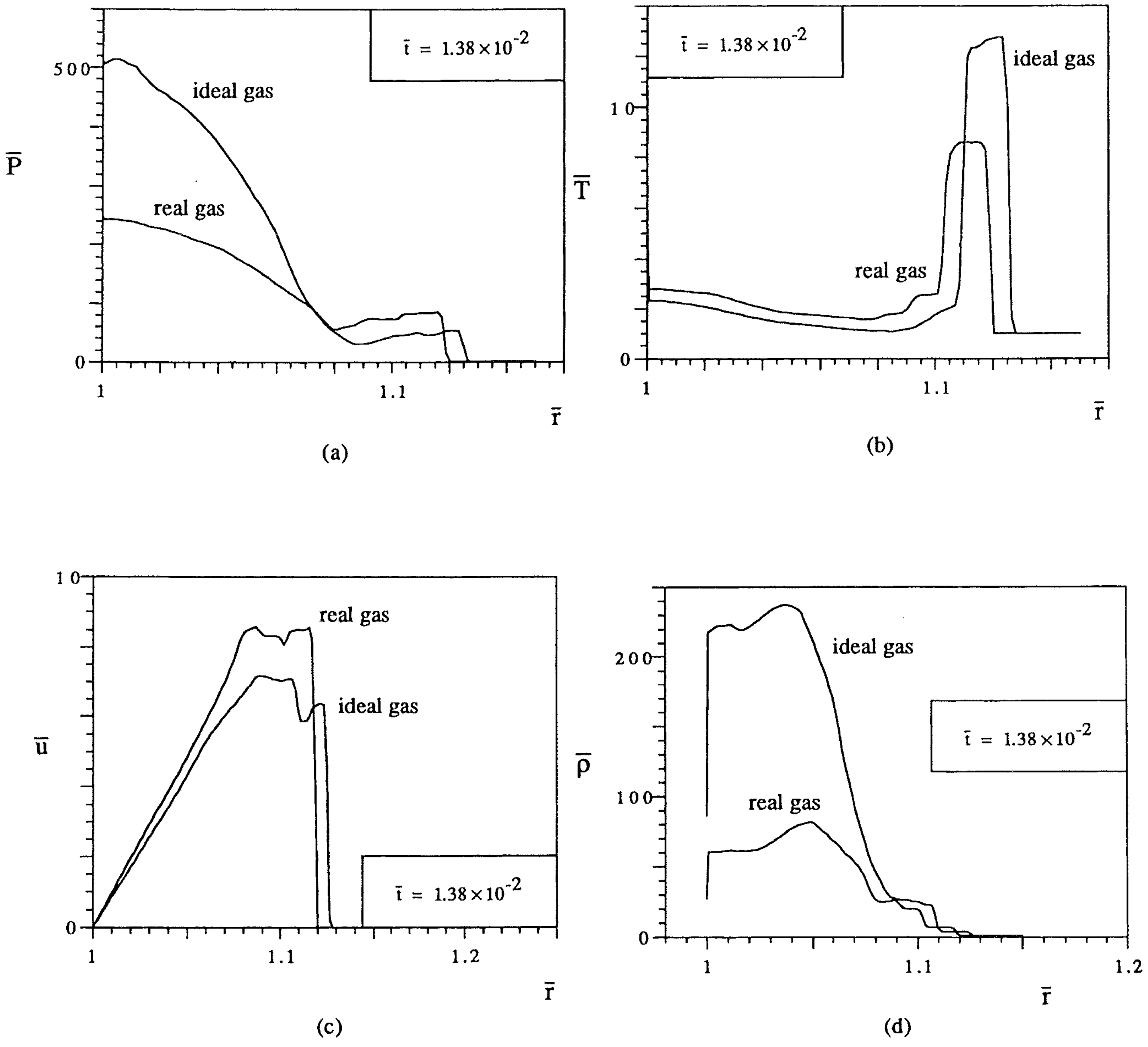

(a) (b) (c) (d)

Figure 9. Comparison between real-gas and ideal-gas simulations with R_S = 10 mm in cartesian coordinates.

also found that the choice between working in spherical coordinates and working in the simpler cartesian coordinates is important: when the size (R_S) of the hot object is small, accuracy demands the use of spherical coordinates.

3 EXPANSION OF A MIXTURE OF HOT PARTICLES, STEAM AND LIQUID WATER

In this section we examine the fundamental thermodynamic aspects of energy conversion during the expansion of a mixture containing saturated liquid water and droplets of high-temperature molten material. The mixture expands because of the volumetric generation of steam. At the same time, the heat released by the molten material is converted partially into mechanical energy. The objective is to show how the irreversibility due to intense heat transfer acts toward decreasing the energy conversion efficiency.

3.1 Mathematical Formulation

The expanding body of steam, water, and molten material is assumed to be mixed: the three-phase mixture is composed of a large number of spherical elemental systems of the

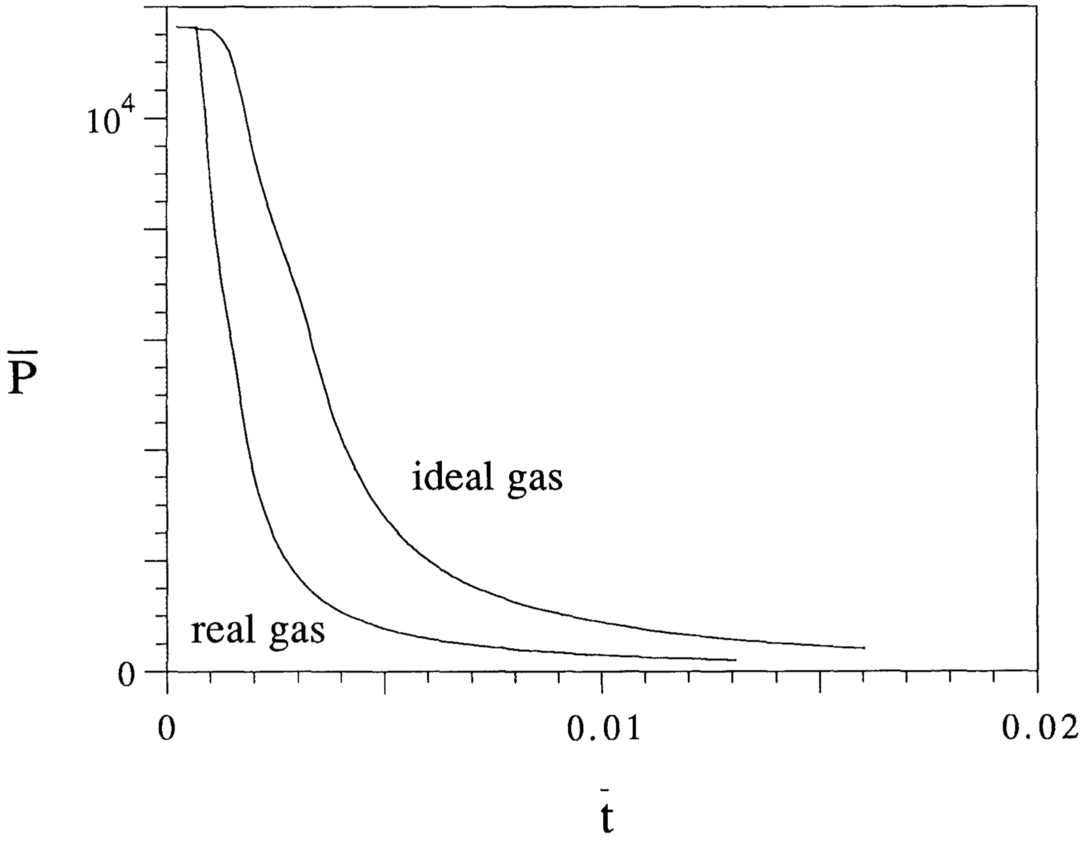

Figure 10. Comparison between the real-gas and ideal-gas simulations of the pressure history at the surface (R_S = 10 mm, cartesian coordinates).

type shown in Fig. 11a. Each elemental system consists of a spherical drop of molten material coated by a layer of steam and immersed in liquid water. At every point in time, the elemental systems are distributed uniformly throughout the mixture. The melt radius r_m is a specified parameter. The steam radius is time-dependent, $r_s(t)$. The spherical symmetry of each elemental system is preserved until adjacent steam layers touch, Fig. 11b.

The heat transfer from the molten material to the steam and the steam-water interface drives the evaporation process that, in an aggregate sense, is visualized by the expanding mixture. In the simplest application of the model, the mixture occupies a one-dimensional layer adjacent to a solid wall, Fig. 12, and is initially at rest. The mixture expands and is accelerated away from the wall. To model the behavior of the mixture, we consider a sample of mass

$$m = m_m + m_s + m_w, \tag{35}$$

and note that the amount of molten material (m_m) does not change during the expansion. In time, some of the liquid water inventory (m_w) changes into steam (m_s). In the beginning ($t = 0$), the amount of water (all in liquid form) is m_{w0} and this quantity does not change during the process so that

$$m_s + m_w = m_{w0} = \text{constant}. \tag{36}$$

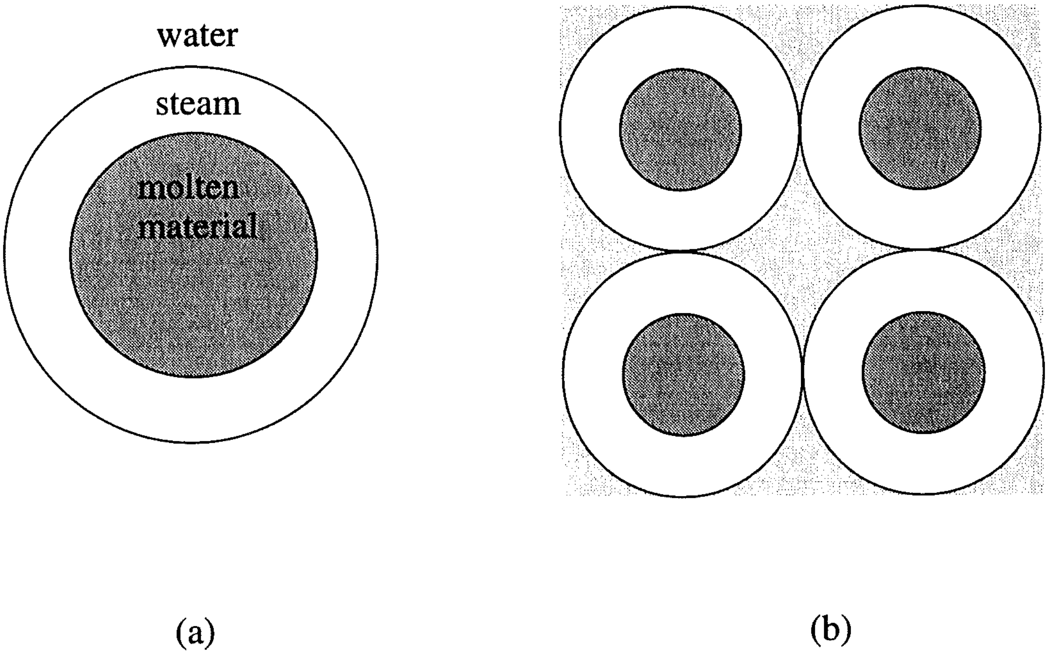

Figure 11. (a) Spherical elemental system and (b) time when adjacent steam layers touch.

We assume that there are N droplets of molten material distributed uniformly throughout m. The volumes occupied by the melt, steam and liquid water in the volume of the mixture sample m are, respectively

$$V_m = N\,4\pi\, r_m^3/\,3 \qquad\qquad V_s = N\,4\pi\left(r_s^3 - r_m^3\right)/\,3 \tag{37}$$

$$V_w = \left(m_{w0} - m_s\right)/\,\rho_w = m_{w0}/\,\rho_w - N\left(\bar{\rho}_s/\,\rho_w\right)\left(4\pi/3\right)\left(r_s^3 - r_m^3\right) \tag{38}$$

where ρ_w and $\bar{\rho}_s$ are the density of liquid water (constant), and the density of steam averaged over the steam volume V_s. The amount of molten material (density ρ_m) present in the sample is

$$m_m = N\rho_m\, 4\pi\, r_m^3/\,3 \tag{39}$$

To calculate the instantaneous density of the mixture we write $\rho = m\,/\,V$, where V is the volume of the sample, $V = V_m + V_s + V_w$. The result can be expressed as a specific volume

$$\rho^{-1} = \left(1 - \varepsilon\right)/\,\rho_w + \left(\varepsilon\,/\,\rho_m\right)\left[\bar{\rho}_s/\,\rho_w + \left(r_s/\,r_m\right)^3\left(1 - \bar{\rho}_s/\,\rho_w\right)\right], \tag{40}$$

where the melt mass fraction ε is a specified constant, $\varepsilon = m_m\,/\,m$, or $1 - \varepsilon = m_{w0}/m$. Because $\rho_s \ll \rho_w$, a simpler alternative to Eq. (40) is

$$\rho^{-1} \cong \left(1 - \varepsilon\right)\rho_w + \left(\varepsilon\,/\,\rho_m\right)\left(r_s/\,r_m\right)^3. \tag{41}$$

Equations (40,41) show that the specific volume ρ^{-1} increases with r_s, and, as the analysis will show, r_s increases with time. The order of magnitude of the time when the Fig. 11a scenario ends can be estimated with the cubic model of Fig. 11b, in which the steam layers just touch. It can be shown that the volume averaged mixture density at the moment depicted in Fig. 11b is

$$\rho = 0.476\,\rho_w + 0.524\,\rho_m\left[\left(r_m/\,r_s\right)^3\left(1 - \bar{\rho}_s/\,\rho_m\right) + \bar{\rho}_s/\,\rho_m\right]. \tag{42}$$

In other words, the validity of the model expires at the time t when $\rho(t)$ of Eq. (40) drops to the value given by Eq. (42). In the latter, the second term is smaller than the first, because $\bar{\rho}_s \ll \rho_m$ and $(r_m\,/\,r_s)^3 \ll 1$. Since the initial density of the mixture is comparable with ρ_w, we anticipate that the Fig. 11a scenario will end when ρ drops to about half of its original value. This is equivalent to saying that the scenario ends when the equivalent radius of the interstitial liquid water assigned to the elemental system becomes of the same order as the steam radius.

The equation for the conservation of mass in the volume averaged mixture is

$$\frac{\partial \rho}{\partial t} + \frac{\partial}{\partial y}(\rho v) = 0 , \tag{43}$$

where y points away from the solid wall, and v(y, t) is the volume averaged velocity in the y direction, Fig. 12. The mixture thickness L(t) increases in time. The mixture density is in general a function of both t and y. If viscous effects are assumed negligible, the momentum equation is

$$\rho\left(\frac{\partial v}{\partial t} + v\,\frac{\partial v}{\partial y}\right) = -\,\frac{\partial P}{\partial y} , \tag{44}$$

where $\rho(y, t)$ is furnished by Eq. (40). The conservation of the original mass inventory provides the constraint for calculating L(t):

$$\int_0^{L_0} \rho\,(y, 0)\,dy = \int_0^{L(t)} \rho\,(y, t)\,dy\ . \tag{45}$$

The problem formulated so far consists of four equations [Eqs. (40), and (43) - (45)] for five unknown functions (ρ, v, P, L, r_s). We close the problem by accounting for energy conservation during the steam generation process in the element of Fig. 11. That element is actually more complicated, as shown in Fig. 13, because, in time, the molten material develops a solid crust. The question is whether all the complications of this configuration are important in predicting the variation of $r_s(t)$. Order of magnitude calculations based on the dimensions listed in Table 1 show that: (i) The effect of thermal radiation from T_m to T_s is greater than the effect of direct conduction through the steam when r_m exceeds the order 0.1 mm. (ii) The solid-crust outer temperature T_m is nearly constant (time-

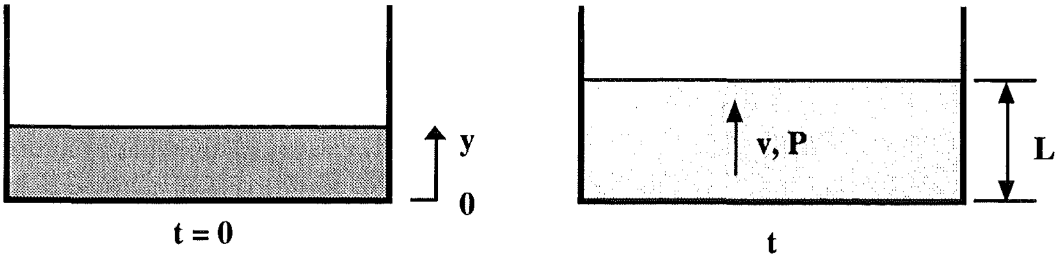

Figure 12. One-dimensional layer occupied by the expanding mixture.

independent) and almost equal to the original (solidification) temperature of the molten material. (iii) The thermal inertia of the solid crust is negligible because its Stefan number is approximately 0.03. (iv) The thermal inertia of the steam is not negligible because the steam Jakob number $c_p (T_m - T_s) / h_{fg}$ is approximately equal to 2. (v) The time-dependent conduction into the liquid water is negligible because the pressure changes are such that the changes in the interface (saturation) temperature T_s are small.

These characteristics, justify the following model for the steam generation process (cf. Fig. 13): (a) Time-independent surface temperature (T_m) at $r = r_m$. (b) Steam layer with thermal inertia and temperature T(r, t). (c) Steam-water interface with time-independent temperature (T_s) at $r = r_s$. (d) The steam behaves as an ideal gas with known constants (c_p, R), and spatially uniform pressure P(t). According to this model, the radial heat transfer and steam motion at a radius r inside the steam annulus are governed by

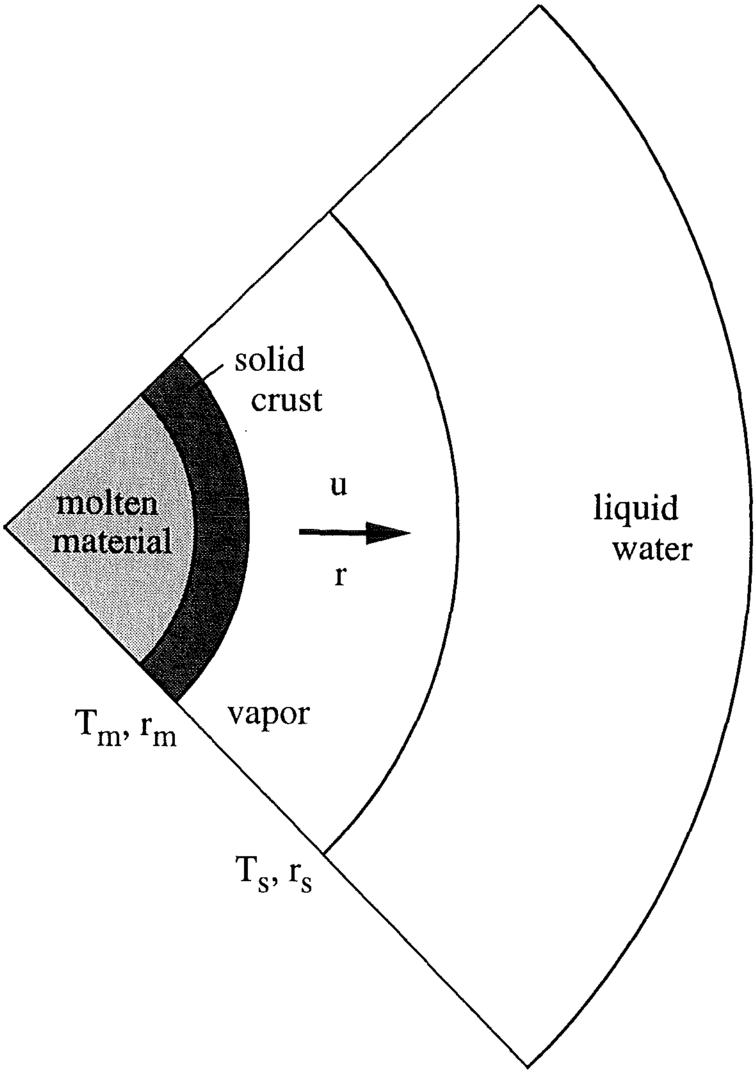

Figure 13. The four-layer structure of the elemental system of Fig. 11a.

$$\frac{1}{r^2}\frac{\partial}{\partial r}\left(r^2 u\right) = \frac{1}{T}\left(\frac{\partial T}{\partial t} + u\,\frac{\partial T}{\partial r}\right), \tag{46}$$

$$\frac{c_p P}{RT}\left(\frac{\partial T}{\partial t} + u\,\frac{\partial T}{\partial r}\right) = \frac{1}{r^2}\frac{\partial}{\partial r}\left(k\,r^2\,\frac{\partial T}{\partial r}\right). \tag{47}$$

In Eq. (47) the steam thermal conductivity is a strong function of temperature, k(T). By eliminating the rhs of Eq. (46) between Eqs. (46) and (47), and integrating away from $r = r_m$ where the radial steam velocity u is zero, we obtain

$$\left(c_p / R\right) P\, r^2 u = k\, r^2 \left(\partial T / \partial t\right) - k_m\, r_m^2 \left(\partial T / \partial r\right)_{r_m}, \tag{48}$$

where $k_m = k\,(T_m)$. Equation (48) delivers the velocity distribution u(r, t) when the steam temperature distribution T(r, t) is known.

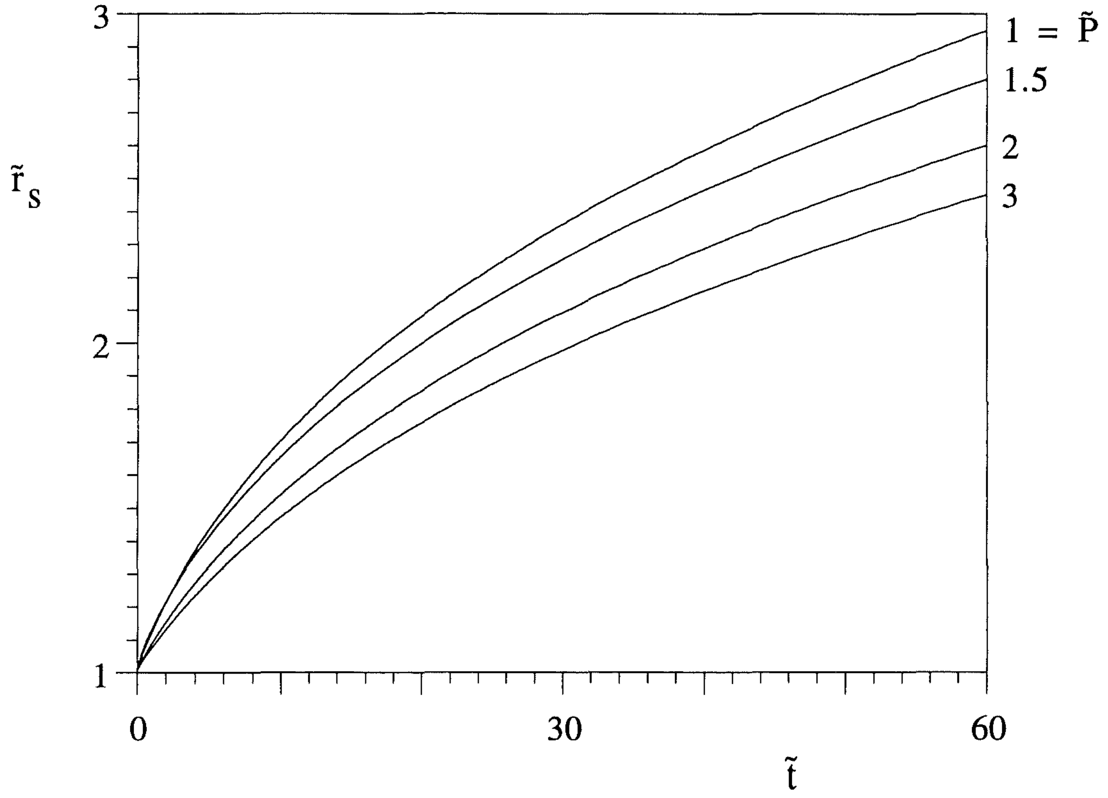

Figure 14. The effect of the assumed constant pressure $\tilde{P}$ on the history of the outer steam radius, for the dimensions listed in Table 1.

The thermal boundary condition at the inner interface is $T(r_m, t) = T_m$. At the liquid water interface we have a balance between the heat transfer (radiation and conduction) from the steam side and the latent heat of the vaporized liquid,

$$q_{rad} + 4\pi r_s^2 k_s \left(-\partial T / \partial r\right)_{r_s} = 4\pi r_s^2 \rho_s h_{fg} \left(dr_s / dt\right), \tag{49}$$

where ρ_s is the steam density at saturation (T_s), and

$$q_{rad} = 4\pi r_m^2 \sigma \varepsilon_m \left(T_m^4 - T_s^4\right) / \left[1 + \left(r_m / r_s\right)^2 \varepsilon_m \left(\varepsilon_s^{-1} - 1\right)\right]. \tag{50}$$

Equation (50) is based on the enclosure model with two gray surfaces of emissivities ε_m and ε_s. The initial condition is $r_s(0) = r_m$.

3.2 Numerical Method

The numerical solution to the $r_s(t)$ problem represented by Eqs. (47)-(49), and the compact presentation of this solution are aided by the use of the dimensionless variables

$$\tilde{r} = r / r_m, \quad \tilde{T} = T / T_m, \quad \tilde{P} = P / P_0, \quad \tilde{k} = k / k_m, \tag{51}$$

$$\tilde{u} = u\, c_p P_0 r_m / \left(R k_m T_m\right), \qquad \tilde{t} = t R k_m T_m / \left(c_p P_0 r_m^2\right) \tag{52}$$

where P_0 is the reference (atmospheric) pressure. Equations (47) - (49) become

$$\tilde{P} \int_1^{\tilde{r}_s} \left(\frac{\partial \tilde{T}}{\partial \tilde{t}} + \tilde{u} \frac{\partial \tilde{T}}{\partial \tilde{r}}\right) \frac{\tilde{r}^2}{\tilde{T}}\, d\tilde{r} = \tilde{k}_s \tilde{r}_s^2 \left(\frac{\partial \tilde{T}}{\partial \tilde{r}}\right)_{\tilde{r}_s} - \left(\frac{\partial \tilde{T}}{\partial \tilde{r}}\right)_1 \tag{53}$$

$$\tilde{P} \tilde{u} = \tilde{k} \frac{\partial \tilde{T}}{\partial \tilde{r}} - \frac{1}{\tilde{r}^2} \left(\frac{\partial \tilde{T}}{\partial \tilde{r}}\right)_1, \tag{54}$$

$$\frac{B}{1 + C \tilde{r}_s^{-2}} - A \tilde{k}_s \tilde{r}_s^2 \left(\frac{\partial \tilde{T}}{\partial \tilde{r}}\right)_{\tilde{r}_s} = \tilde{r}_s^2 \frac{d \tilde{r}_s}{d \tilde{t}}, \tag{55}$$

where A, B, C and $\tilde{k}_s$ are the constant dimensionless groups

$$A = \frac{c_p P_0}{R \rho_s h_{fg}}, \quad B = \frac{\sigma \varepsilon_m T_m^3 r_m c_p P_0}{R k_m \rho_s h_{fg}}, \quad C = \varepsilon_m \left(\varepsilon_s^{-1} - 1\right), \quad \tilde{k}_s = \frac{k_s}{k_m}. \tag{56}$$

Equation (53) was obtained by integrating Eq. (47) from the inner surface $(\tilde{r} = 1)$ to the outer surface $(\tilde{r} = \tilde{r}_s)$. The initial and boundary conditions are $\tilde{r}_s = 1$ at $\tilde{t} = 0$, $\tilde{T} = 1$ at $\tilde{r} = 1$, and $\tilde{T} = \tilde{T}_s$ $(<<1)$ at $\tilde{r} = \tilde{r}_s$.

The numerical method consisted of approximating the mass and momentum Eqs. (9, 10) by finite differences [33], in combination with numerical integral solutions for $\tilde{r}_s(\tilde{t})$, $\tilde{u}(\tilde{r}, \tilde{t})$ and $\tilde{T}(\tilde{r}, \tilde{t})$ inside the steam annulus. We assumed that the steam temperature distribution behaves as

$$\tilde{T} = \frac{a_1(\tilde{t})}{\tilde{r}} + \frac{a_2(\tilde{t})}{\tilde{r}^2} + \frac{a_3(\tilde{t})}{\tilde{r}^3}, \tag{57}$$

where the first term on the right side corresponds to the known (exact) shape of the $\tilde{T}$ solution in a spherical annulus with uniform density and negligible thermal inertia (e.g. Ref. 34, p. 35). The second and third terms account for the effect of steam thermal inertia. The time-dependent coefficients (a_1, a_2, a_3) are determined by fitting Eq. (57) to the boundary conditions (55), $\tilde{r}_s(0) = 1 + \varepsilon$, and $\tilde{T}(1,\tilde{t}) = 1$. The local $\tilde{T}$ value furnished by Eq. (57) is substituted into Eq. (54) to determine the local radial velocity $\tilde{u}(\tilde{r}, \tilde{t})$. Finally, the $\tilde{T}$ and $\tilde{u}$ values are substituted into Eq. (53) to obtain $\tilde{r}_s(\tilde{t})$. The analytical details of this algorithm are omitted for brevity. The integration across the steam thickness is based on the trapezoidal rule with specified accuracy (relative error less than 10^{-4}). The $\tilde{r}_s$ value at the next time step is obtained by using forward Euler time discretization. The moving line $\tilde{r} = \tilde{r}_s$ is always on the grid: this feature is preserved by using a front-tracking procedure and a time dependent grid spacing.

The numerical procedure is completed with the adoption of a correlation for the thermal conductivity of steam, $\tilde{k} = k / k_m$, where k_m and T_m are listed in Table 1. The following curvefit of the steam k data is particularly accurate in the range 1500-2300 K (cf. Ref. 35, p. 649)

$$\tilde{k}(\tilde{T}) = 0.002 \times \exp(6.2\,\tilde{T}). \tag{58}$$

We account for the thermal conductivity at lower temperatures (near the steam-water interface) by using instead of Eq. (58) the correct value $k_s \cong 0.025$ W/m K at $T_s = 373$ K, which is the same as writing that $\tilde{k}_s = 0.0195$.

The specified algorithm is sufficient for determining $\tilde{T}$, $\tilde{u}$, and finally $\tilde{r}_s$ for each elemental system, provided the steam pressure $\tilde{P}$ is specified. Indeed, the pressure $\tilde{P}$ effects the coupling between the evolution of the elemental system and the flow of the mixture. In general, in the geometry of Fig. 12 the mixture pressure is a function of both y and t. For a given P(y, t) value, the elemental algorithm would deliver the next value of r_s and, via Eq.

(40), the local mixture density to be substituted back into the mixture flow Eqs. (43, 44). This coupling is greatly simplified when the mixture pressure variation across the layer thickness L is negligible relative to P_0 such that the function P(y, t) may be approximated by the constant P_0 in the elemental system algorithm. In such a case the elemental algorithm has to be solved only once for each time step, and the histories $r_s(t)$ and $\rho(t)$ hold at every level y in the expanding mixture.

This simplification opportunity makes it necessary that we study the effect of the assumed time-independent pressure on the results generated by the elemental algorithm. The pressure effect is felt through ρ_s, c_p, h_{fg} and T_s, however, the most strongly affected are ρ_s and c_p. It can be shown that, in dimensionless form, this effect is condensed in the way in which A and B vary with the assumed $\tilde{P}$ constant. Figure 14 shows that although the steam radius is smaller when $\tilde{P}$ is larger, the $\tilde{P}$ effect is negligible when the $\tilde{P}$ values are restricted to the range $1 < \tilde{P} \lesssim 1.5$. We shall see that the pressure variation across the mixture layer is even less pronounced, such that the use of the constant $\tilde{P} = 1$ is justified in all the elemental system results exhibited in this paper.

Table 1. Sample of physical dimensions and calculated dimensionless parameters.

k_m =	1.28 W/m K	ρ_m =	3600 kg / m^3
k_s =	0.025 W / m K	ρ_w =	1000 kg / m^3
P_0 =	1.013 bar	σ =	5.67×10^{-8} W / m^{2}K^4
r_m =	1 mm		
R =	0.462 kJ / kg K	A =	0.61
T_m =	2295 K	A_1 =	5.38
T_s =	373 K	B =	0.262
ε =	0.15	C =	0.2
ε_m =	0.8	D =	0.017
ε_s =	0.8	$\tilde{k}_s$ =	0.0195

The time derivative of the $\tilde{r}_s$ history of Fig. 14 is the water interface velocity illustrated for $\tilde{P} = 1$ in Fig. 15. In this case the history is tracked until $\tilde{t} \sim 60$ when adjacent steam annuli touch (Fig. 11b). At that time the water velocity is 0.12 m/s. Relevant to this calculation is the question of whether the water kinetic energy should have been included in Eq. (55). The complete form of this equation is

$$\frac{B}{1 + C\tilde{r}_s^{-2}} - A\,\tilde{r}_s^2 \tilde{k}_s \left(\frac{\partial \tilde{T}}{\partial \tilde{r}}\right)_{\tilde{r}_s} = \tilde{r}_s^2 \frac{d\tilde{r}_s}{d\tilde{t}} \left[1 + D\left(\frac{d\tilde{r}_s}{d\tilde{t}}\right)^2\right] \qquad (59)$$

where the term containing D represents the water kinetic energy effect, where $D = \rho_w (R\, k_m T_m)^2 / 2\rho_s\, h_{fg}\, (c_p P_0 r_m)^2$. For the physical dimensions used in Table 1 the D value is 0.017. We performed the $\tilde{r}_s(\tilde{t})$ calculations of Fig. 14 using both Eqs. (55) and (59), and found no discernible difference between the two sets of results. In the case when the D effect was included, the numerical method led to a third order equation for $d\tilde{r}_s / d\tilde{t}$, which was solved at each time step based on the bisection method with 10^{-6} accuracy (Ref. 36, p. 353).

We also found that the $\tilde{r}_s(\tilde{t})$ solution does not change when in the assumed steam temperature function (57) the third denominator $(\tilde{r}^3)$ is replaced with $\tilde{r}^{0.5}$. This finding shows that the integral method of treating the space $1 < \tilde{r} < \tilde{r}_s$ is robust, and that the behavior of the $\tilde{T}$ profile (57) is captured by the known limiting solution (the $a_1/\tilde{r}$ term).

Continuing the description of the quantities that can be calculated at the elemental level, we see in Fig. 16 the history of the heat release from the sphere of molten material. The instantaneous heat transfer rate $\tilde{q}$ is due to two contributions, conduction from the melt to the adjacent steam layer, and radiation from the melt to the water front,

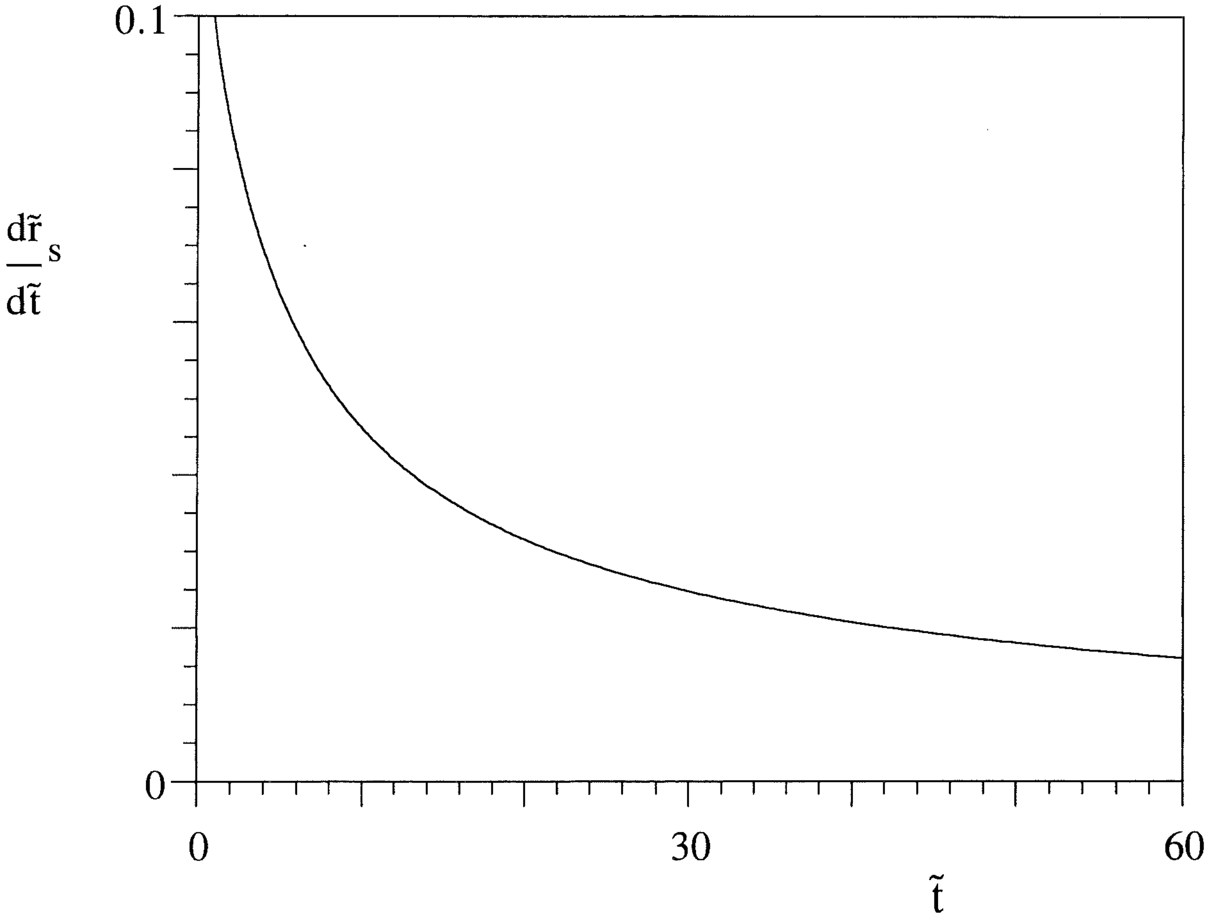

Figure 15. The steam-water interface velocity in the elemental system of Fig. 14.

$$\tilde{q} = \tilde{q}_{\text{cond}} + \tilde{q}_{\text{rad}} = 4\,\pi\,\tilde{k}_s\,\tilde{r}_s^2\left(-\partial\tilde{T}/\partial\tilde{r}\right)_{\tilde{r}_s} + A_1\left(1-\tilde{T}_s^4\right)/\left(1+C\,\tilde{r}_s^{-2}\right). \tag{60}$$

where

$$\tilde{q} = q/\left(k_m r_m T_m\right), \qquad A_1 = 4\pi\sigma\,\varepsilon_m\,r_m T_m^3/k_m\,. \tag{61}$$

The total heat transfer rate drops rapidly to an early minimum, and then becomes practically constant. The radiation contribution increases and reaches a plateau, while the conduction contribution $(\tilde{q} - \tilde{q}_{\text{rad}})$ drops to a negligible level.

3.3 Energy Conversion

The elemental algorithm developed in the preceding section can be combined with the volume averaged mixture model in any flow geometry. The link is provided by the density history $\rho/\rho_w = \tilde{\rho}\,(\tilde{t})$, which is obtained by substituting the calculated function $\tilde{r}_s(\tilde{t})$ into Eq. (40). One example is shown in Fig. 17, which shows that the calculations end at the time $\tilde{t} = 51$ when the density $\tilde{\rho}$ drops to approximately half of its original value (Fig. 11b).

The density history $\tilde{\rho}\,(\tilde{t})$ is combined with Eqs. (43, 44), which acquire the dimensionless form

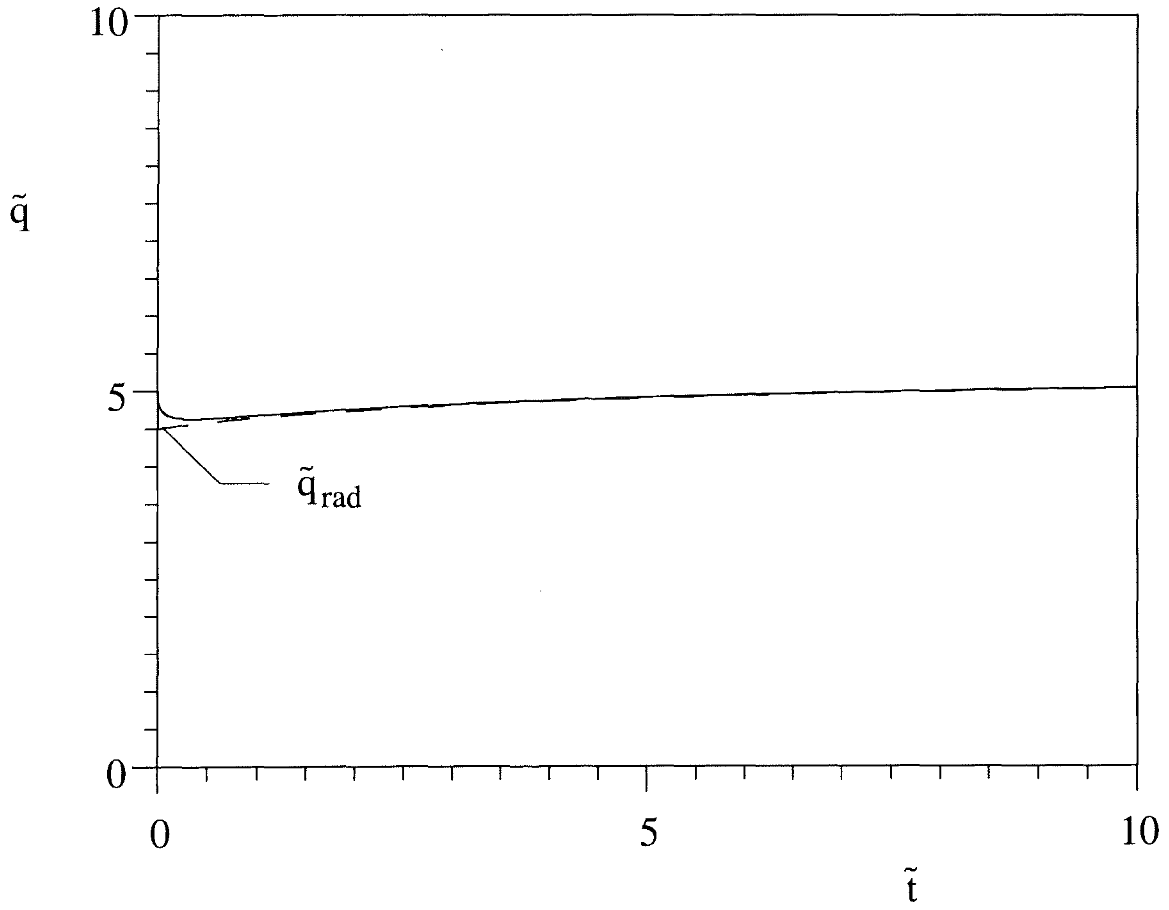

Figure 16. The heat released by the molten material in the elemental system of Fig. 14.

$$\frac{\partial \tilde{\rho}}{\partial \tilde{t}} + \tilde{\rho} \frac{\partial \tilde{v}}{\partial \tilde{y}} = 0, \qquad (62)$$

$$\tilde{\rho} \left(\frac{\partial \tilde{v}}{\partial \tilde{t}} + \tilde{v} \frac{\partial \tilde{v}}{\partial \tilde{y}} \right) = \frac{1}{E} \frac{\partial \tilde{P}}{\partial \tilde{y}}, \qquad (63)$$

where

$$\tilde{y} = y / r_m, \quad \tilde{v} = v c_p P_0 r_m / \left(R k_m T_m \right), \quad E = \rho_w R^2 k_m^2 T_m^2 / \left(c_p^2 P_0^3 r_m^2 \right). \qquad (64)$$

and $\tilde{y}$ is measured away from the wall (Fig. 12) to the free surface $\tilde{y} = \tilde{L}(\tilde{t})$, where $\tilde{L} = L_0 / r_m$. Equations (62) and (63) were solved for $\tilde{v}(\tilde{y}, \tilde{t})$ and $\tilde{P}(\tilde{y}, \tilde{t})$ using a second-order accurate discretization scheme. The dependent variables $\tilde{P}$ and $\tilde{v}$ were evaluated at different grid points: specifically, $\tilde{P}$ was evaluated at the half distance between two adjacent points were the $\tilde{v}$ values were defined. This method leads to an increase in accuracy without requiring grid refinement [33].

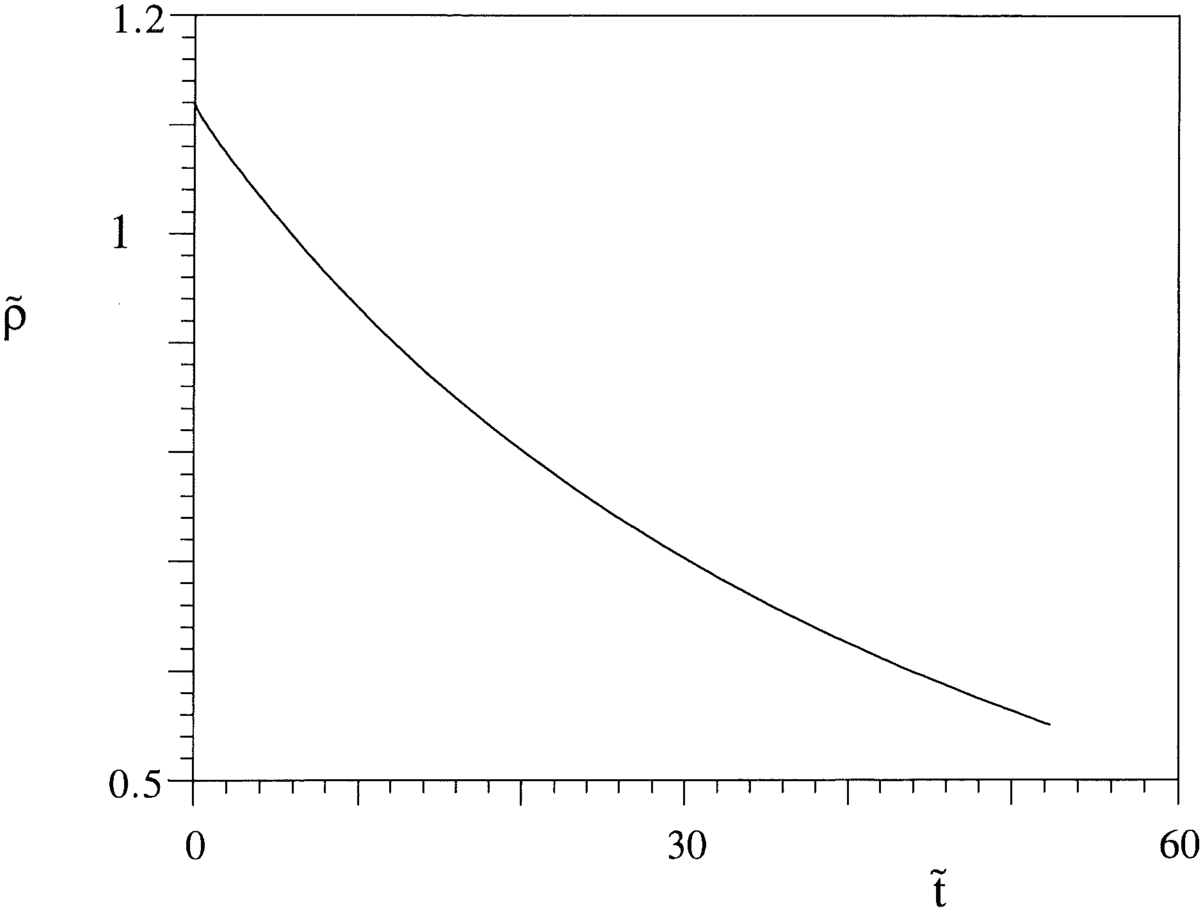

Figure 17. The mixture density history corresponding to the elemental system (Fig. 14).

The $\tilde{\rho}$ and $\tilde{v}$ fields were used to calculate the kinetic energy inventory of the mixture,

$$KE = \rho_w V_{scale}^2 V(t) \left(\int_0^{\tilde{L}(\tilde{t})} \frac{1}{2} \tilde{\rho} \tilde{v}^2 \, d\tilde{y} \right) / \tilde{L}(\tilde{t}) \tag{65}$$

where V(t) is the mixture volume, and the velocity scale is given in Eq. (64), $V_{scale} = R k_m T_m / (c_p P_0 r_m)$. We then compared KE(t) with the heat transferred out of the molten spheres during the same time interval t,

$$Q = \tilde{Q}(\tilde{t}) r_m^3 P_0 N c_p / R, \tag{66}$$

where N is the number of spheres of molten material present in the initial mixture volume sample, $V_0 = L_0^3$. Note that the volume sample is a layer of thickness L_0 covering a wall unit area L_0^2. The number N is proportional to ε, and follows from the ε definition shown under Eq. (40),

$$N = 3\varepsilon V_0 \rho_w / \left(4\pi r_m^3 \rho_m\right). \tag{67}$$

In Eq. (66), the heat release history is provided by Eq. (60) via

$$Q / \left(c_p / R\right) P_0 r_m^3 N = \tilde{Q}(\tilde{t}) = \int_0^{\tilde{t}} \tilde{q} \, d\tilde{t}, \tag{68}$$

and Q[J] is the corresponding dimensional value. Finally, the energy conversion efficiency is calculated as

$$\eta = KE / Q . \tag{69}$$

We expect small η values because most of the exergy released by the molten droplets is destroyed by heat transfer in the very small temperature gaps (or very steep temperature gradients) between molten material (T_t) and liquid water (T_s). The time-dependent energy conversion process is monitored numerically until the steam annuli of adjacent molten droplets touch, which corresponds to the time when L(t) grows to approximately twice the initial thickness L_0, or when the mixture density decreases to about half of its original value, Fig. 11b.

3.4 Discussion

In this section we present the results in dimensional (physical) terms, while indicating in the insets the dimensions that were assumed given at the start of the calculations. As noted earlier, the pressure in the steam annuli was assumed uniform at P_0 in order to decouple the $r_s(t)$ calculation from the pressure field of the mixture. Figure 18 shows that the local velocity increases almost linearly away from the solid wall (y = 0), and the free surface velocity [v at y = L(t)] is nearly constant during the time interval 0.18 ms < t < 7.6 ms. This feature is also evident in Fig. 19, which shows the evolution of the layer thickness, L(t). Figure 19 also shows that the mixture expansion becomes faster as the molten mass fraction ε increases.

The effect of varying the mass fraction of molten material while holding the other parameters fixed is illustrated further in Figs. 20 and 21. The ε values 0.15, 0.225 and 0.3 correspond to N = 10, 15 and 30, respectively. The kinetic energy acquired by the mixture (Fig. 20) increases considerably as ε increases: this effect is felt especially at long times. The energy conversion efficiency (Fig. 21) is less sensitive to changes in ε; in fact, the sensitivity decreases as ε increases to values of order 0.3.

Figure 22 documents the effect of increasing the size of the system (L_0) when the molten droplet size (r_m) and mass fraction (ε) are fixed. The L_0 values (10, 15 and 20 mm) correspond, in order, to N = 10, 22 and 40. The efficiency increases by one order of magnitude as the mixture thickness increases by a factor of 2. This is a very important conclusion, which says that large (thicker) mixture systems are more efficient as converters of heating into mechanical energy.

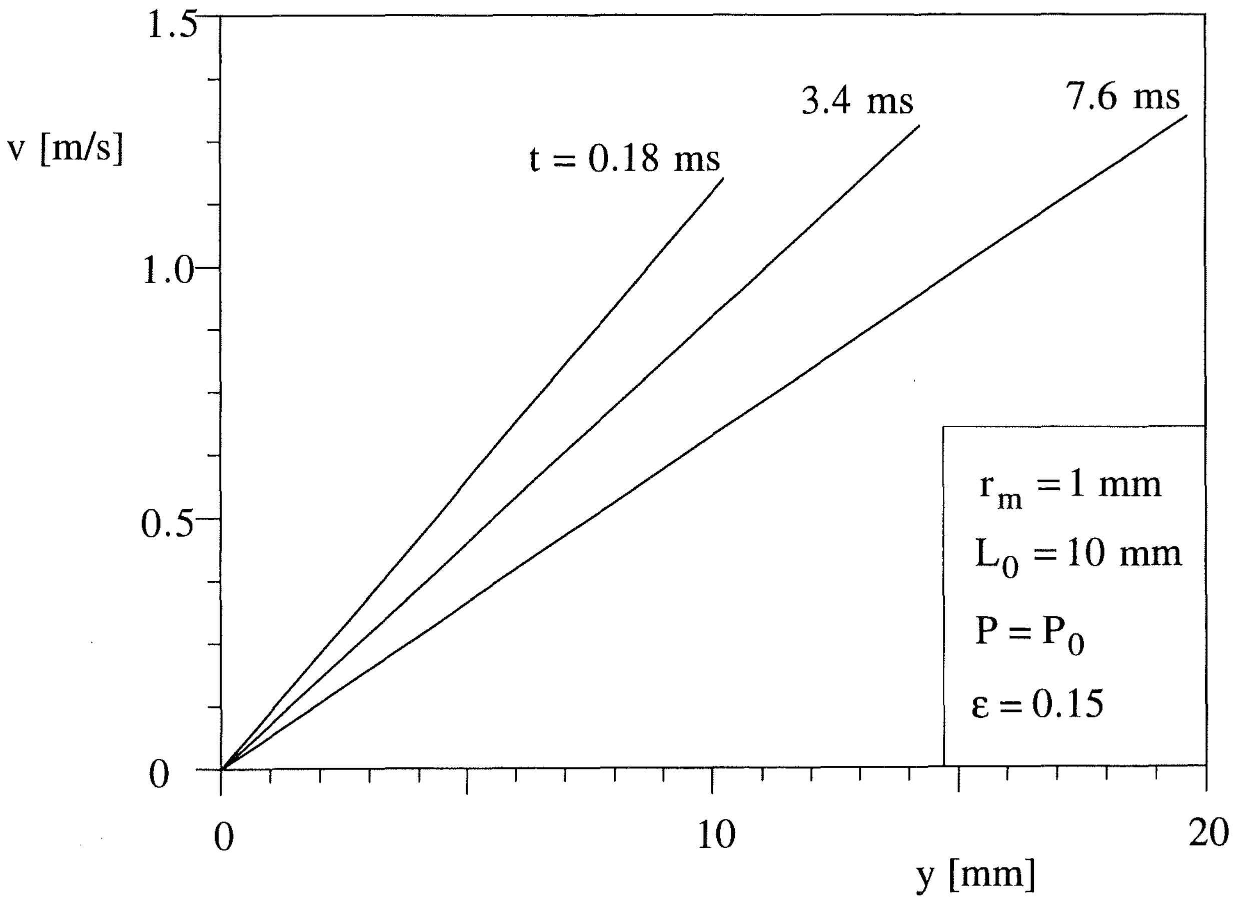

Figure 18. The evolution of the local mixture velocity.

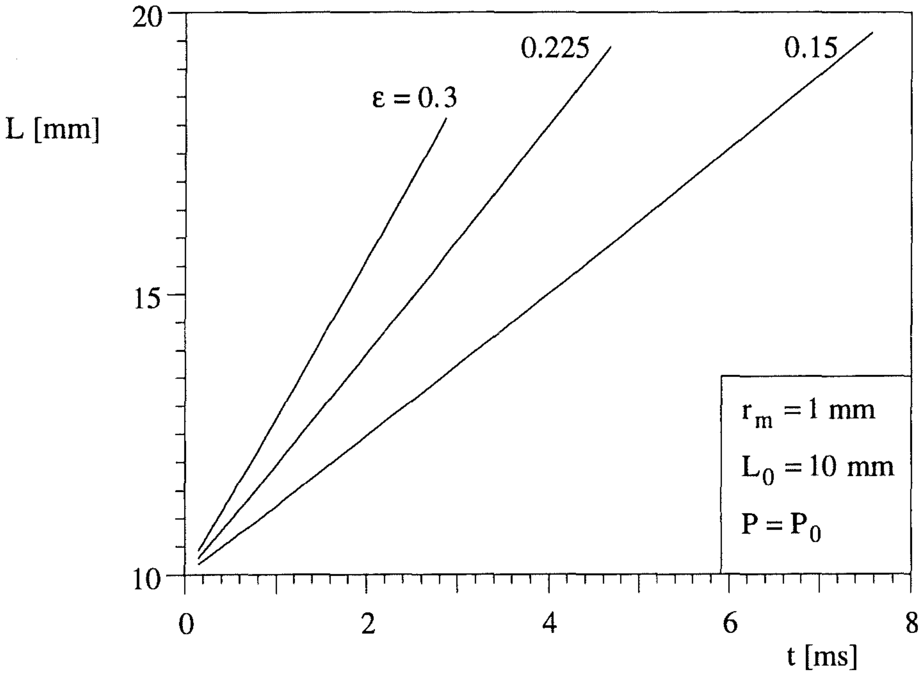

Figure 19. The effect of the mass fraction of molten material on the evolution of the thickness of the one-dimensional mixture layer.

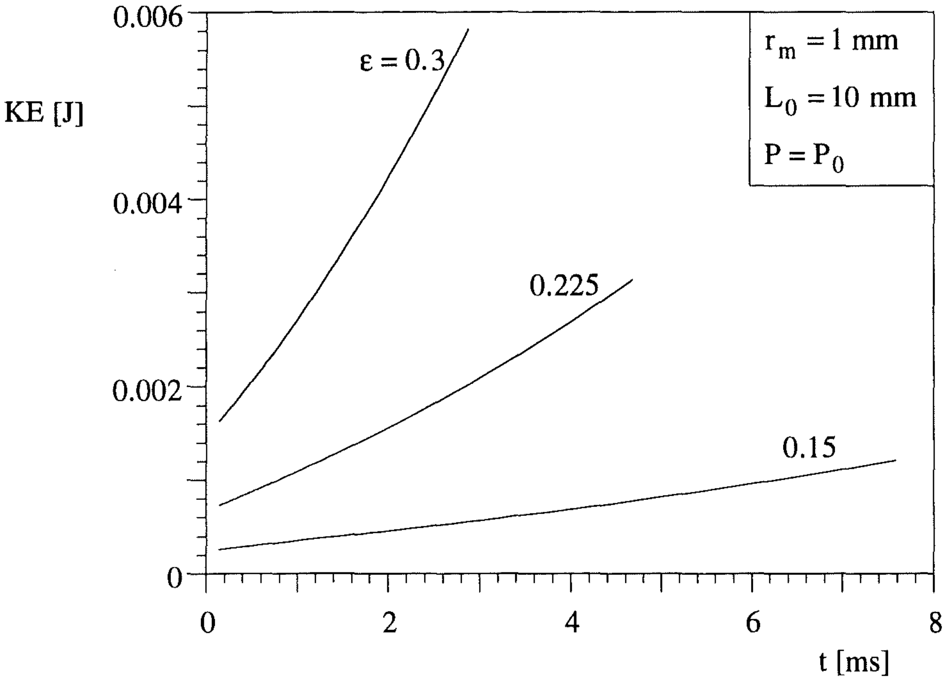

Figure 20. The effect of the mass fraction of molten material on the kinetic energy of the mixture sample of initial volume L_0^3.

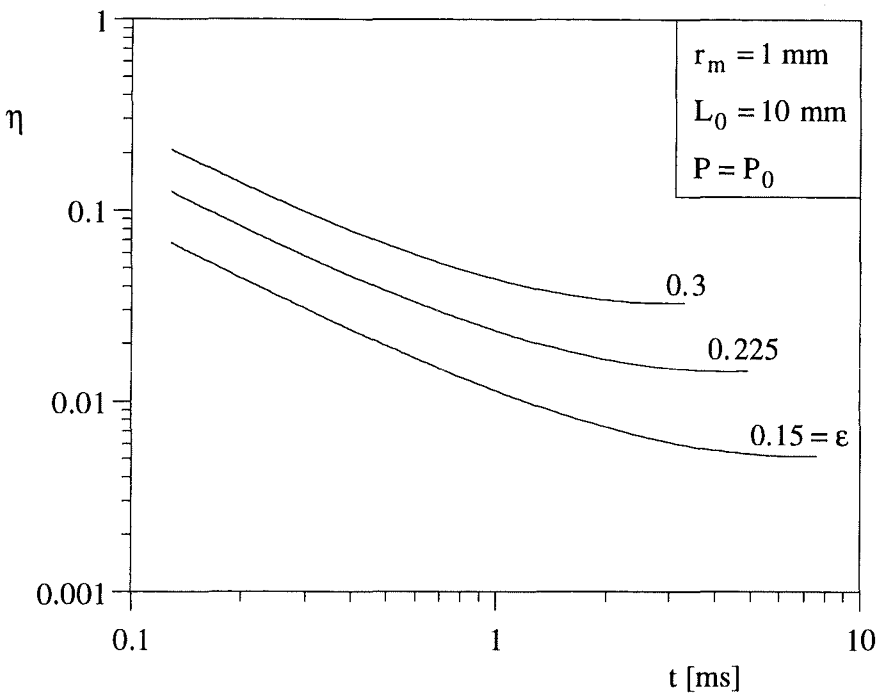

Figure 21. The effect of the mass fraction of molten material on the energy conversion efficiency.

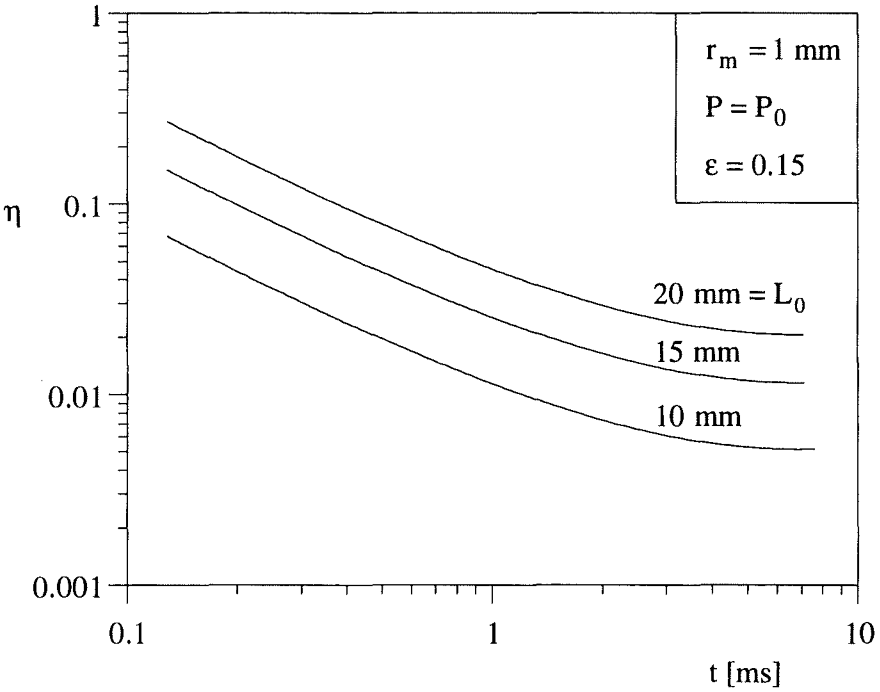

Figure 22. The effect of the thickness of the mixture layer on the energy conversion efficiency.

The effect of varying the radius of the molten droplet (r_m) is illustrated in Figs. 23 and 24. The remaining parameters are fixed at the values of the example of Fig. 18. For example, the radii 0.5, 1 and 1.5 mm correspond to N = 80, 10 and, respectively, 3 in the unit mixture volume L_0^3. In Fig. 23 we see that the expansion is considerably faster when r_m is small. This is a direct consequence of the effect of heat transfer enhancement: the fixed amount of molten material (ε) has a better thermal contact with its surroundings when its length scale (r_m) is small. The end of each line in Fig. 23 indicates the time when the validity of the model expires (Fig. 11b).

The thermodynamic efficiency of the heating and expansion process is reported in Fig. 24. The efficiency decreases almost as t^{-1}, and then reaches a plateau close to the time when adjacent sphere annuli come in contact. Figure 24a shows that if η is plotted against the dimensionless time $\tilde{t}$ the size of the molten sphere has a relatively small effect at small times. At large times, the efficiency is lower when r_m is smaller. The same results are plotted in Fig. 24b with the real time on the abscissa. This figure reinforces the conclusion drawn based on Fig. 23: the process is faster when r_m is smaller.

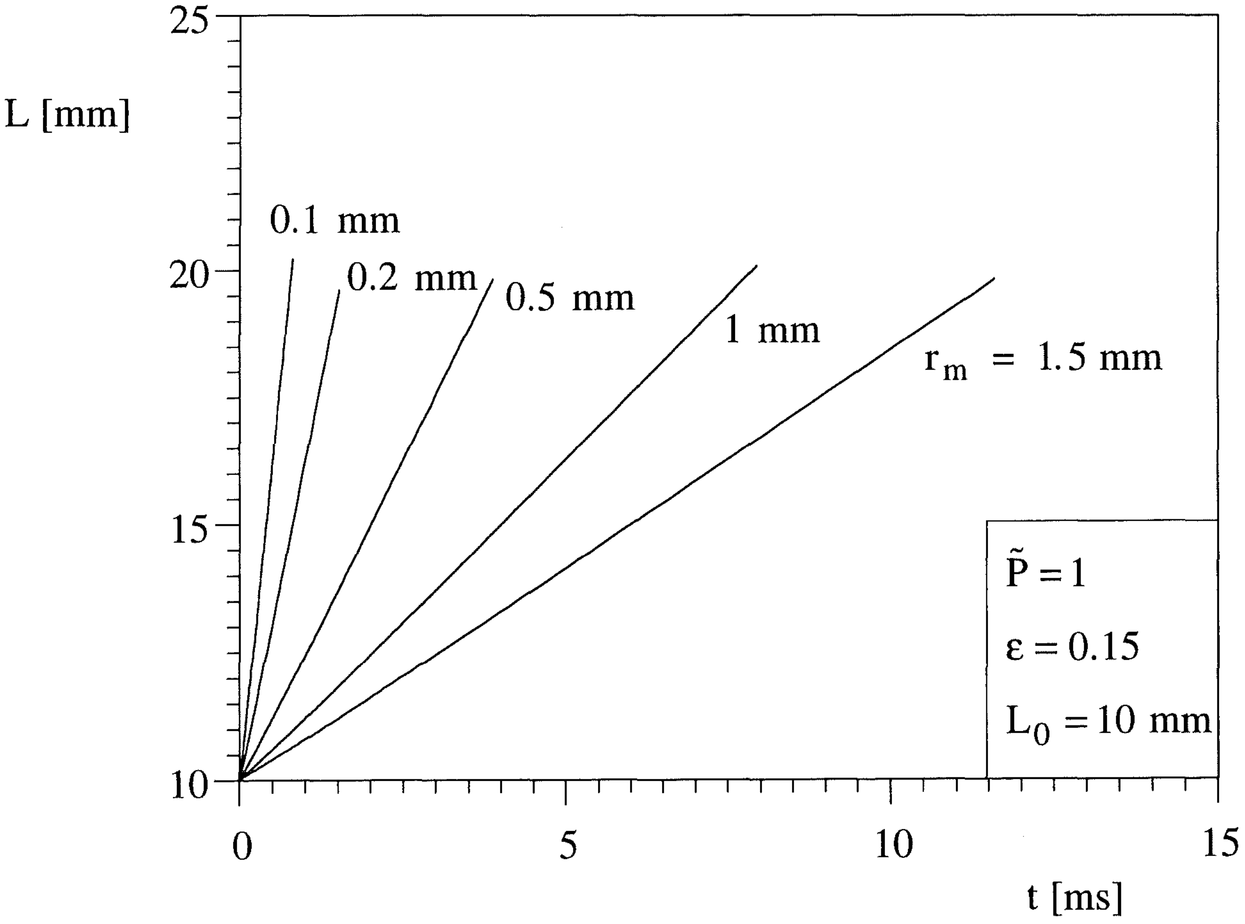

Figure 23. The effect of the size of the molten droplet on the evolution of the thickness of the mixture layer.

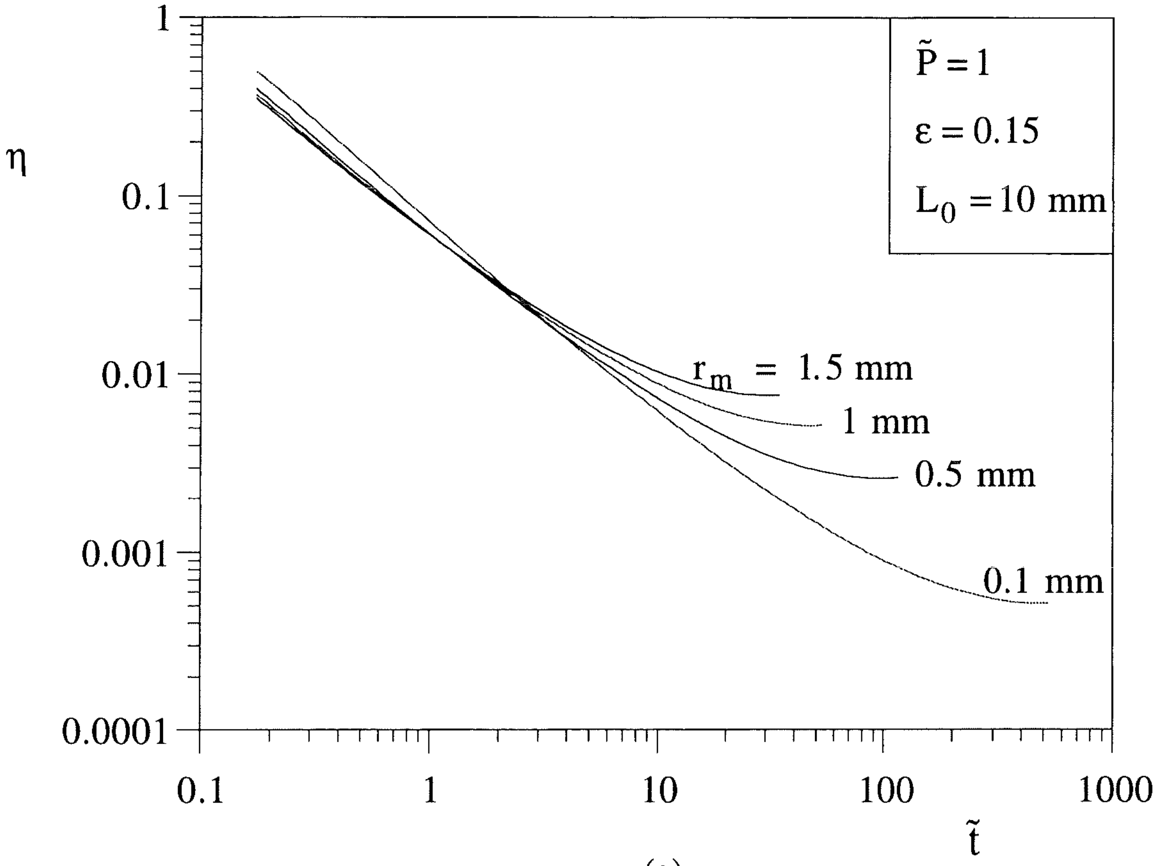

(a)

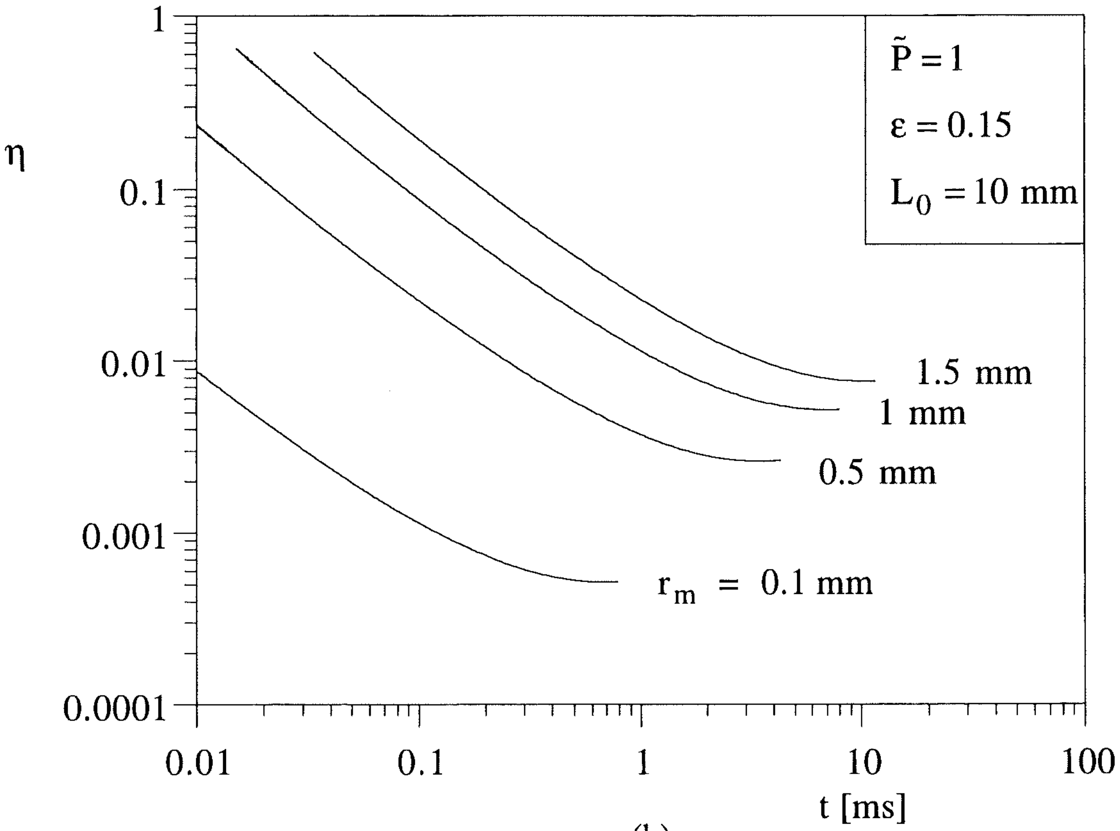

(b)

Figure 24. The effect of the size of the molten droplet on the energy conversion efficiency.

In Fig. 25, we tested the assumption that the steam annulus pressure can be decoupled from the mixture pressure in the time-dependent simulation of the mixture expansion process. In this test we continued to assume that the elemental-system steam pressure ($\tilde{P}$, constant) is decoupled from the mixture pressure field $\tilde{P}(\tilde{y}, \tilde{t})$, however, this time we assigned values between 1 and 1.2 to the constant elemental pressure $\tilde{P}$.

Figure 25 shows that the estimated efficiency decreases as assumed $\tilde{P}$ constant increases. This conclusion is important, because it means that the $\tilde{P} = 1$ value used to generate Figs. 14 - 24 is the most conservative choice that can be made with respect to anticipating the efficiency. In the actual mixture, $\tilde{P}$ is always 1 near the free surface, and only slightly higher near the solid wall. For example, in the run documented in Fig. 14, the pressure reached the maximum value $\tilde{P} = 1.007$ at t = 0.3 ms. In conclusion, in the present simulations the use of the uniform pressure assumption (with $\tilde{P} = 1$) was justified for calculating $\tilde{r}_s(\tilde{t})$.

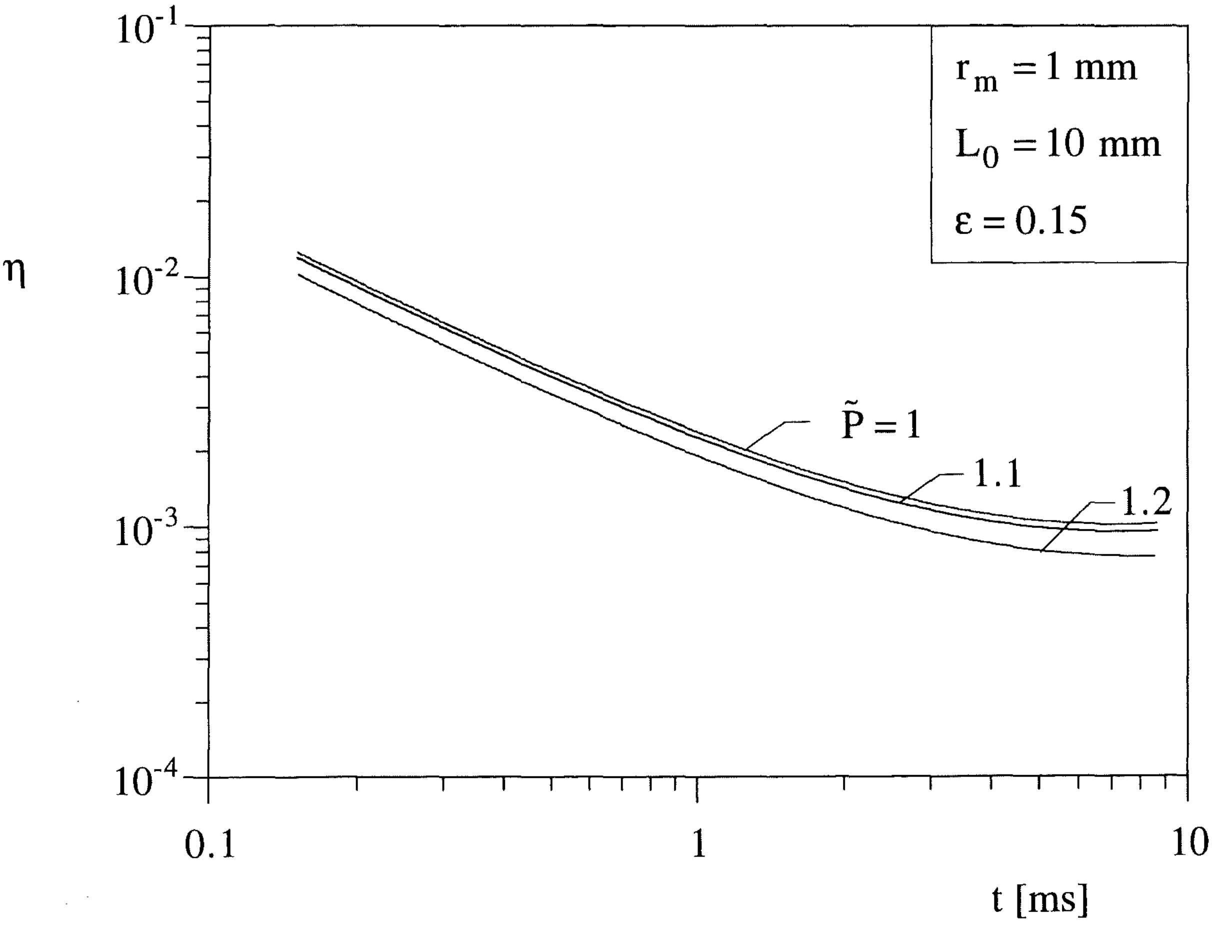

Figure 25. The effect of the assumed constant elemental pressure on the energy conversion efficiency.

4 EVOLUTION OF A FINITE-SIZE MIXTURE IMMERSED IN A WATER POOL

In this section we continue to describe numerically the time evolution of an expanding mixture of hot spherical particles, steam and water. The mixture expands against a body of water, in which it is immersed (Fig. 26). The numerical procedure is based on moving finite element (MFE) procedure. The fluid particles, distributed throughout the domain, are moved in time in a Lagrangian manner to simulate the change of the domain configuration. Three configurations are studied numerically: cylindrical mixture volume immersed in a cylindrical water pool, plane mixture layer held under a layer of water, and hemispherical mixture volume at the bottom of a much larger water pool.

4.1 Mathematical Formulation

Consider a mixture of molten material, water and steam. The mixture is immersed in a water pool, Fig. 26. In time, the heat transfer from the molten material causes the evaporation of some of the liquid water. The steam volume increases and the mixture volume expands in time. The expanding mixture acts like a piston that pushes the water pool. This is a moving boundary problem: one of the unknowns is the shape of the mixture domain (or mixture-water interface) during the expansion process. For the analysis of the moving boundary problem we apply the well known principle of "following the particle motion." The time derivatives of the objective function (velocity potential) in the moving frame are expressed in terms of the time derivatives of the function in the fixed frame together with a term arising from the velocity of the frame itself. In this problem the frame velocities are not prescribed but are to be generated by the method.

The problem is formulated in terms of the unknown velocity potential function Φ for irrotational compressible flow. The mass conservation equation for the domain presented in Fig. 26 requires,

$$\nabla^2 \Phi = S(t) \tag{70}$$

where S(t) is the source term, which is a function of time

$$S(t) = -\frac{1}{\rho}\frac{\partial \rho}{\partial t} \tag{71}$$

The velocity field follows from the general representation of an irrotational field,

$$\vec{v} = \nabla \Phi \tag{72}$$

The source term S(t) of Eq. (70) is unknown. To solve the problem, this term must be known *a priori* as a function of time in the mixture domain. In the water, which is assumed incompressible, this term is zero.

The elemental mixture model is the same as in section 3.1: for clarity, we repeat the key assumptions here. The mixture is composed of a number of N elemental systems. Each elemental system consists of a spherical melt droplet with a specified radius (r_m), surrounded by a spherical layer of steam and immersed in liquid water, Fig. 11a. The steam radius is time-dependent, $r_s(t)$. The volumes occupied by the melt, steam and liquid water in the volume of one elemental mixture system are given by Eqs. (37) and (38), where m_{w0} is the initial mass of the water (all in liquid form) and m_s is the steam mass. The density of the water is ρ_w, while $\overline{\rho}_s$ is the density of the steam averaged over the steam volume V_s. The instantaneous density of the mixture can be calculated from

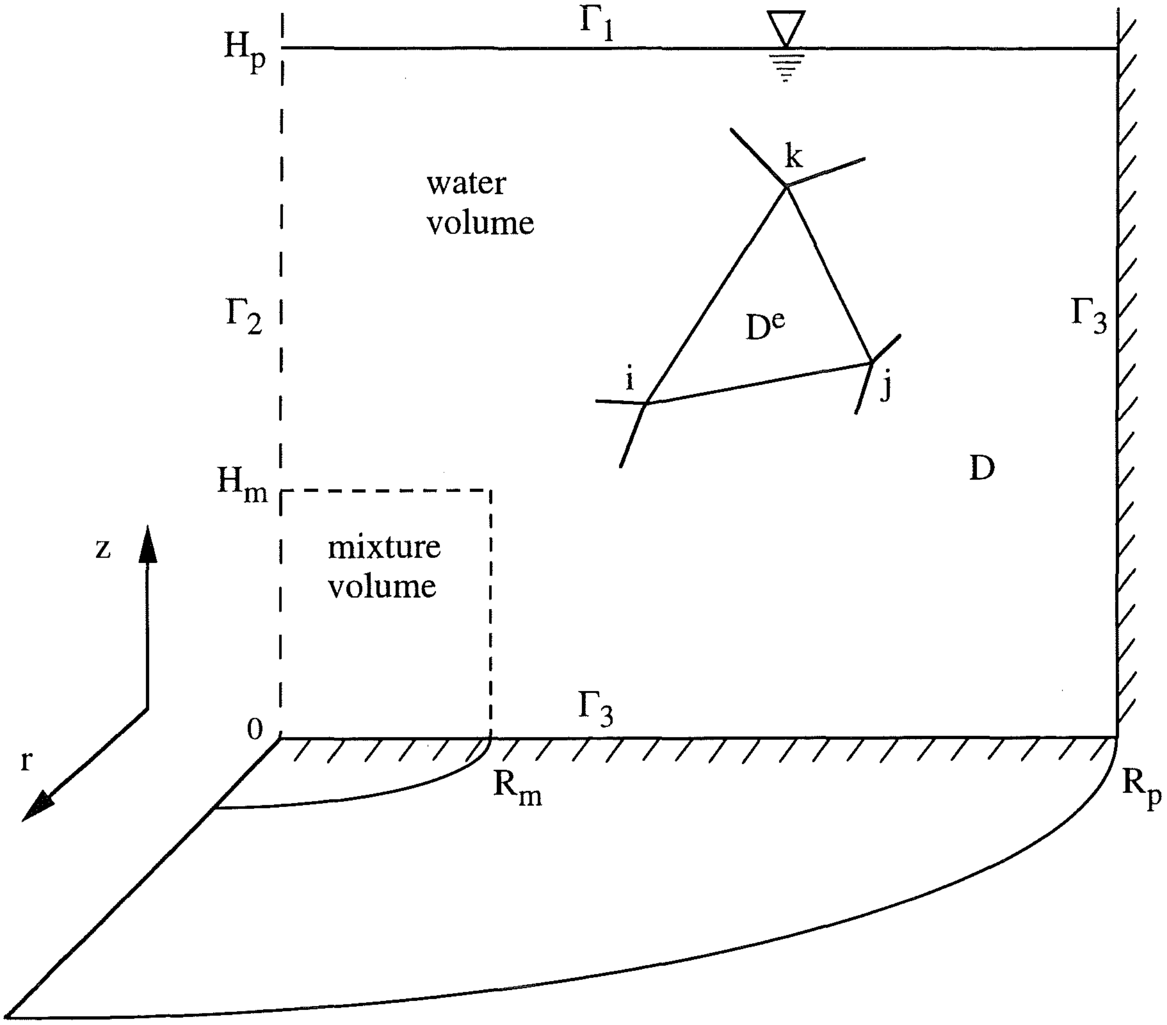

Figure 26. Two-dimensional space in which a cylindrical mixture volume is immersed in a water pool.

$$\rho = \frac{m_m + m_s + m_w}{V_m + V_s + V_w} \tag{73}$$

The result can be expressed as a specific volume, Eq. (40), where the melt mass fraction $\varepsilon = m_m / m$ is a specified constant. The order of magnitude of the time when the Fig. 11a scenario ends can be estimated with the cubic model of Fig. 11b: at this time the steam annuli become tangent. The volume averaged mixture density at this moment is given by Eq. (42).

The steam radius $r_s(t)$ can be calculated using the model described in connection with Fig. 13. According to this model, the radial heat transfer and steam motion inside the steam annulus are governed by mass and energy conservation equations (46, 47). By eliminating the right side of Eq. (46) between Eqs. (46) and (47), and integrating away from $r = r_m$ where u is zero, we find Eq. (48). In this equation the steam thermal conductivity k is a function of temperature and $k_m = k\,(T_m)$. At the liquid water interface the balance between the heat transfer (radiation and conduction) from the steam side and the latent heat of the vaporized liquid yields, cf. Eqs. (49, 50), where ρ_s is the steam density at saturation (T_s).

Equations (46)–(50) are sufficient for determining T, u, and, finally, r_s for each elemental system, provided the steam pressure P is specified. The initial and boundary conditions are $r_s = r_m$ at $t = 0$, $T = T_m$ at $r = r_m$ and $T = T_s$ at $r = r_s$. The thermal conductivity of the steam is correlated to the temperature cf. Eq. (58), where T is expressed in kelvin. The analytical details of the algorithm are omitted for brevity. The r_s value for the next time step is obtained from Eqs. (49, 50) by using a forward Euler time discretization scheme. The moving front $r = r_s$ is considered in the algorithm by using a time dependent grid spacing preserved by front-tracking procedure. The calculated r_s values and Eq. (40) provide the mixture density $\rho(t)$ and the source term, Eq. (71).

4.2 Method of Solution

For the fixed (Eulerian) frame we solved the boundary value problem (70) of the axisymmetric domain of Fig. 26 by using the Galerkin finite element method with first-order triangular elements. We assumed that the mixture and the surrounding water are immiscible, and both fluids (mixture, water) are inviscid. With reference to the system of coordinates shown in Fig. 26, Eq. (70) can be written as

$$\frac{\partial^2 \Phi}{\partial r^2} + \frac{1}{r}\frac{\partial \Phi}{\partial r} + \frac{\partial^2 \Phi}{\partial z^2} = S(t) \tag{74}$$

where S(t) is the source term:

$$\begin{aligned} S(t) &= -\frac{1}{\rho}\frac{\partial \rho}{\partial t} \text{ in the mixture} \\ S(t) &= 0 \text{ in the water} \end{aligned} \tag{75}$$

The Galerkin residual method was executed in the following steps:

1. Divide the domain D (mixture and water) into n_{el} triangular elements.
2. Assume that over each finite element Φ varies as

$$\Phi^e(r,z) = \sum_{a=1}^{3} N_a(r,z)\,\Phi_a^e \tag{76}$$

where N_a are the shape functions.

3. Satisfy the criterion that the residue must be zero, which yields

$$\left[K^e\right]\left\{\Phi^e\right\} = \left\{f^e\right\} \tag{77}$$

where

$$\left[K^e\right] = \frac{\pi r_c^2}{2A^e}\begin{pmatrix} \left(b_1^2 + c_1^2\right) & \left(b_1 b_2 + c_1 c_2\right) & \left(b_1 b_3 + c_1 c_3\right) \\ & \left(b_2^2 + c_2^2\right) & \left(b_2 b_3 + c_2 c_3\right) \\ & & \left(b_3^2 + c_3^2\right) \end{pmatrix} \tag{78}$$

Note that A^e is the elemental triangular area

$$A^e = \frac{1}{2}\left| r_i\left(z_j - z_k\right) + r_j\left(z_k - z_i\right) + r_k\left(z_i - z_j\right)\right| \tag{79}$$

and the coefficients (a_i, b_i, c_i) are shorthand for

$$\begin{aligned} a_1 &= r_j z_k - r_k z_j \qquad & b_1 &= z_j - z_k \qquad & c_1 &= r_k - r_j \\ a_2 &= r_k z_i - r_i z_k \qquad & b_2 &= z_k - z_i \qquad & c_2 &= r_i - r_k \\ a_3 &= r_i z_j - r_j z_i \qquad & b_3 &= z_i - z_j \qquad & c_3 &= r_j - r_i \end{aligned} \tag{80}$$

where i, j and k represent the local elemental triangle indexes, Fig. 26, and

$$\{f^e\} = -\frac{SA^e \pi r_c}{6} \begin{pmatrix} (2r_i + r_j + r_k) \\ (r_i + 2r_j + r_k) \\ (r_i + r_j + 2r_k) \end{pmatrix} \tag{81}$$

The factor

$$r_c = \int\int_{D^e} r^2 \, d\, A^e \tag{82}$$

is approximated by the centroidal value

$$r_c = \frac{1}{3}\left(r_i + r_j + r_k\right) \tag{83}$$

4. Assemble the elemental equations, to obtain the overall system of equations.
5. Solve the general system of equations using the Choleski decomposition direct method.

Consider two successive time steps, t and t + Δt, and assume that a fluid particle moves from (r, z) to (r', z'). In the moving frame, the new coordinates (r', z') are obtained from a truncated Taylor series expansion about (r, z, t) [37],

$$r' = r + \Delta t \frac{Dr}{Dt} \tag{84}$$

$$z' = z + \Delta t \frac{Dz}{Dt} \tag{85}$$

where D / Dt denotes the Lagrangian time differentiation. The time increment is calculated at each time step from the Courant-Friedrichs-Lewy (CFL) condition. Similarly, at the new time step the new velocity potential function can be approximated as

$$\Phi' = \Phi + \Delta t \frac{D\Phi}{Dt} \tag{86}$$

The Lagrangian derivatives of r and z are

$$\frac{Dr}{Dt} = v_r = \frac{\partial \Phi}{\partial r} \qquad \frac{Dz}{Dt} = v_z = \frac{\partial \Phi}{\partial z} \tag{87}$$

After the velocity potential values are determined at each node of the triangular mesh, the velocities v_r and v_z are computed on each triangular element,

$$v_r^e = \frac{\partial \Phi}{\partial r} = \frac{1}{2A^e}\left(b_1 \Phi_i + b_2 \Phi_j + b_3 \Phi_k\right) \tag{88}$$

$$v_z^e = \frac{\partial \Phi}{\partial z} = \frac{1}{2A^e}\left(c_1 \Phi_i + c_2 \Phi_j + c_3 \Phi_k\right) \tag{89}$$

In these equations A^e denotes the element area. The velocity potential is assumed to have a linear variation on each element, and consequently, the velocity components in each triangle are constant. The velocities appearing in the Lagrangian derivatives of r and z are the velocities at the mesh nodes

$$v_r = \frac{1}{n_{el}} \sum_{a=1}^{n_{el}} (v_r)_a^e \qquad v_z = \frac{1}{n_{el}} \sum_{a=1}^{n_{el}} (v_z)_a^e \tag{90}$$

where n_{el} denotes the number of elements adjacent to each mesh node. The Lagrangian derivative of the velocity potential function is

$$\frac{D\Phi}{Dt} = \frac{\partial \Phi}{\partial t} + v_r \frac{\partial \Phi}{\partial t} + v_z \frac{\partial \Phi}{\partial t} = \frac{\partial \Phi}{\partial t} + \left(v_r^2 + v_z^2\right) \tag{91}$$

The first order Eulerian derivative $\Phi_t = \partial \Phi / \partial t$ can be found by differentiating Eq. (74) with respect to time

$$\frac{\partial^2 \Phi_t}{\partial r^2} + \frac{1}{r}\frac{\partial \Phi_t}{\partial r} + \frac{\partial^2 \Phi_t}{\partial z^2} = \dot{S}(t) \tag{92}$$

The time derivative of the source term $\dot{S}(t)$ is known. The finite element algorithm is repeated one more time in order to compute Φ_t at the mesh nodes. Worth noting is that the global matrix assembled for solving the linear system of equations for Φ is identical to the global matrix for Φ_t.

4.3 Results in cylindrical coordinates

The algorithm was used to simulate the evolution of several mixture-water systems. The parameter that varied was the radius of the hot spheres (melt droplets) contained in the mixture volume. The physical dimensions and parameters that were held fixed are presented in Table 1. The variation in time of the mixture density, which is necessary for the calculation of the source term, is presented in Fig. 27. The radius r_m was set at 0.5, 0.1 and 0.05 mm. We fixed the relative amount of hot material ($\varepsilon = 0.15$). Figure 27 shows that the mixture expansion is considerably faster when r_m is small. The end of each curve indicates the time when the validity of the elemental volume model expires, that is when the adjacent steam layers touch (Fig. 11b).

For subsequent calculations it was convenient to curve-fit with exponential polynomials the numerical data obtained for the mixture density:

$$\rho_{\text{analytical}} = \sum_{i=1}^{n} c_i \exp\left(-\lambda_i\, t\right) \tag{93}$$

An accurate fit is obtained with n = 2. The accuracy is defined as

$$\varepsilon_r = \frac{\left|L_2(\rho) - L_2\left(\rho_{\text{analytical}}\right)\right|}{\left|L_2(\rho)\right|} \tag{94}$$

where L_2 is the euclidean norm of vector solutions, and ε_r is of order 10^{-4}. The agreement between $\rho_{\text{analytical}}$ and the numerical ρ data is very good, as illustrated in Fig. 27. The coefficients calculated for the density function (93) are

$$\begin{array}{lllll} r_m = 0.5\ \text{mm:} & c_1 = 473.85 & c_2 = 645.96 & \lambda_1 = 455.73 & \lambda_2 = 74.24 \\ r_m = 0.1\ \text{mm:} & c_1 = 480.91 & c_2 = 636.72 & \lambda_1 = 2255.3 & \lambda_2 = 363.9 \\ r_m = 0.05\ \text{mm:} & c_1 = 458.11 & c_2 = 661.37 & \lambda_1 = 4657.8 & \lambda_2 = 774.8 \end{array} \tag{95}$$

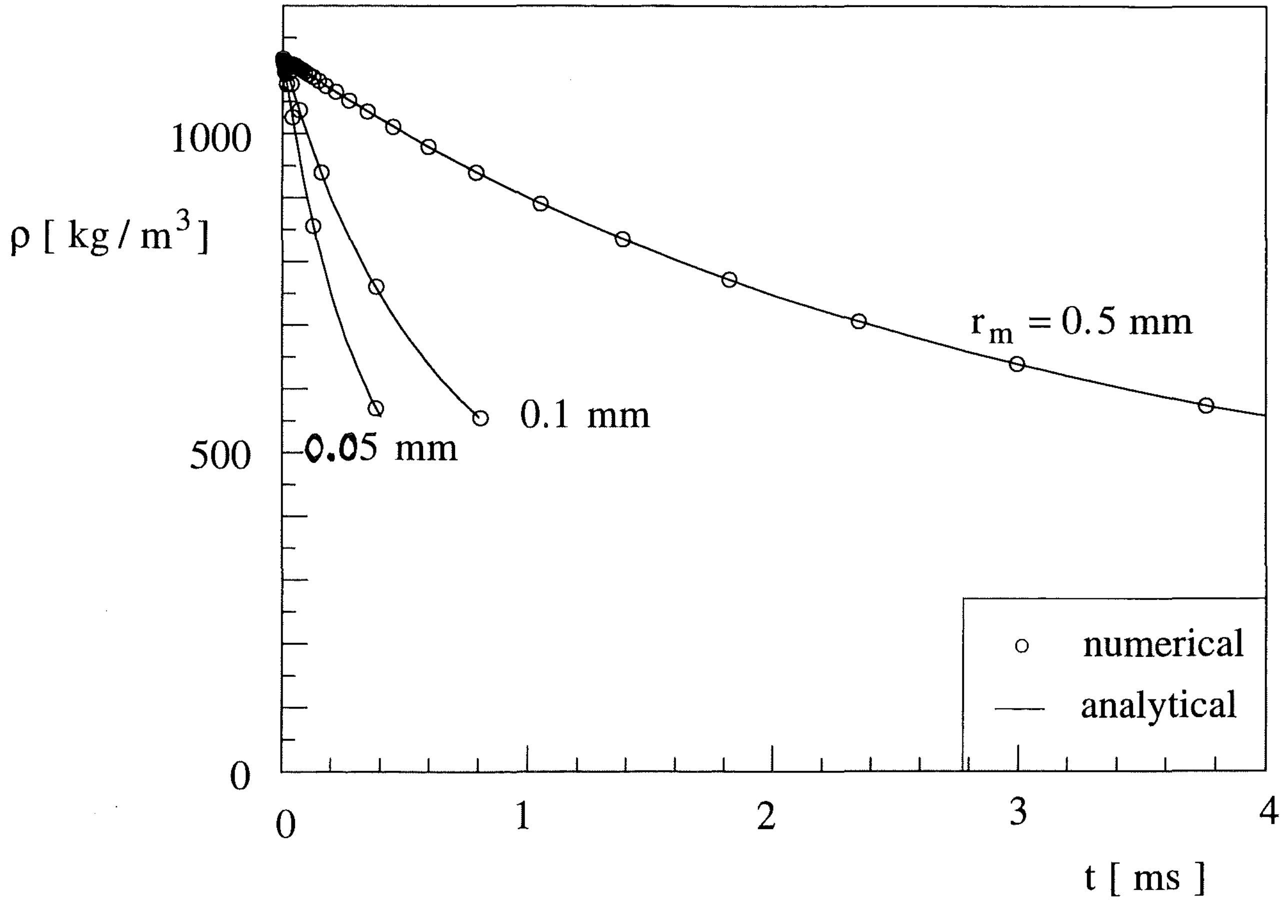

Figure 27. The time-evolution of the mixture density.

For the configuration of Fig. 26 we assumed the following dimensions: mixture radius R_m = 10 mm, mixture height H_m = 10 mm, pool radius R_p = 40 mm and pool height H_p = 40 mm. A coarse triangular mesh was first constructed as shown in Fig. 28a (number of elements ne = 800; number of nodes nn = 441). In order to increase the accuracy of the solution without increasing the order of the interpolating polynomial, the initial mesh was refined automatically in the code. The refined mesh is presented in Fig. 28b (ne = 3200, nn = 1681). We studied the convergence by comparing the solutions obtained on the coarse grid and on the refined grid. Two other meshes having different node indexing are shown in Figs. 28c and 28d. The correctness of the algorithm and the convergence were also tested using these finite element meshes.

The boundary conditions for Φ relative to the domain shown in Fig. 26 are

$$\frac{\partial \Phi}{\partial n} = 0 \quad \text{on} \quad \Gamma_2 \cup \Gamma_3 \tag{96}$$

$$\Phi^k = \Phi^{k-1} \quad \text{on} \quad \Gamma_1 \tag{97}$$

where n is the boundary normal and k denotes the time step. The boundary conditions for Φ_t are

$$\frac{\partial \Phi_t}{\partial n} = 0 \quad \text{on} \quad \Gamma_2 \cup \Gamma_3 \tag{98}$$

$$\Phi_t = -0.5\left(v_r^2 + v_z^2\right) \quad \text{on} \quad \Gamma_1 \tag{99}$$

During the expansion the number of mesh elements remains unchanged, while the node coordinates and the triangular element areas change. Figure 29 shows the mesh state at the end of the expansion process, where for better illustration the entire cross section of the pool is shown. The velocity distribution in the domain (mixture and water) is presented in Fig. 30 for the case r_m = 0.05 mm, at the end of the expansion process ($t \approx 0.4$ ms). The maximum velocity is approximately 4 m/s, and occurs at the mixture-water interface. Additional simulations showed that the velocities are smaller when the particle size r_m is larger.

A three-dimensional representation of the constant vector potential lines is shown in the upper part of Fig. 31. These lines were obtained after solving the global system of equations, and were drawn by using a two-dimensional interpolation for the nodal potential values. The velocities are proportional to the gradient of the potential. The vector representation of the velocity is shown in the lower part of Fig. 31. The vector moduli are proportional to the actual velocity. Figure 31 was drawn for the molten radius r_m = 0.05 mm. We controlled the step size by enforcing the Courant-Friedrichs-Lewy condition [38]

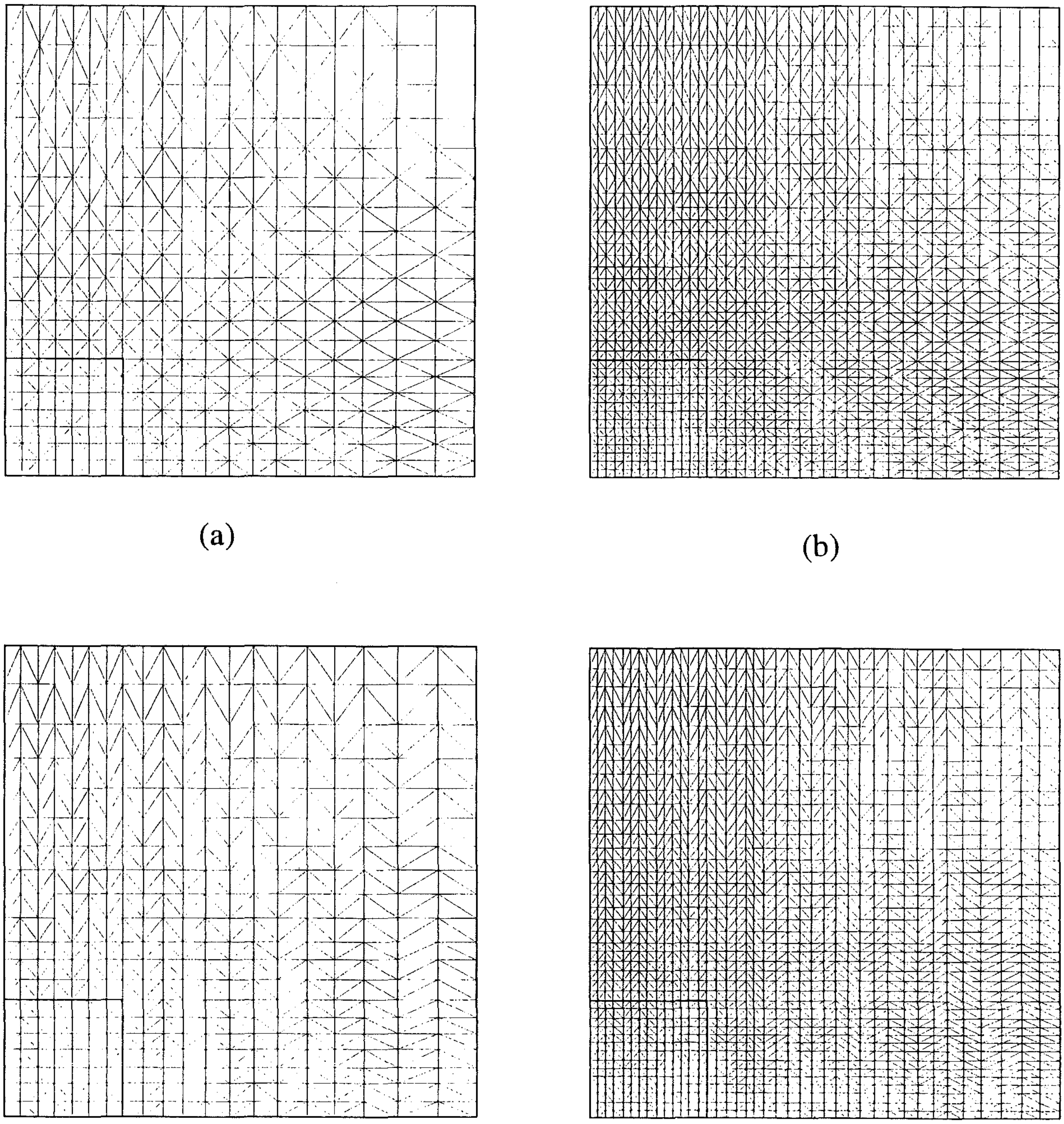

(a)

(b)

(c)

(d)

Figure 28. The triangular meshes tried (a, c, d), and the one used (b).

$$u_{max} \frac{\Delta t}{\Delta s} \leq 1 \tag{100}$$

where the u_{max} is the maximum velocity at the preceding time step, and Δs is the maximum distance covered by the fluid particle during one time step.

4.4 Energy conversion

An important aspect of the expansion process is the efficiency with which the energy released by the hot spheres is converted into kinetic energy in the moving mixture and water. The kinetic energy acquired by the entire system is

$$KE = \sum_{e=1}^{n_{el}} \frac{1}{2} m^e \left(v^e\right)^2 = 2\pi \sum_{e=1}^{n_{el}} \frac{1}{2} \rho^e r_c^e A^e \left(v^e\right)^2 \tag{101}$$

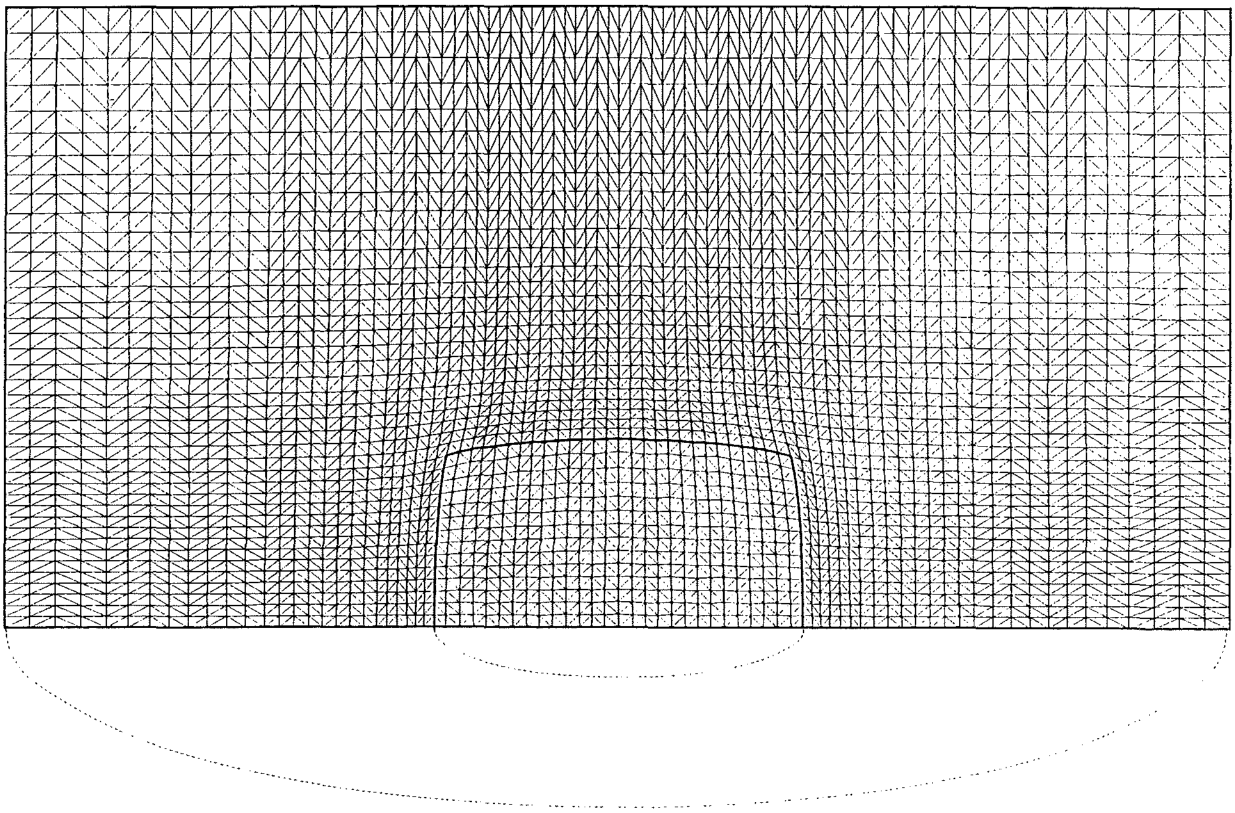

Figure 29. The deformed mesh at the time t = 4 ms, for $r_m = 0.5$ mm, $R_m = 10$ mm, $H_m = 10$ mm, $R_p = 40$ mm and $H_p = 40$ mm.

where n_{el} is the total number of triangular elements used for domain discretization, ρ^e is the density on each element and v^e is the elemental velocity. The kinetic energy is associated with elements (not with mesh nodes), and is constant in each element. The total kinetic energy is obtained at each time step from Eq. (101). The total volume is $V(t) = \pi R_p^2 H_p$, where the pool radius R_p and pool height H_p are functions of time because of the moving boundaries. The total kinetic energy histories are shown in Fig. 32 for the first 0.4 ms of the process.

The heat transfer rate was calculated for each hot sphere. First, the instantaneous heat transfer rate q is due to two contributions, conduction from the r_m sphere to the adjacent steam layer, and radiation from the sphere to the water front,

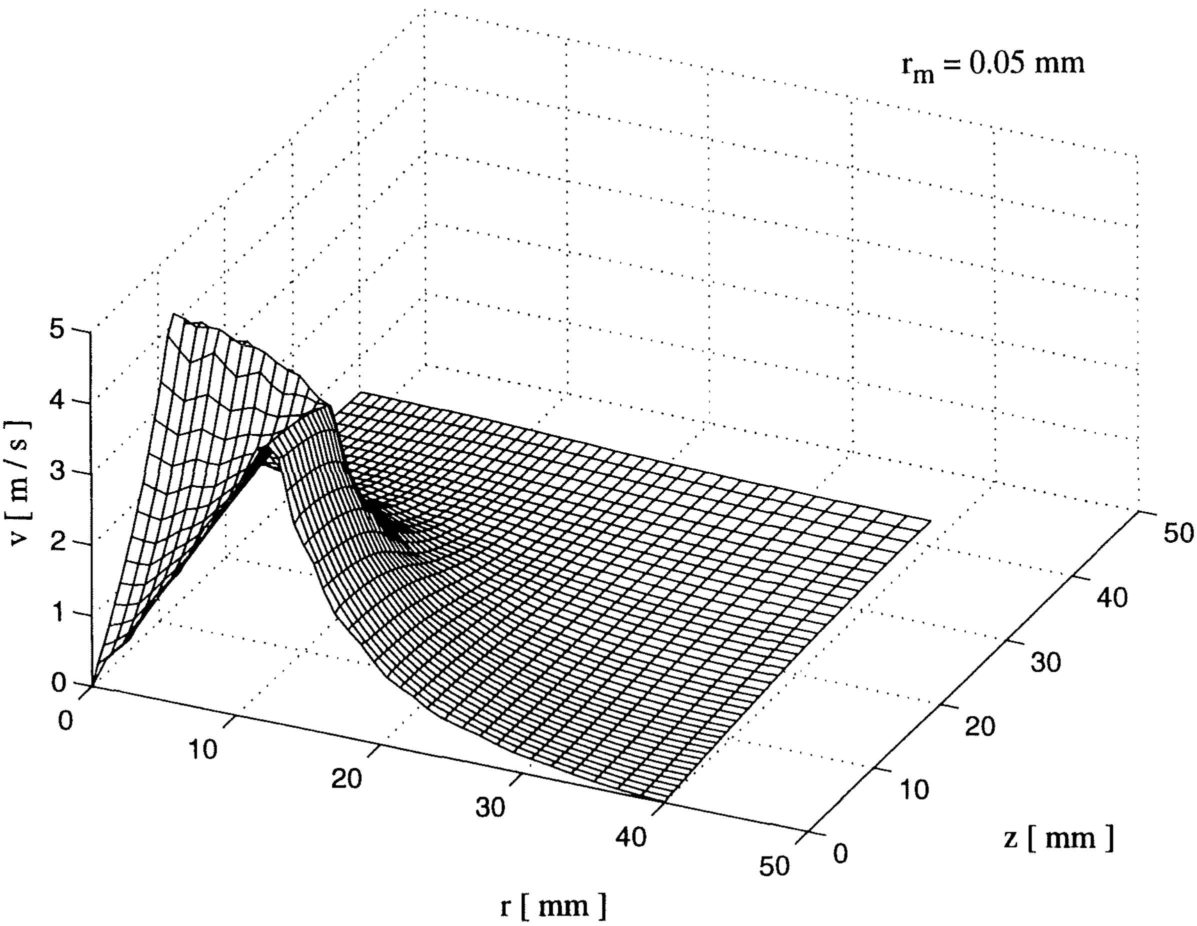

Figure 30. The velocity distribution in the mixture and water domain when the steam annuli touch (Fig. 11b).

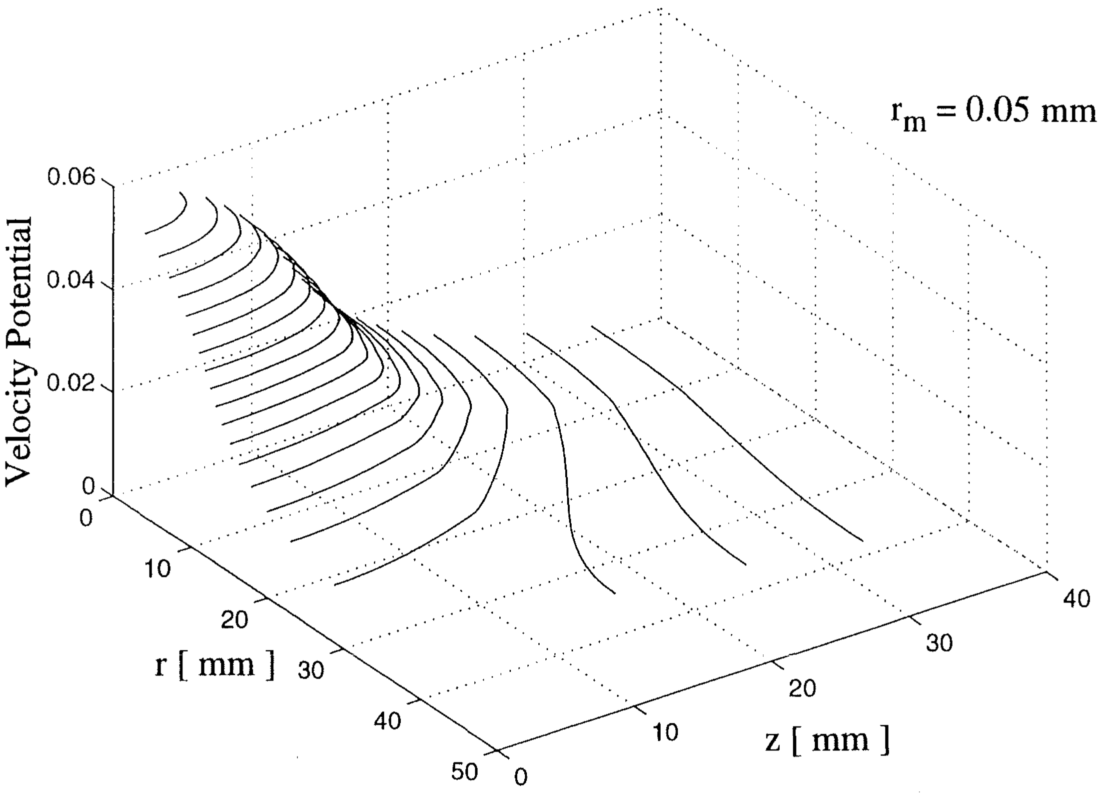

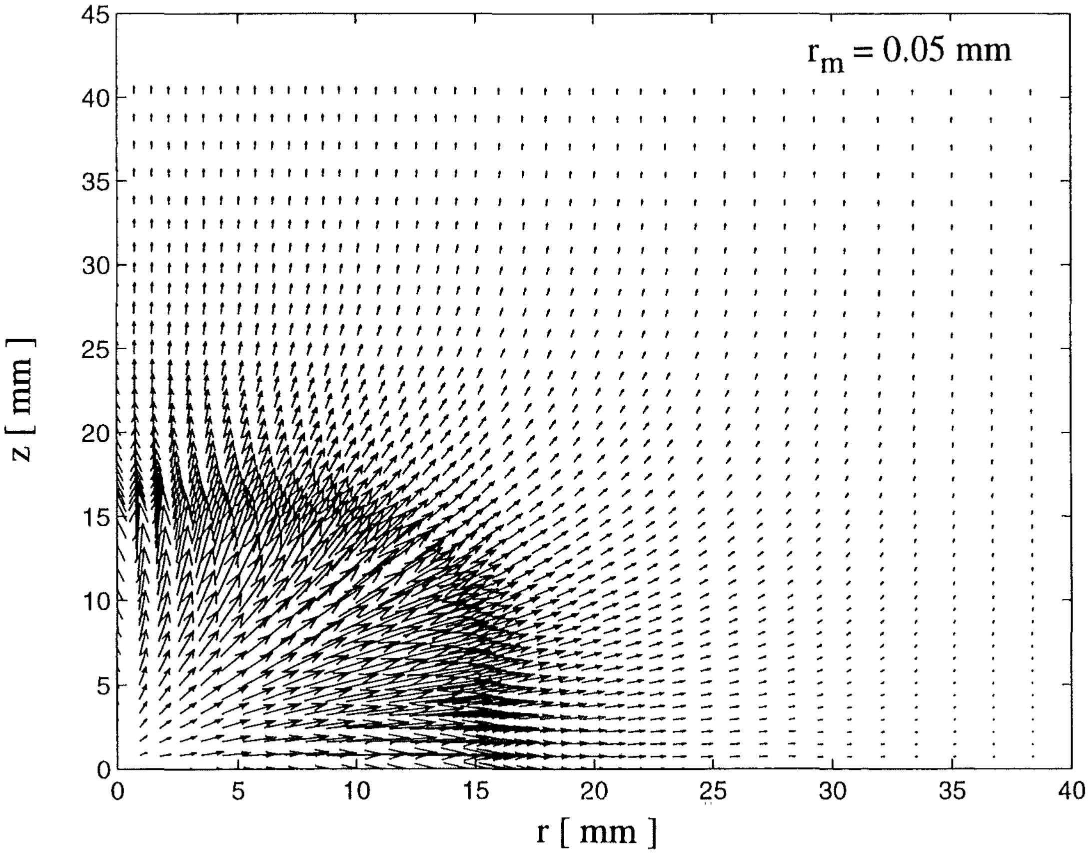

Figure 31. The velocity potential (top) and velocity vector (bottom) for the state described in Fig. 30.

$$q = q_{rad} + q_{cond} = \frac{4\pi r_m^2 \sigma \varepsilon_m \left(T_m^4 - T_s^4\right)}{1 + \left(r_m / r_s\right)^2 \varepsilon_m \left(\varepsilon_s^{-1} - 1\right)} + 4\pi r_s^2 k_s \left(-\frac{\partial T}{\partial r}\right)_{r_s} \tag{102}$$

The total heat release from the hot sphere is

$$Q = \int_0^t q\,dt \tag{103}$$

Figure 33 shows the Q(t) function and how it is affected by changes in r_m. Finally, the conversion efficiency is obtained by writing

$$\eta = \frac{KE}{NQ} \tag{104}$$

The number of hot spheres N contained in the given mixture volume follows from the definition of the mass fraction ε_m,

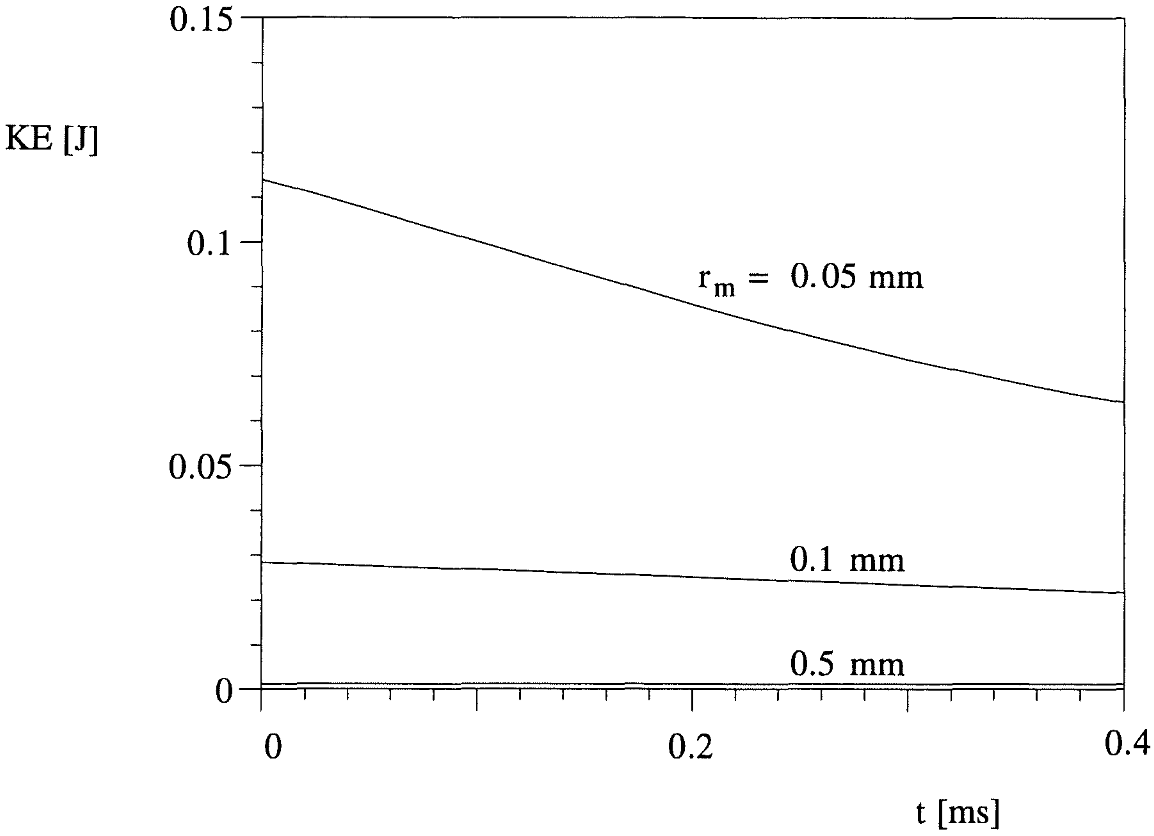

Figure 32. The time-evolution of the total kinetic energy.

$$N = \frac{\varepsilon_m \rho_w \pi R_m^2 H_m}{\rho_m (4\pi / 3) r_m^3} \tag{105}$$

The time evolution of the conversion efficiency is shown in the Fig. 34. The efficiency is higher at the start of the expansion process, and decreases sharply as the time increases. The particle size r_m has an important effect on the efficiency: η increases when r_m decreases. In other words, the energy conversion process is more efficient, and the KE inventory of the mixture is larger, when the contact area between the hot material and the surrounding water is larger.

In Fig. 35 we show another set of results that document the effect of increasing the relative size of the water pool (R_p, H_p). The mixture dimensions are held fixed at $r_m = 0.1$ mm, $R_m = 10$ mm and $H_m = 10$ mm. The effect of the water pool is relatively weak: the energy conversion efficiency decreases at a decreasing rate as the surrounding water pool becomes larger.

4.5 One-dimensional configurations

The preceding results refer to the configuration of Fig. 26, where the mixture expanded simultaneously in two directions, z and r. We studied the same phenomenon in two simpler configurations, which are shown in Fig. 36. In these configurations the expansion is unidirectional, vertically away from the wall in Fig. 36a, and radially away from the center of the hemispherical mixture volume in Fig. 36b. If we continue to curve-fit the elemental results for the density history cf. Eq. (93), then the solution for the mixture velocity field can be developed analytically. For brevity, we report only the results for energy conversion efficiency, in order to document the effect of changing the configuration of the mixture and water system.

In Fig. 37 we show the results for a mixture layer characterized by $r_m = 0.1$ mm, $H_m = 10$ mm and $\varepsilon = 0.15$. The height of the water pool increases from 10 mm to 50 mm and at the same time the efficiency increases. This means that unlike the two-dimensional space (Fig. 35), in Fig. 36a the water layer plays the role of an accelerated mass, and this translates into a less irreversible conversion process. The time dependence of η is the same as in Figs. 34 and 35, i.e., approximately as t^{-1}.

Figure 38 shows the behavior of the energy conversion efficiency in the hemispherical configuration of Fig. 36b in the limit $R_p / R_m \rightarrow \infty$. The mixture is characterized by $\varepsilon = 0.15$, $r_m = 0.1$ mm and R_m values in the range 10 mm - 50 mm. For example, when $R_m = 25$ mm the number of hot particles contained in the hemispherical mixture volume is 3.25×10^5. The efficiency decreases in time as t^{-1}, and increases as R_m increases.

4.6 Closing comments

In this section we documented the evolution of mixtures of hot particles, steam and water, when such mixtures are surrounded by liquid water. The method of solution is based on MFE in a Lagrangian manner. The algorithm is very economical compared to space-time finite element methods in which we deal in fact with a three-dimensional problem for a two-dimensional one. The only extra cost in our method consisted of solving one additional equation. The equation for the derivative of velocity potential function is easily solved by using Galerkin FEM one more time.

In this phase of our work the focus was on the thermodynamic inefficiency of the heat transfer process. For example, Figs. 34, 35, 37 and 38 showed that the efficiency is generally of the order of 1 percent when the time scale is of the order of 1 ms. We documented the effects associated with changing the dimensions of the hot particles, mixture volume and water pool. The elemental model of Fig. 11, in which hot particles and water are assumed dispersed through a finite-size volume before the expansion begins, places the process described in this paper at times longer than those associated with sudden, thermoacoustic effects [7, 39]. Future numerical studies may consider what happens at even longer times, specifically, after the moment depicted in Fig. 11b. In this final regime the volume of the expanding mixture will be dominated by steam.

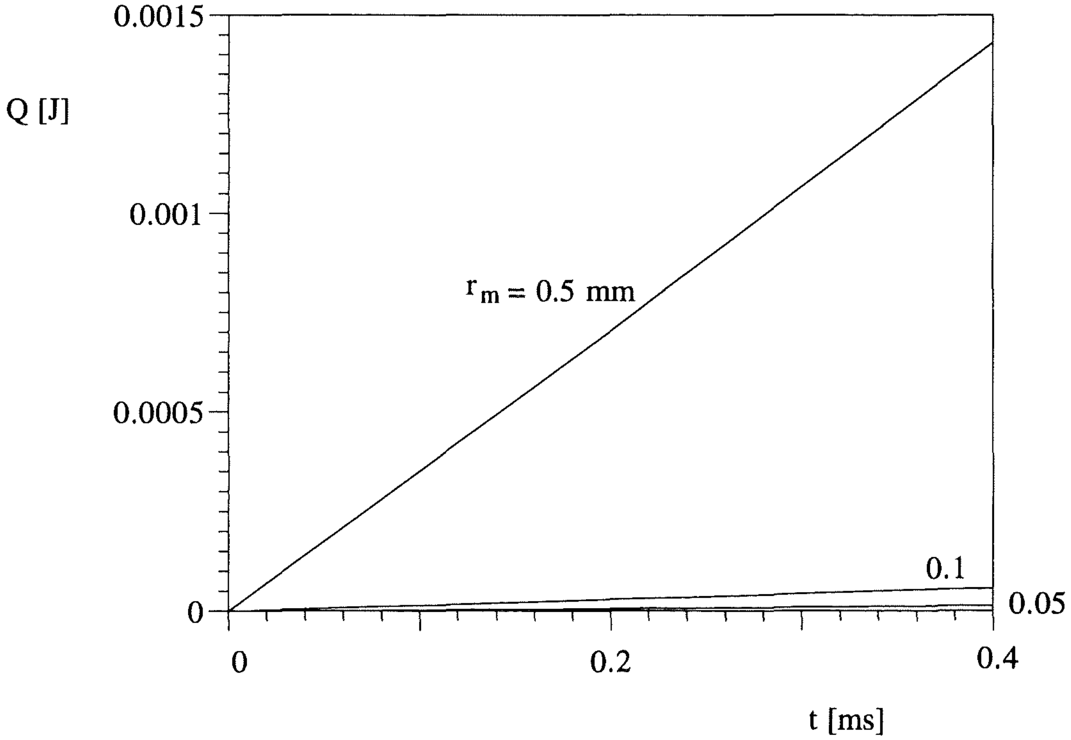

Figure 33. The time-evolution of the heat released from one hot sphere.

5 IRREVERSIBILITY DUE TO SUDDEN HEAT TRANSFER IN A STATIONARY MIXTURE

The work described in this section is based on the idea that *before* the melt and water mixture begins to expand, it achieves a state of mixing *en masse*, which occurs at constant volume. The melt particles are distributed throughout the mixture, and are effectively cooled to an "equilibrium" state that later serves as starting point for the expansion process.

During thermal mixing in the absence of fluid motion, a portion of the useful energy (exergy) of the melt and water system is destroyed. The calculation of this portion is the subject of this section. Other losses such as fluid friction and additional heat transfer, which occur subsequently during expansion, will add themselves to the destroyed exergy calculated in this section. Consequently, the energy conversion efficiency (or exergetic efficiency) described in this section is an *upper bound* for the efficiency of the actual, complete mixing and expansion process. It is a relative upper bound because it accounts for

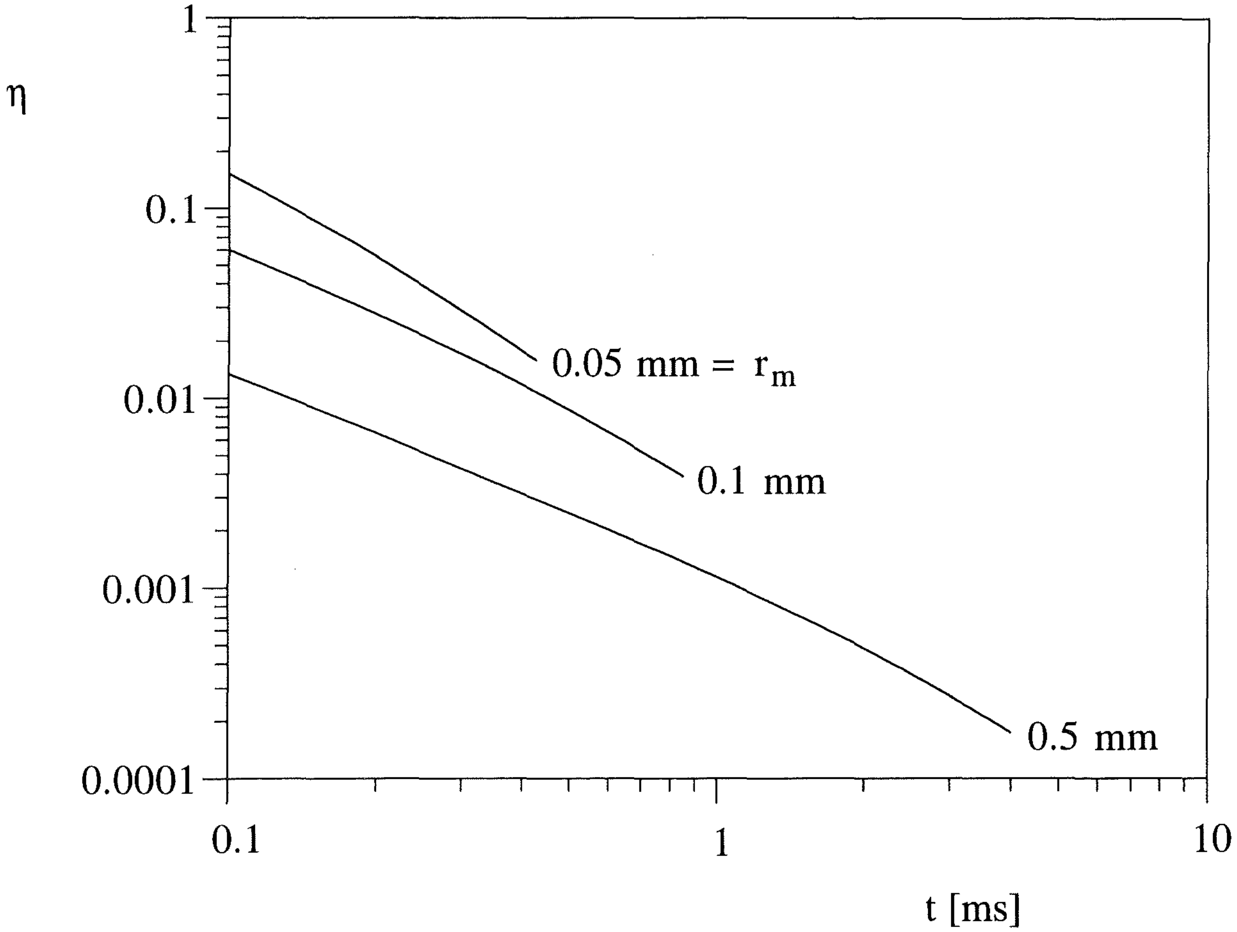

Figure 34. The energy conversion efficiency for the systems described by Figs. 30-33.

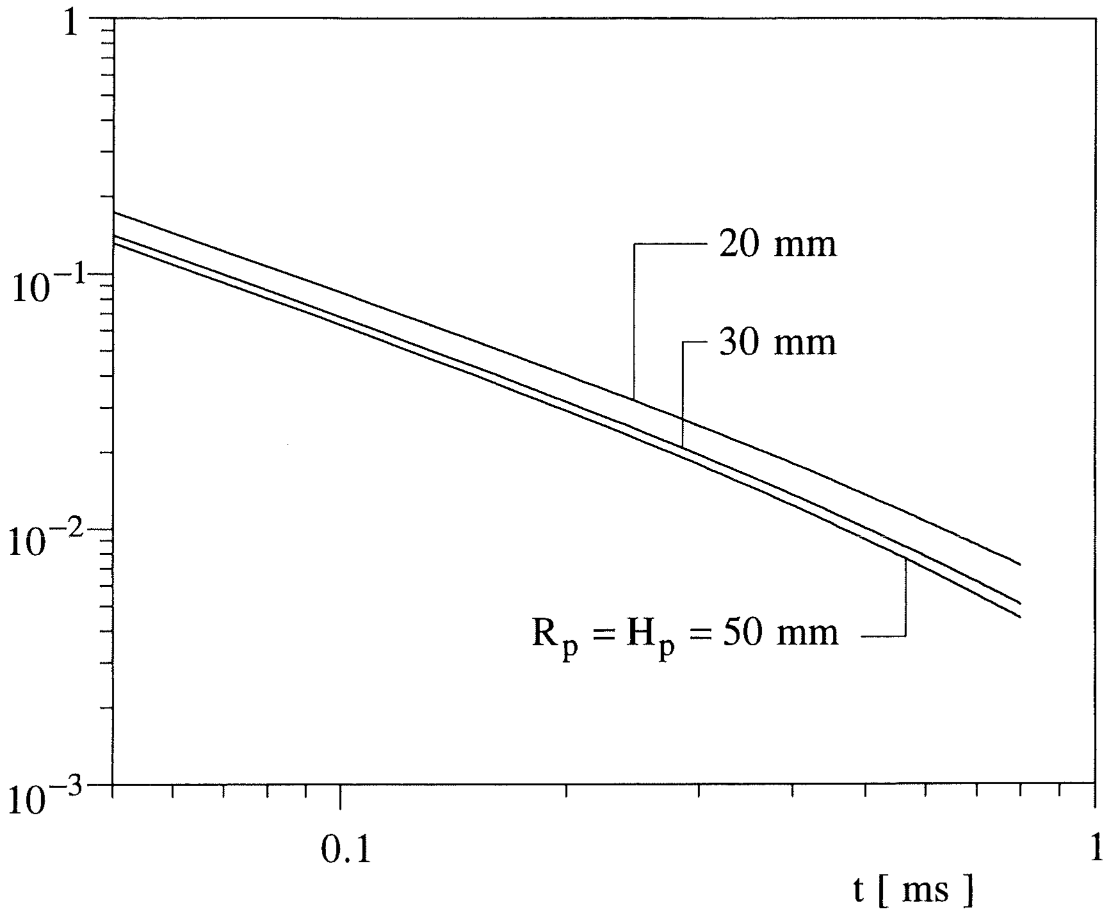

Figure 35. The effect of the size of the water pool on the energy conversion efficiency.

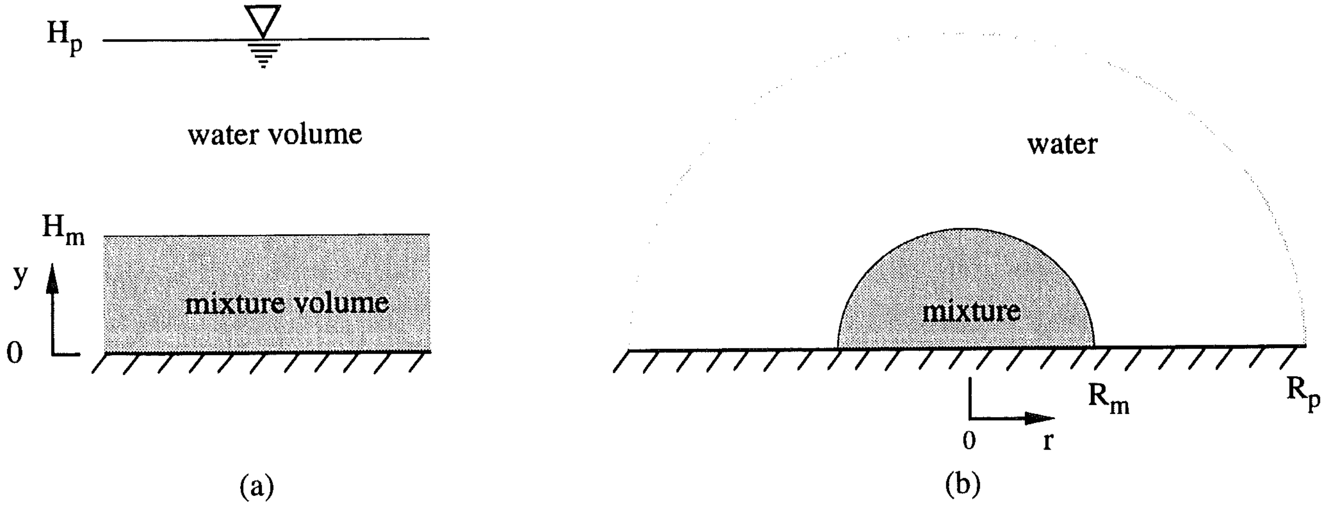

Figure 36. One-directional configurations: (a) vertical expansion, and (b) radial expansion.

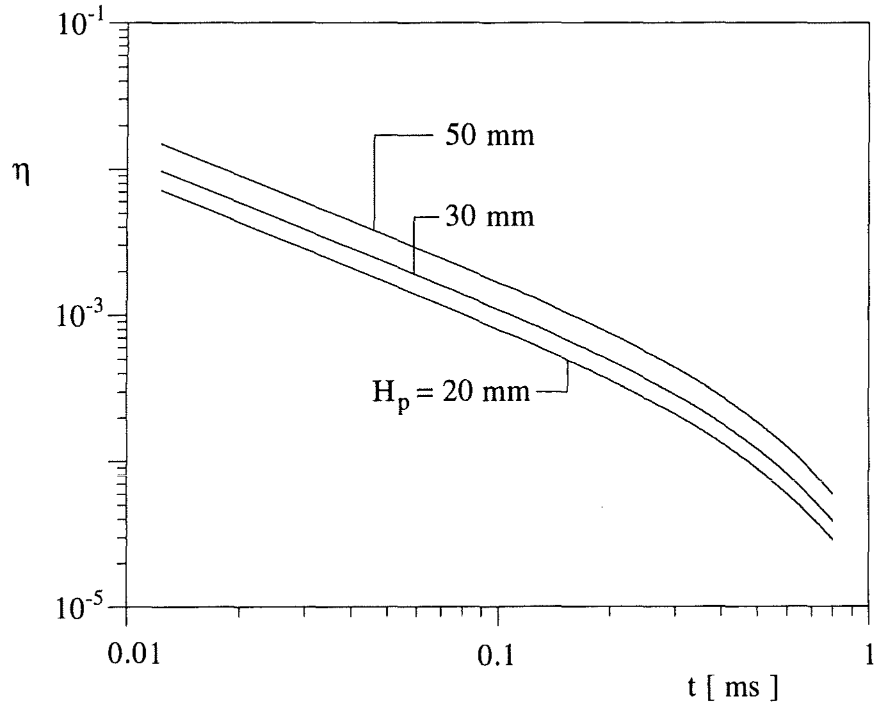

Figure 37. The effect of water pool size on efficiency in the configuration of Fig. 36a.

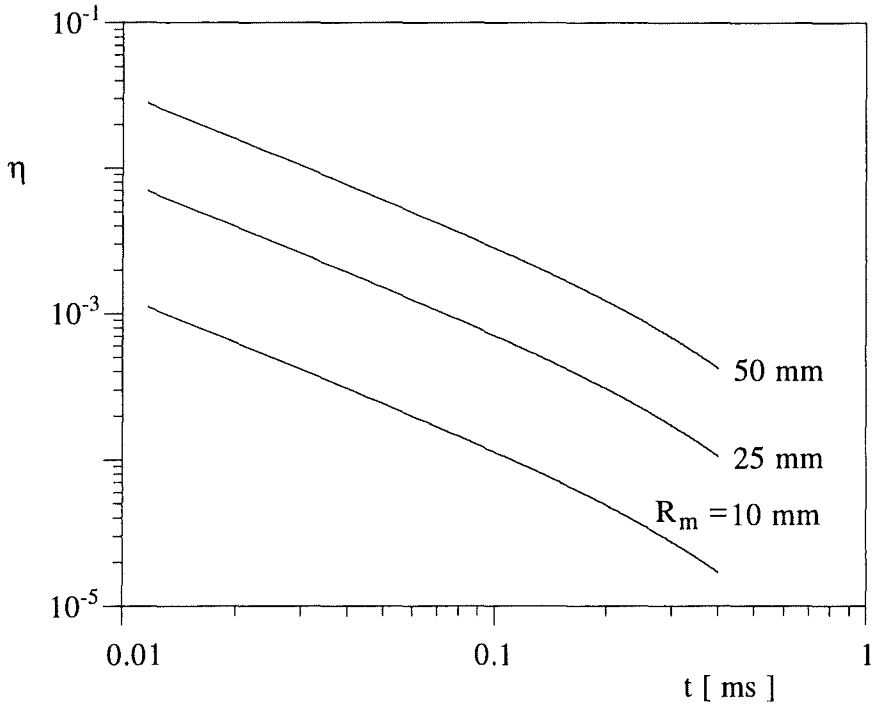

Figure 38. The effect of mixture volume size on efficiency in the configuration of Fig. 36b.

the most important source of thermodynamic irreversibility: the heat transfer from melt to water when the temperature difference between the two is the greatest.

This section represents a departure from the line of inquiry that was followed consistently in Sections 2-4. The new feature is that motion and expansion are ruled out. Another feature is that the calculation leads to a single efficiency value, which depends only on the initial parameters of the melt and water combination. In Sections 3 and 4, the calculations shed light on the early stages in the history of the energy conversion efficiency, which is a function of time as the mixture expands.

5.1 Model

The purpose of the following analysis is to evaluate the energy conversion efficiency (or irreversibility) associated with the mixing of an amount of molten material (m_m) with an amount of saturated liquid water (m_w) in a fixed volume (Fig. 39). The molten material is initially superheated at the temperature T_i. During the mixing process it experiences, (i) sensible cooling down to the solidification point T_m, (ii) solidification at T_m, and (iii) sensible cooling to a final equilibrium temperature, T_e. During the same process, the (P_0) to the final conditions P_e and T_e.

The equilibrium pressure and temperature are dictated by the first law of thermodynamics for the total mass ($m_m + m_w$) as an isolated system,

$$m_m\left(u_{m,i} - u_{m,e}\right) = m_w\left(u_{w,e} - u_{w,i}\right) \tag{106}$$

and the volume constraint for the water mass

$$\rho_{w,i} = \rho_{w,e} \tag{107}$$

In these equations u_m, u_w and ρ_w are the specific internal energies of the two components and the density of water. Equations (105) and (106) are sufficient for determining P_e and T_e. Built into Eq. (107) is the assumption that the volume fraction occupied by m_m does not change. Consequently, we model m_m as an incompressible substance with constant specific heat (c_m) from T_i to T_m, latent heat of solidification u_{sf}, and constant specific heat (c_s) from T_m to T_e. The specific energy change shown on the left side of Eq. (106) becomes

$$u_{m,i} - u_{m,e} = c_m\left(T_i - T_m\right) + u_{sf} + c_s\left(T_m - T_e\right) \tag{106'}$$

where it has been assumed that the solidification has been complete, i.e., $T_e \leq T_m$.

For the water component we expect P_e and T_e to represent a state of high pressure and temperature, most likely in the supercritical pressure domain. For the left side of the liquid-vapor dome, that is, during the process (i) → (e) executed by the water mass m_w, we use the latest compilation of water thermodynamic properties [27]. We proceed at constant density into the compressed liquid states, cf. Eq. (107), namely, $\rho_{w,e} = 958 \text{ kg/m}^3$, and reach states (e) of increasing pressure (P_e) and temperature (T_e), as the specific energy ($u_{w,e}$) at that state increases. This evolution is reported in Figs. 40 and 41, where the curves were fitted to data interpolated from the tables of Haar et al. [27]. In each case the curve starts from the initial state of water, which is saturated liquid at atmospheric pressure ($u_{w,e}$ = 419 kJ / kg). In the ranges indicated in Figs. 40 and 41 the T_e [K] and P_e [bar] values are accurate within 0.5 percent and, respectively, 0.95 percent.

The specific entropy curve (Fig. 42) was obtained similarly, and is accurate within 0.93 percent. How far we travel to the right on the curves of Figs. 40 – 42 depends on the mass ratio m_m / m_w and the initial state of the melt, cf. Eq. (106). We return to this aspect at the end of Section 5.2.

5.2 Efficiency

The system ($m_m + m_w$) is surrounded by saturated liquid water at atmospheric pressure P_0. Accordingly, we regard P_0 and $T_0 = T_{sat}(P_0)$ as environmental state (i.e., restricted dead state [40]) in the following exergy estimates. The energy conversion efficiency of the process (i) → (e) is best represented by the exergetic (second law) efficiency

$$\eta = \frac{\text{exergy at state (e)}}{\text{exergy at state (i)}} \qquad (108)$$

The exergy at state (i) is due only to m_m, because m_w is initially at the environmental state. To estimate the nonflow exergy of the melt $\Xi_{m,i}$ we imagine a reversible work production process in three parts, with heat rejection to T_0:

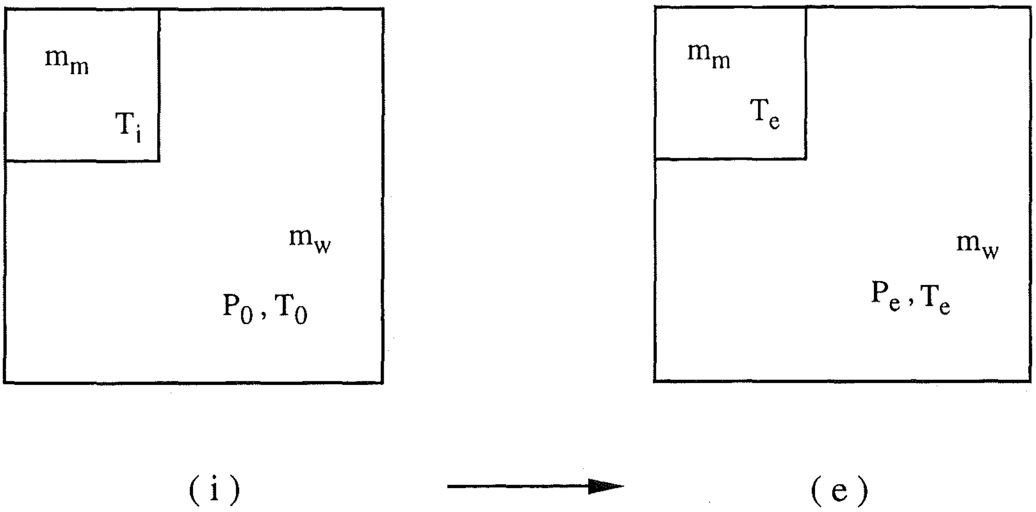

Figure 39. The constant-volume mixing of specified amounts of water (m_w) and molten material (m_m).

1. Sensible cooling from T_i to T_m:

$$W_1 = m_m\, c_m \left(T_i - T_m - T_0 \ln \frac{T_i}{T_m} \right) \tag{109}$$

2. Solidification at T_m:

$$W_2 = m_m\, u_{sf} \left(1 - \frac{T_0}{T_m} \right) \tag{110}$$

3. Sensible cooling from T_m to T_e:

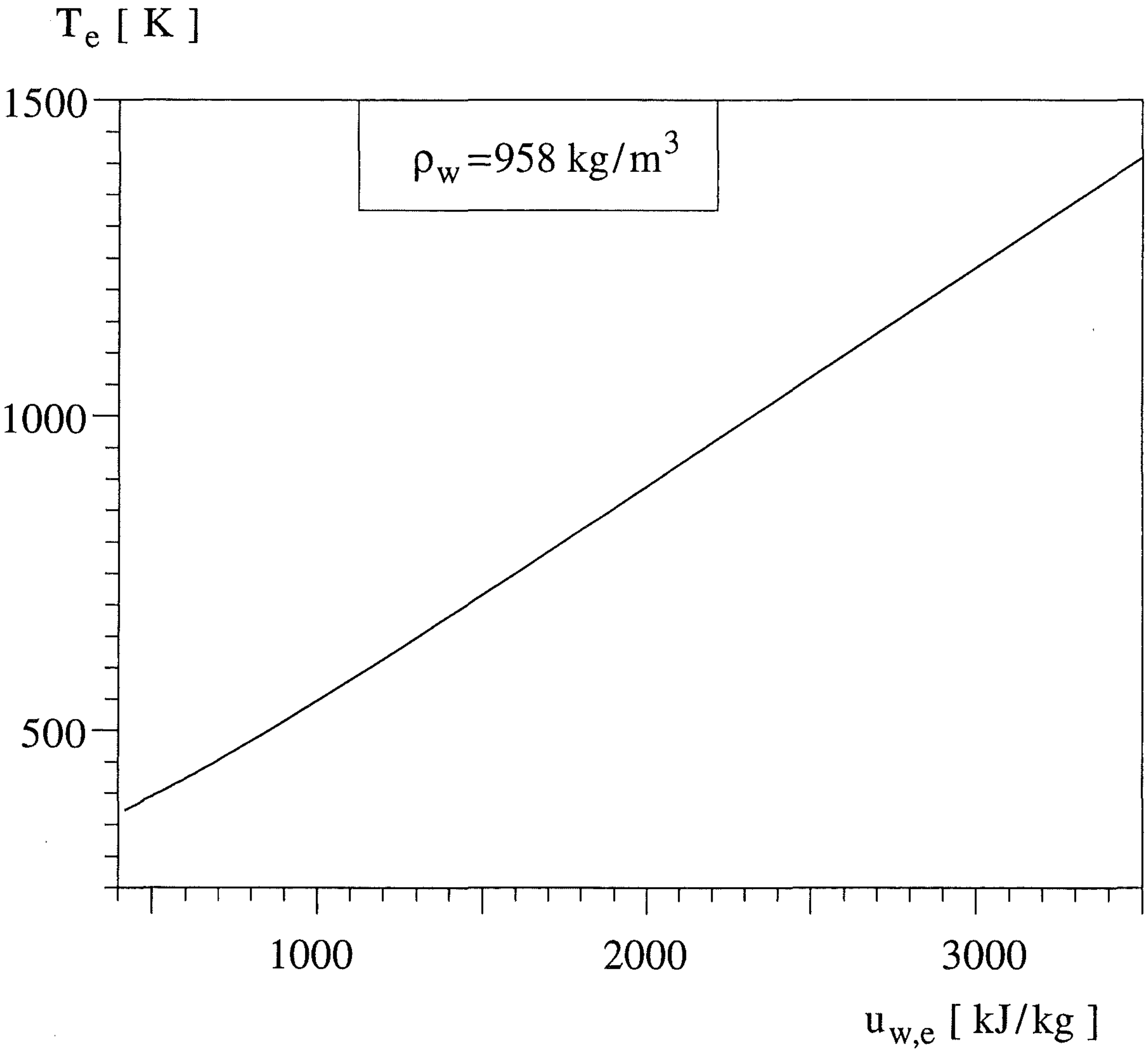

Figure 40. The temperature variation at constant density in compressed liquid water.

$$W_3 = m_m c_s \left(T_m - T_e - T_0 \ln \frac{T_m}{T_e} \right) \quad (111)$$

In sum, the initial exergy of the system is

$$\Xi_{m,i} = W_1 + W_2 + W_3 \quad (112)$$

At the end of the process, in the thermally mixed state (e), the exergy still held by the melt is

$$\Xi_{m,e} = m_m c_s \left(T_e - T_0 - T_0 \ln \frac{T_e}{T_0} \right) \quad (113)$$

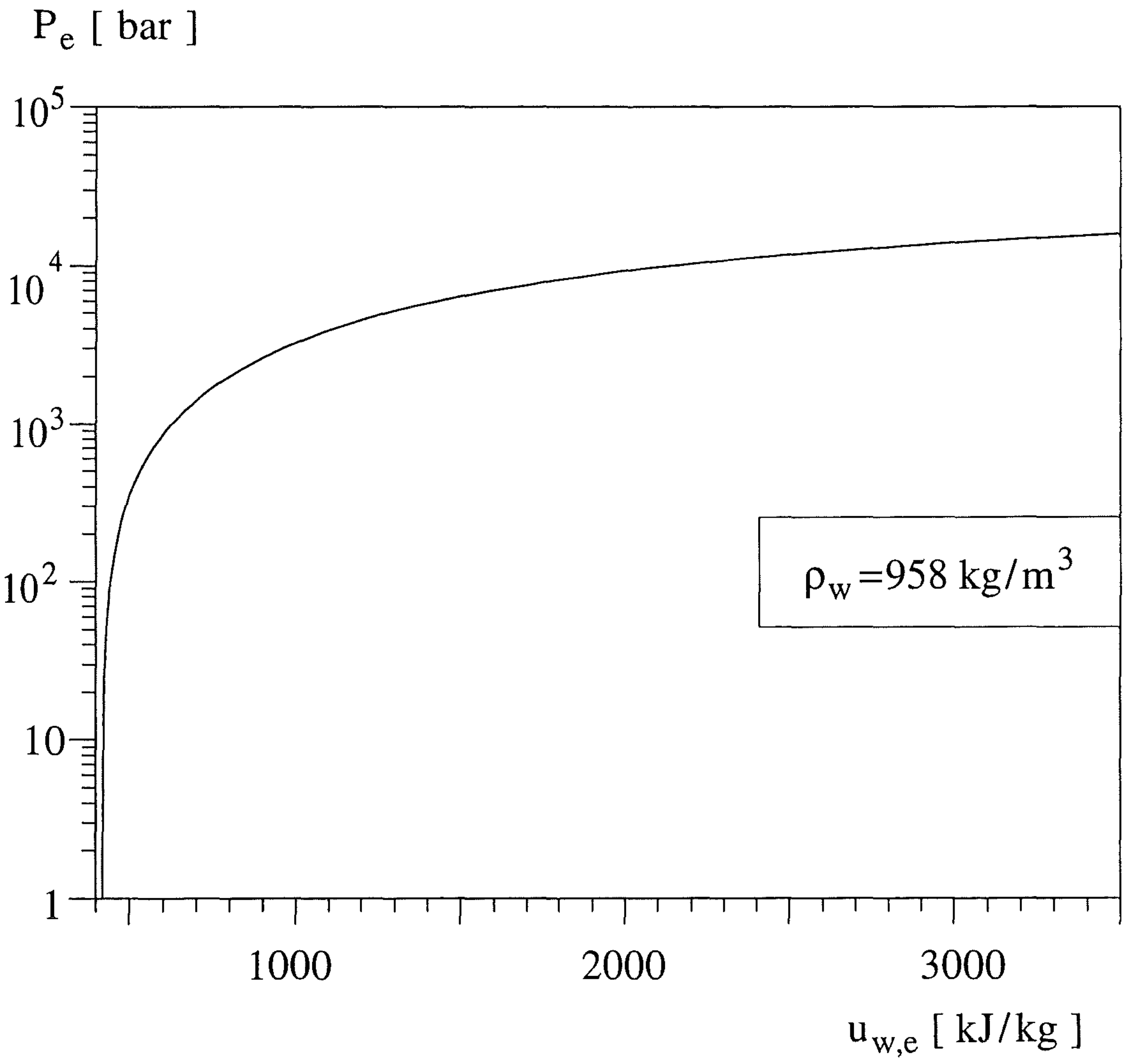

Figure 41. The pressure variation at constant density in compressed liquid water.

where it has been assumed that the solidification is complete ($T_e \leq T_m$). For the water mass at state (e) we use the nonflow exergy [40] with respect to saturated liquid at T_0,

$$\Xi_{w,e} = m_w \xi_w = m_w \left[u_e - u_i - T_0 \left(s_e - s_i \right) + P_0 \left(v_e - v_i \right) \right] \tag{114}$$

The last term in the square brackets is zero because the specific volume (or density) does not change from (i) to (e), cf. Eq. (107). Putting everything together, we conclude that the efficiency is

$$\eta = \frac{\Xi_{m,e} + \Xi_{w,e}}{\Xi_{m,i}} \tag{115}$$

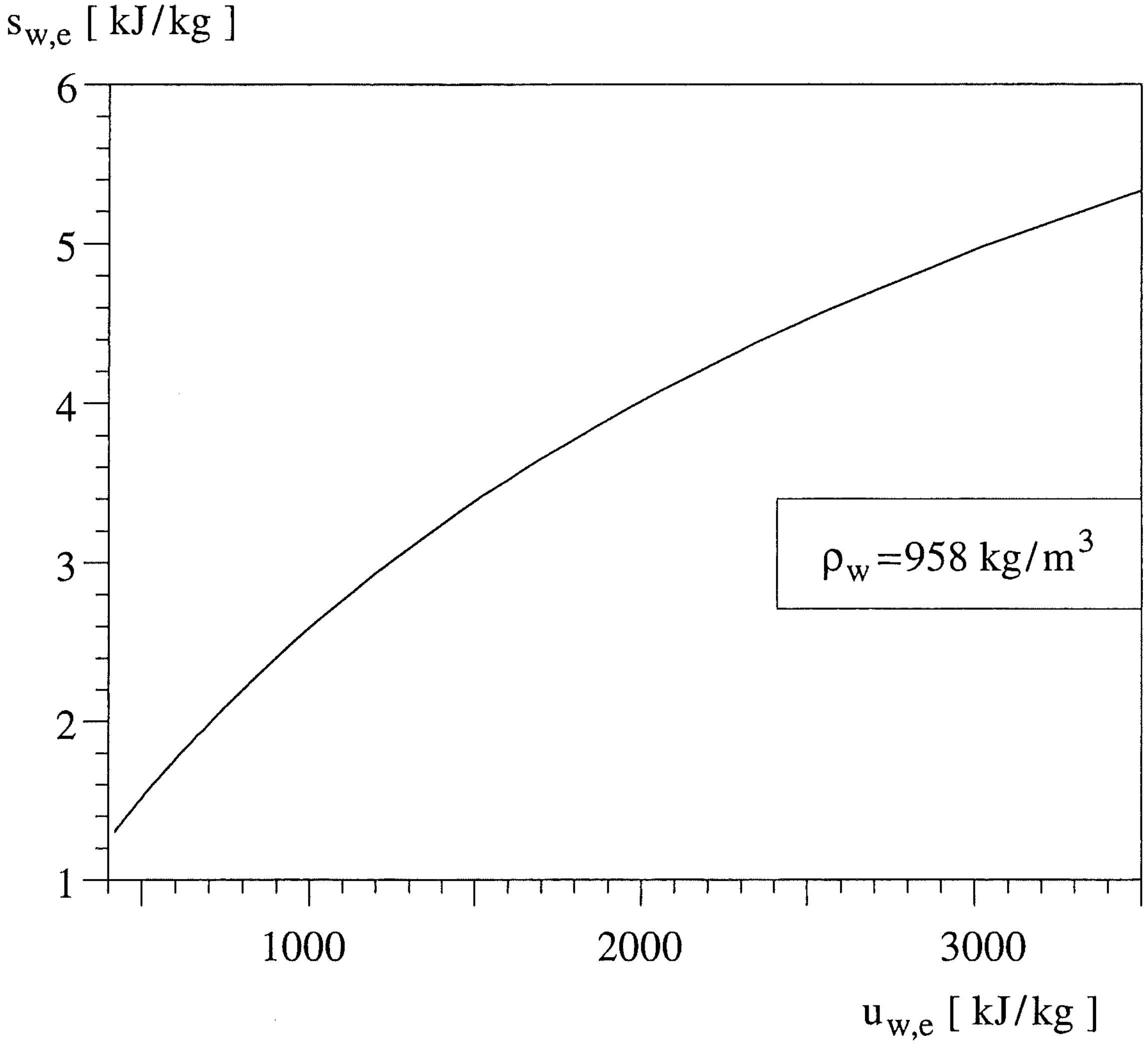

Figure 42. The entropy variation at constant density in compressed liquid water.

The following η calculations are based on the constants

$$\begin{array}{ll} T_0 = 373\ \mathrm{K} & P_0 = 10^5\ \mathrm{N/m^2} \\ T_i = 2600\ \mathrm{K} & T_m = 2313\ \mathrm{K} \\ c_m \cong 1.32\ \mathrm{kJ/kgK} & c_s \cong 1\ \mathrm{kJ/kg\,K} \\ u_{sf} = 1067\ \mathrm{kJ/kg} & c_w = 4.03\ \mathrm{kJ/kg\,K} \end{array} \tag{116}$$

The calculation begins with combining Eqs. (106) and (108) with Fig. 40. The result is the relationship between $u_{w,e}$ and m_m/m_w, which is displayed in Fig. 43. This monotonic relation is used next to convert the $u_{w,e}$ abscissas of Figs. 40 – 42 into abscissas representing the "design" parameter m_m/m_w. In this way all the quantities that appear on the right-hand side of Eq. (115) can be calculated as soon as the mass ratio is specified. The end result of this calculation is the efficiency shown as a solid line in Fig. 44.

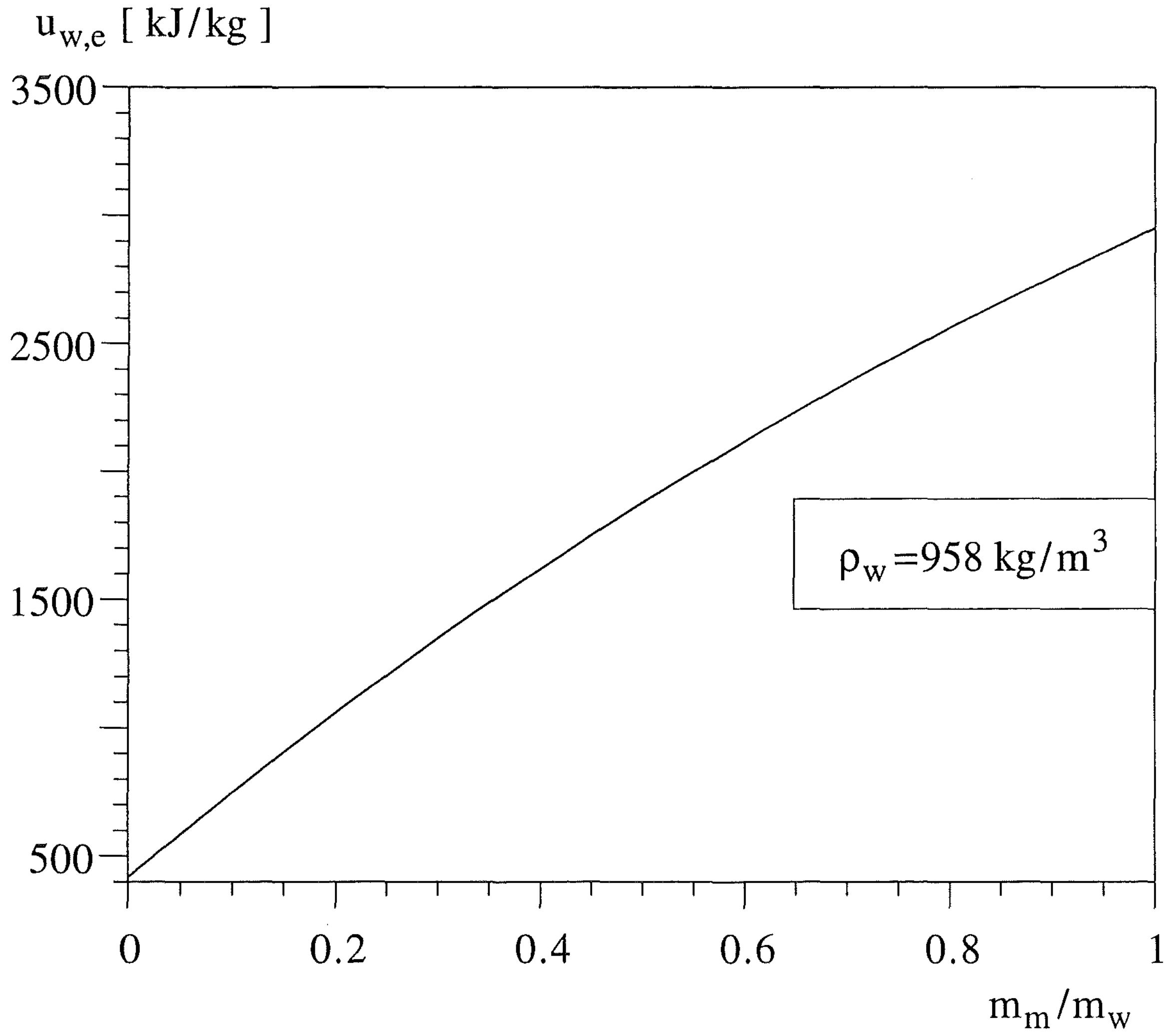

Figure 43. The specific internal energy of liquid water in the final state (e), as a function of the mass ratio.

5.3 The Small Melt Mass Fraction Limit

It is possible to anticipate analytically the behavior of the efficiency η in the limit of small melt mass fraction, $m_m/m_w \rightarrow 0$. In that limit the equilibrium temperature T_e approaches T_0, and most of the energy change experienced by m_m from T_i to T_e ($\sim T_0$) is due to the sensible cooling of the solid [e.g., Eq. (118)]. Over the temperature interval T_i - T_0, we define the equivalent specific heat of m_m as a single-phase substance, $\bar{c}_m$, by setting the sensible-heat change $\bar{c}_m$ (T_i - T_0) equal to the actual energy change:

$$\bar{c}_m\left(T_i - T_0\right) = c_m\left(T_i - T_m\right) + u_{sf} + c_s\left(T_m - T_0\right) \qquad (117)$$

Using the data listed in Eqs. (116) we find, in order,

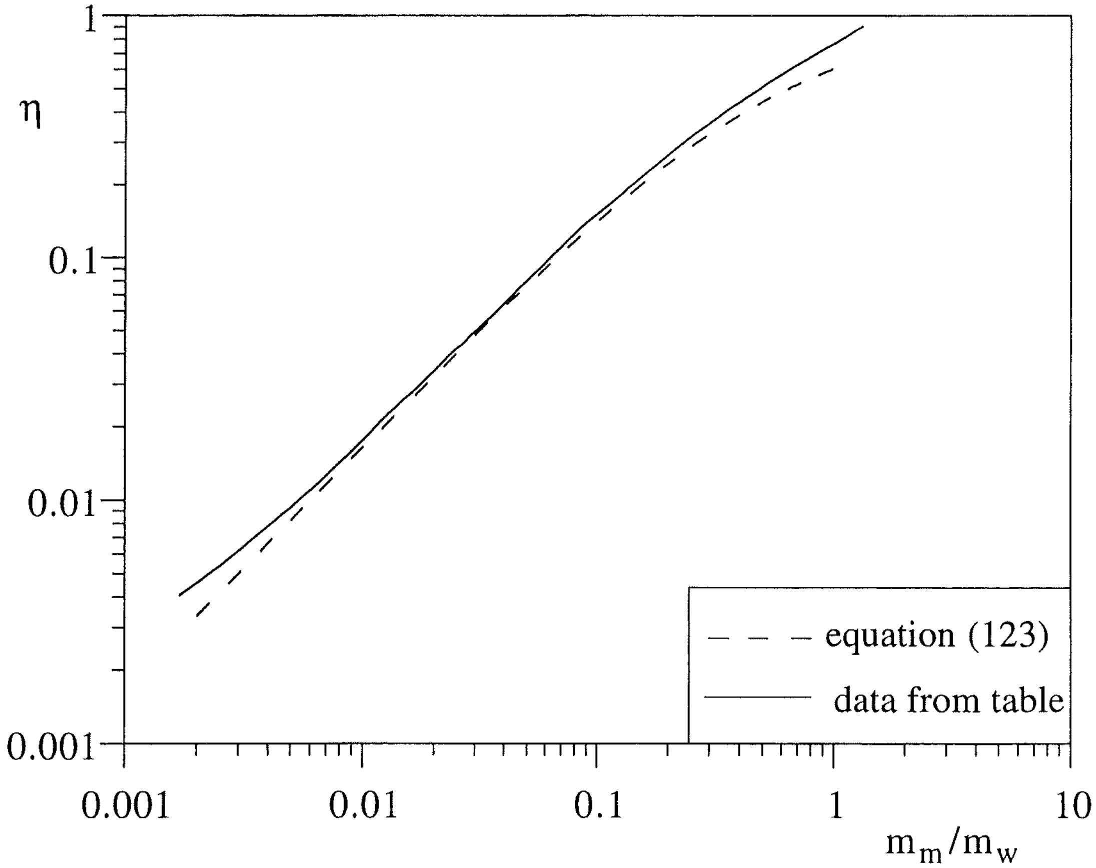

Figure 44. The exergetic efficiency as a function of the mass ratio.

$$\bar{c}_m = (0.170 + 0.479 + 0.871)\ \frac{kJ}{kg} = 1.52\ \frac{kJ}{kg} \tag{118}$$

which shows that the value of $\bar{c}_m$ is indeed dominated by the sensible cooling of m_m as a solid, from T_m to T_0.

In the same limit ($T_e \gtrsim T_0$), we model the water mass m_w as an incompressible substance with the specific heat c_w. Equation (106) attains the explicit form

$$m_m\bar{c}_m\left(T_i - T_e\right) = m_w c_w\left(T_e - T_0\right) \tag{119}$$

Similarly, Eqs. (112) – (114) become

$$\Xi_{m,i} = m_m\bar{c}_m\left(T_i - T_0 - T_0\ \ln\frac{T_i}{T_0}\right) \tag{120}$$

$$\Xi_{m,e} = m_m\bar{c}_m\left(T_e - T_0 - T_0\ \ln\frac{T_e}{T_0}\right) \tag{121}$$

$$\Xi_{w,e} = m_w c_w\left(T_e - T_0 - T_0\ \ln\frac{T_e}{T_0}\right) \tag{122}$$

Substituting Eqs. (119) – (121) into the efficiency definition (115) we find

$$\eta = \left(1 + \frac{1}{\mu}\right)\ \frac{\tau_e - 1 - \ln\ \tau_e}{\tau_i - 1 - \ln\ \tau_i} \tag{123}$$

where

$$\mu = \frac{m_m\bar{c}_m}{m_w c_w} \qquad \tau_i = \frac{T_i}{T_0} \qquad \tau_e = \frac{T_e}{T_0} \tag{124}$$

The first law [Eq. (119)] provides another relation between μ and τ_e,

$$\tau_e = \frac{\mu\ \tau_i + 1}{\mu + 1} \tag{125}$$

such that η is solely a function of μ (or the mass fraction m_m/m_w),

$$\mu = \frac{\bar{c}_m}{c_w}\ \frac{m_m}{m_w} = \frac{1.52}{4.03}\ \frac{m_m}{m_w} = 0.38\ \frac{m_m}{m_w} \tag{126}$$

Solving by trial and error Eqs. (123) and (125) for τ_i = 2600 K / 373 K ~ 7, we complete the following table:

μ	τ_e	η	m_m/m_w
0.1	1.545	0.299	0.265
0.02	1.118	0.081	0.053
0.01	1.059	0.042	0.027

The function $\eta(m_m/m_w)$ described by Eqs. (123) and (125) has been added to Fig. 44. In the limit $\mu \rightarrow 0$ this function behaves as

$$\eta = \frac{1}{2}\mu \frac{(\tau_i - 1)^2}{\tau_i - 1 - \ln \tau_i} = 4.44\mu = 1.68 \frac{m_m}{m_w} \tag{127}$$

This shows that when m_m/m_w is small the exergetic efficiency is of the same order of magnitude as the mass ratio m_m/m_w. In the opposite limit, when the order of m_m/m_w is greater than 1, the efficiency η approaches 1.

5.4 The Effect of the Choice of Dead State

Exergy calculations depend on the choice of dead state [40]. In Sections 5.2 and 5.3 the dead state was taken as the initial pressure and temperature of the water (P_0, T_0), with the thought that the "environment" surrounding the system of Fig. 39 is infinite and made out of liquid water at P_0 and T_0. Another plausible choice of dead state is represented by the atmospheric conditions

$$P_* = 10^5 \text{ N/m}^2 \qquad T_* = 298 \text{ K} \tag{128}$$

In this case the efficiency formula (115) must be modified because the initial exergy of the water mass $\left(\Xi_{w,i}\right)$ is no longer zero. The complete definition is

$$\eta = \frac{\text{exergy at state (e)}}{\text{exergy at state (i)}} = \frac{\Xi_{m,e} + \Xi_{w,e}}{\Xi_{m,i} + \Xi_{w,i}} \tag{129}$$

where

$$\Xi_{w,i} = m_w \left[u_i - u_* - T_* \left(s_i - s_*\right) + P_* \left(v_i - v_*\right)\right] \tag{130}$$

$$\Xi_{w,e} = m_w \left[u_e - u_* - T_* \left(s_e - s_*\right) + P_* \left(v_e - v_*\right)\right] \tag{131}$$

and $\left(u_*, s_*, v_*\right)$ represent water properties evaluated at P_* and T_*. The initial and final exergies of the melt mass are, cf. Eqs. (109)–(113),

$$\Xi_{m,i} = m_m c_m \left(T_i - T_m - T_* \ln \frac{T_i}{T_m} \right) + m_m u_{sf} \left(1 - \frac{T_*}{T_m} \right) \tag{132}$$

$$+ m_m c_s \left(T_m - T_e - T_* \ln \frac{T_m}{T_e} \right)$$

$$\Xi_{m,e} = m_m c_s \left(T_e - T_* - T_* \ln \frac{T_e}{T_*} \right) \tag{133}$$

The solid line in Fig. 45 shows the result of combining Eqs. (129)–(133), and using the P_* and T_* values and the rest of the data listed in Eqs. (116). The dashed line reproduces the efficiency calculated in Sections 5.2 and 5.3 based on $P_0 = 10^5 \text{ N} / \text{m}^2$ and $T_0 = 373$ K. The figure shows that the choice of dead state temperature has only a minor effect, which becomes visible when m_m/m_w is of the order of 10^{-2} or smaller. Relevant is also the observation that the dead state used in Sections 5.2 and 5.3 leads to an efficiency estimate that is higher (i.e., more conservative) than the efficiency calculated in this section.

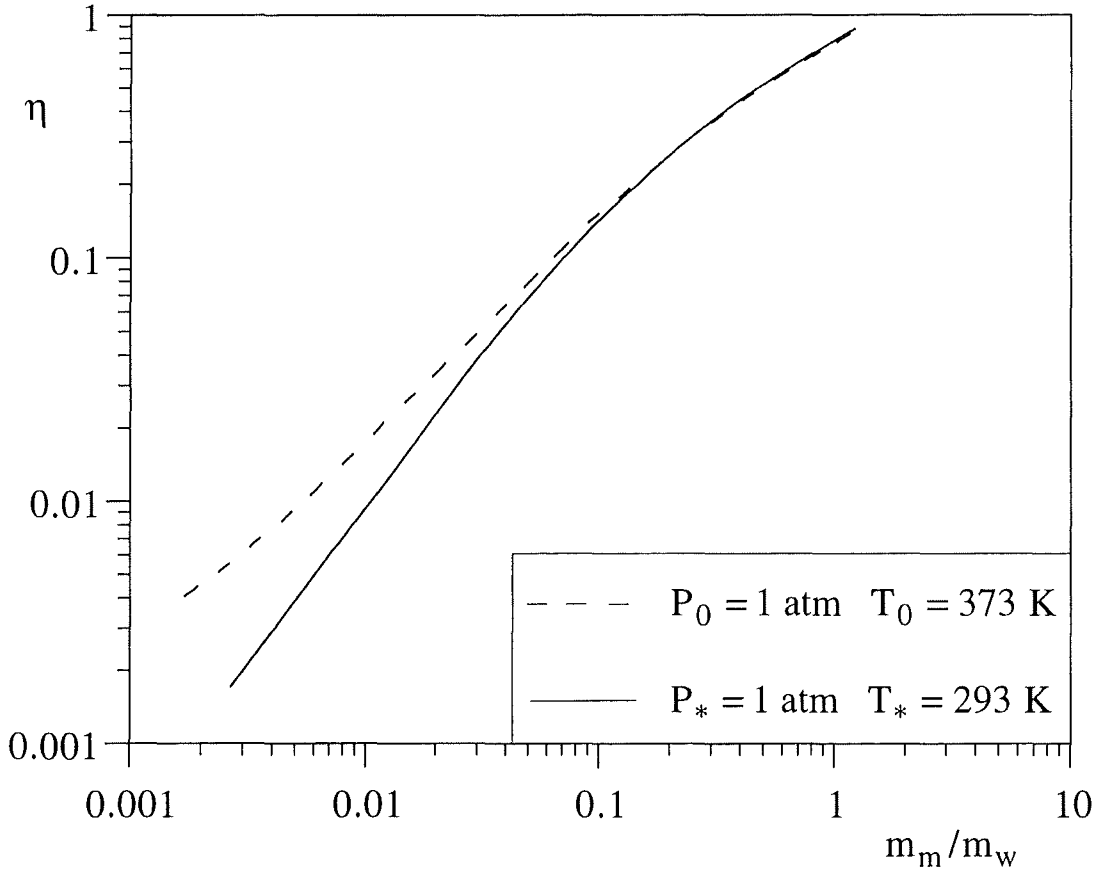

Figure 45. The effect of the choice of dead state temperature on the exergetic efficiency.

We verified the new η result plotted in Fig. 45 by repeating its calculation based on the analytical model outlined in Section 5.3. To start with, the equivalent specific heat of the melt is $\bar{c}_m = 1.50 \text{ kJ/kg}$ instead of 1.52 kJ/kg. This conclusion follows from substituting $T_* = 298$ K in place of T_0 in Eq. (117). Next, Eqs. (131)–(133) are replaced by

$$\Xi_{w,e} = m_w c_w \left(T_e - T_* - T_* \ln \frac{T_e}{T_*} \right) \tag{134}$$

$$\Xi_{m,i} = m_m \bar{c}_m \left(T_i - T_* - T_* \ln \frac{T_i}{T_*} \right) \tag{135}$$

$$\Xi_{m,e} = m_m \bar{c}_m \left(T_e - T_* - T_* \ln \frac{T_e}{T_*} \right) \tag{136}$$

According to Eq. (130) in which $v_i = v_*$, the initial exergy of the water is

$$\Xi_{w,i} = m_w \left[u_i - u_* - T_* \left(s_i - s_* \right) \right] = m_w \tilde{K} \tag{137}$$

where $\tilde{K} = 34.11 \text{ kJ/kg}$. Finally, by substituting Eqs. (134)–(137) into the efficiency definition (129) we obtain

$$\eta = \frac{(1+\mu)\left(\tau_e - 1 - \ln \tau_e\right)}{\mu\left(\tau_i - 1 - \ln \tau_i\right) + \tilde{K} / \left(c_w T_*\right)} \tag{138}$$

where

$$\mu = \frac{m_m \bar{c}_m}{m_w c_w} \qquad \tau_i = \frac{T_i}{T_*} \qquad \tau_e = \frac{T_e}{T_*} \tag{139}$$

The relation between τ_i and τ_e is provided by the first law, which is written as in Eq. (125).

The efficiency η calculated based on Eq. (138) is shown as a dashed line in Fig. 46. The solid line shows the corresponding result developed earlier in this section using the tabulated data for water (see also the solid line in Fig. 45). There is good agreement between the two η calculations—the same level of agreement that we saw earlier in Fig. 44, where the dead state was different. In conclusion, we can use with confidence all the η results presented in Section 5.

5.5 The Effect of Melt Superheat

One question that was raised more than once during this project is whether the model should account for the fact that the melt is at a temperature T_i above the melting point T_m. We are able to answer this question based on the no-flow model used in this section. Figure 47 shows how the efficiency curve responds to the disappearance of melt superheat.

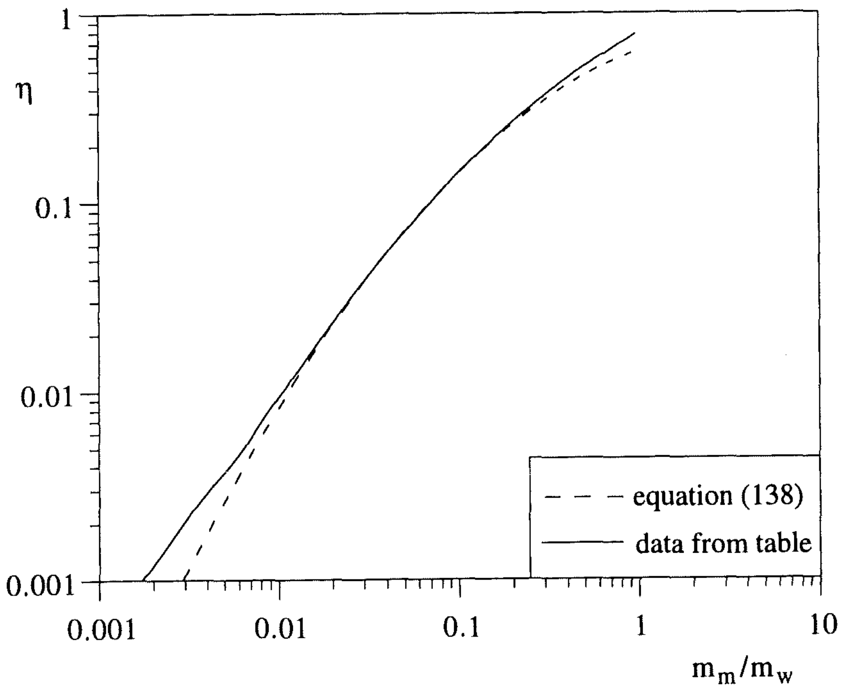

Figure 46. Accuracy test for the efficiency formula (138).

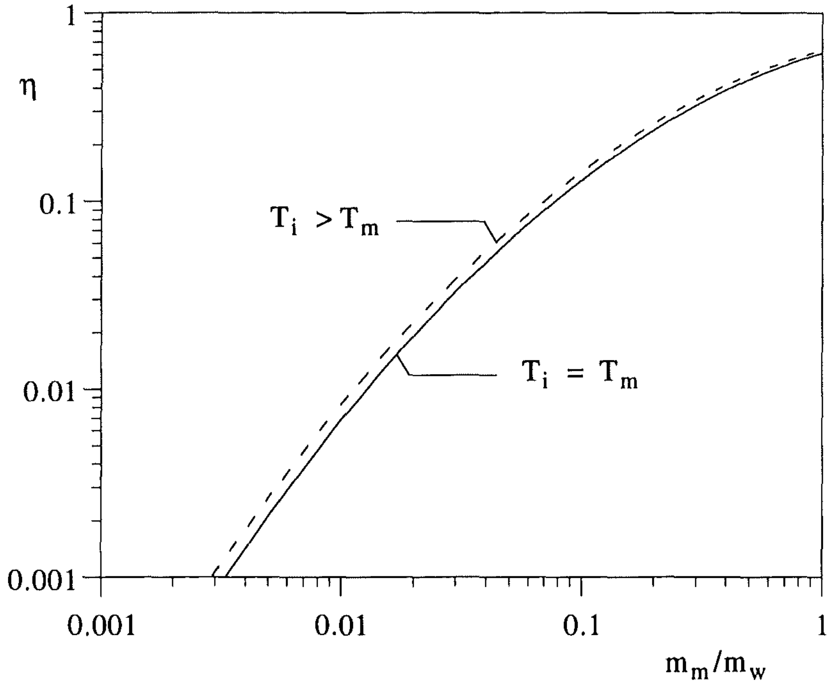

Figure 47. The small effect of the melt superheat ($T_i > T_m$) on the exergetic efficiency.

Both curves were generated with the analytical model and dead state of Section 5.4. The dashed curve corresponds to superheated melt ($T_i = 2600$ K), while the solid curve results from assuming that the melt is saturated liquid ($T_i = T_m = 2313$ K). The figure shows that the change in the η value is relatively small throughout the m_m / m_w range considered in Section 5.

6 EFFICIENCY OF MELT-WATER INTERACTION WHEN THE MIXTURE EXPANDS WITH FLOW RESISTANCE

6.1 Model

In this section we introduce in the model the effect that was ruled out in the preceding section: the flow of the expanding mixture, and the resistance encountered by this flow. Consider a vessel containing a mixture of an amount of molten material (m_m) and an amount of water (m_w). Initially the molten material is heated at the temperature T_i, and the temperature of the water before mixing is T_0. In time, the temperature of the molten material decreases because of heat transfer to water. During the same process, the water temperature T_w and the pressure P increase.

During the expansion process the mixture is ejected through openings in the vessel structure. We model these openings as a number of exit ports as shown in Fig. 48a. Inside the vessel (BL), the instantaneous thermodynamic state is spatially uniform. Each infinitesimal volume element contains molten material and water in the same proportion as the total volume (Fig. 48b).

In every volume element the cooling of the molten material (Δm_m) is balanced by the heating of the water mass (Δm_w). If we neglect the kinetic energy of water and molten material inside the vessel, the first law of thermodynamics for the elemental volume is

$$\Delta m_m \bar{c}_m \left(- \frac{dT_m}{dt} \right) = \Delta m_w c_v \frac{dT_w}{dt} = h \, \Delta A \left(T_m - T_w \right) \qquad (140)$$

where $\bar{c}_m$ is the equivalent specific heat of m_m as a single-phase material. The $\bar{c}_m$ value was defined and calculated in Eq. (118). Assuming the water behaves as an ideal gas, we have

$$P(t) = \rho_w R T_w \qquad (141)$$

where P and ρ_w are the water pressure and the water density respectively. Using Eq. (141), the vessel volume constraint can be written as

$$1 = m_w'''(t)\left[\frac{m_m/m_w}{\rho_m} + \frac{RT_w(t)}{P(t)}\right] \tag{142}$$

where we have assumed a spatially uniform distribution of the components of the mixture. The instantaneous volumetric distribution of water mass is

$$m_w''' = \frac{m_w}{BL} \tag{143}$$

where B is the vessel base and L is its length, Fig. 48a. Mass conservation requires

$$\frac{dm_w'''}{dt} = -m_w'''\frac{\sigma}{L}V \tag{144}$$

In this equation V is the mean velocity of the ejected material, and σ (<< 1) is the area reduction ratio, i.e., cross-sectional area of all the outlet ports divided by the vessel base area. The mixture flow is driven by the pressure drop

$$P(t) - P_0 = \frac{K}{2}m_w'''\left(1 + \frac{m_m}{m_w}\right)V^2 \tag{145}$$

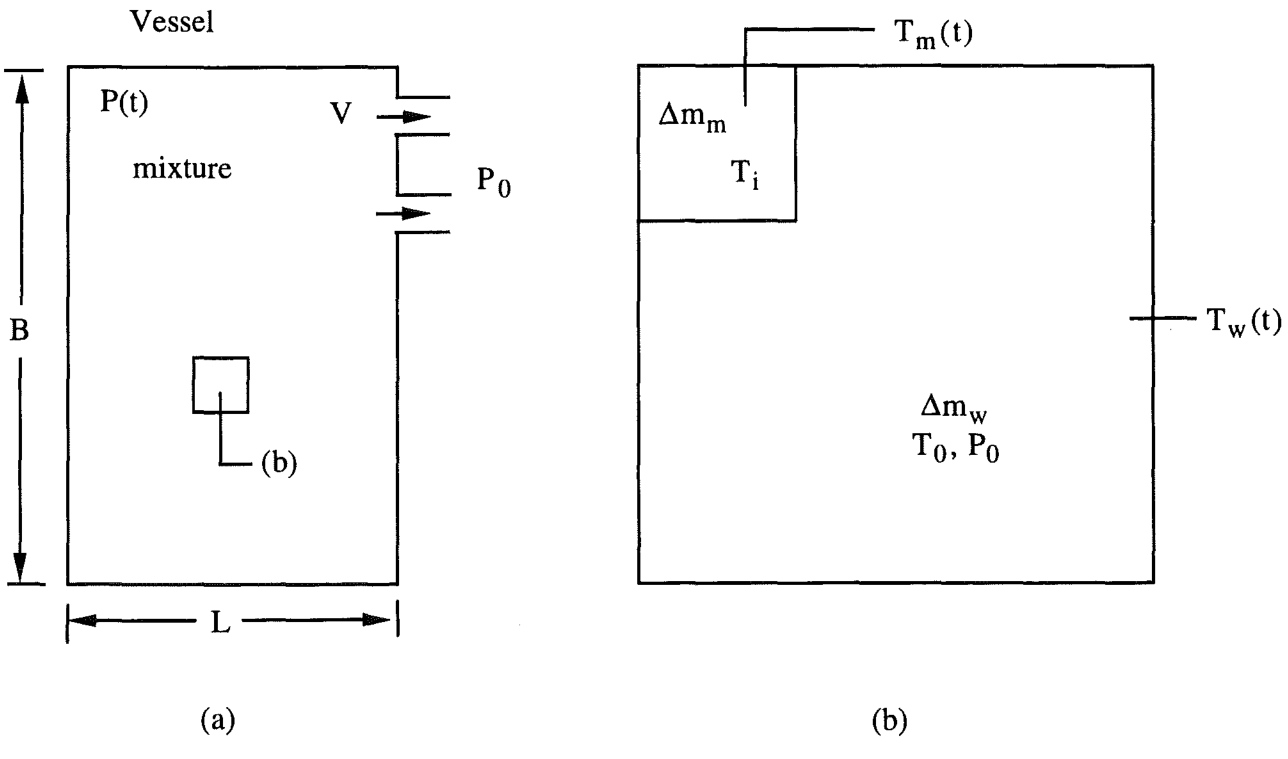

Figure 48. Model of expanding melt-water mixture with flow resistance at the outlet.

where K represents the pressure loss coefficient.

In summary, the analytical model consists of four equations [namely Eqs. (140), (142), (144) and (145)], which must be solved for four unknowns T_w, m_w''', P and V as functions of time.

6.2 Solution

The water temperature $T_w(t)$ is obtained explicitly from Eq. (140)

$$\frac{dT_w}{dt} = \frac{h\Delta A}{c_m \Delta m_m}(1+\mu)\left[\frac{T_0 + \mu T_i}{1+\mu} - T_w\right] \tag{146}$$

where the ratio $\mu = \Delta m_m \bar{c}_m / \Delta m_w c_w$ is constant. Solving Eq. (146) subject to the initial condition $T_w = T_0$ at $t = 0$ yields

$$\theta(\tau) = 1 + a\left[1 - \exp(-\tau)\right] \tag{147}$$

where

$$\theta = \frac{T_w}{T_0} \qquad \tau = \frac{t\, h\, \Delta A\,(1+\mu)}{c_m\, \Delta m_m} \qquad a = \frac{\mu}{1+\mu}\left(\frac{T_i}{T_0} - 1\right) \tag{148}$$

Equation (142) can be arranged in the form

$$1 = M(\tau)\left[b + \frac{\theta}{\tilde{p}}\right] \tag{149}$$

where

$$b = \frac{m_m / m_w}{\rho_m} \cdot \frac{P_0}{RT_0}, \qquad M = m_w''' \frac{RT_0}{P_0}, \qquad \tilde{p} = \frac{P}{P_0} \tag{150}$$

The dimensionless form of Eq. (144) is

$$\frac{dM}{d\tau} = -M \cdot \tilde{V} \tag{151}$$

where

$$\tilde{V} = V \cdot \frac{\sigma}{L} \cdot \frac{c_m \, \Delta m_m}{h \, \Delta A \, (1+\mu)} \tag{152}$$

The equation that remains—Eq. (145)—can be written as

$$\tilde{p}\,(\tau) = 1 + c\, M\, \tilde{V}^2 \tag{153}$$

where the constant c is given by

$$c = \frac{k}{2\,R\,T_0}\left(1 + \frac{m_m}{m_w}\right)\left(\frac{L}{\sigma}\,\frac{h\,\Delta A\,(1+\mu)}{c_m\,\Delta m_m}\right)^2 \tag{154}$$

To summarize, Eqs. (147), (149) and (153) can be solved for θ, $\tilde{p}$ and $\tilde{V}$ as functions of time. The following results are based on integrating Eq. (151) in time by using Runge-Kutta method.

6.3 Efficiency

The chief objective of this study is to calculate the energy conversion efficiency

$$\eta = \frac{\text{kinetic energy of mixture through the exits}}{\text{initial exergy of the system}} = \frac{KE}{\Xi_i} \tag{155}$$

where Ξ_i is the initial exergy of the melt and water system. The kinetic energy (KE) generated by the expanding mixture is a function of time, and is calculated as follows. The instantaneous mass flow rate through all the outlet ports is $\dot{m}_{out} = \rho\, V\, \sigma\, B$. The instantaneous rate at which kinetic energy is imparted to the outflowing stream is $\dot{m}_{out}\,\frac{1}{2}\,V^2$. Integrating this quantity from the time t = 0 until the time t we obtain the total kinetic energy produced by the system:

$$KE = \int_0^t \frac{1}{2}\rho\, \sigma\, B\, V^3\, dt \tag{156}$$

The initial exergy Ξ_i is due to m_m alone, because the water is initially at the environmental state. For the molten material we use the single-phase equivalent model, Eq. (120),

$$\Xi_i = m_m \bar{c}_m \left(T_i - T_0 - T_0 \ln \frac{T_i}{T_0} \right) \qquad (157)$$

The calculated equivalent specific heat $\bar{c}_m = 1.52\ \mathrm{kJ/kg}$ corresponds to the properties listed in Eqs. (116): The efficiency definition (155) can also be written as

$$\eta = \frac{\left(1 + m_w/m_m\right) KE_l}{\bar{c}_m \left(T_i - T_0 - T_0 \ln T_i/T_0\right)} \qquad (158)$$

where KE_l is the kinetic energy per unit mass of mixture:

$$KE_l = \frac{\sigma}{2L} \int_0^t V^3\, dt \qquad (159)$$

The integral (159) was evaluated using the trapezoidal rule.

6.4 Results

The numerical results illustrate the influence of the physical parameters on efficiency. Emphasis is placed on the effects of the particle radius r_m, the mass ratio m_m/m_w, and the area contraction ratio σ. The radius r_m is proportional to $\Delta m_m/\Delta A$:

$$r_m = \frac{3\, \Delta m_m}{\rho_m\, \Delta A} \qquad (160)$$

Figure 49 shows the evolution of the velocity of the ejected mixture. The velocity reaches a peak at a time that is shorter when r_m is smaller. The corresponding kinetic energy production is shown in Fig. 50. The KE_l value increases in time, and is higher when r_m is smaller. The efficiency η has the same time behavior as KE_l, which can also be anticipated from Eq. (158).

The results of Figs. 49-51 were generated by holding the following parameters fixed: $m_m/m_w = 0.2$, $\sigma = 0.01$ and $L = 1\mathrm{m}$. The effect of varying the mass ratio m_m/m_w is illustrated in Figs. 52–56. The velocity, kinetic energy and efficiency decrease correspondingly as m_m / m_w decreases. The water temperature approaches its final value during the time interval associated with the velocity peak (Fig. 54). The pressure reaches a peak at the same time scale, as shown in Fig. 55. Generally, pressures are lower when the relative amount of hot material (m_m / m_w) is smaller.

The effect of changing the area reduction ratio is documented in Figs. 57-60. The velocity reaches a maximum value at a time that is smaller when σ is greater. The maximum velocity is higher for the smaller σ values as shown in Fig. 57. The kinetic energy per unit mass, KE_1, has a sharp slope in time when the area reduction is greater (Fig. 58). The maximum KE_1 values are higher for smaller σ values and the time corresponding to this maximum is higher when σ is smaller. The pressure levels are higher when σ is smaller, and the process slows down as shown in Fig. 59. The pressure peak occurs later in time when σ decreases. As mentioned earlier the efficiency η has the same behaviour as KE_1 and its variation is represented in Fig. 60.

The size of the system (L) has an important effect which is documented in Figs. 61-64. The velocity, kinetic energy and pressure increase when L is higher. Their maximum values occur later in time if the system size is larger. The changing of area reduction σ and system size (L) do not affect the water temperature variation. This feature is visible in Eqs. (147)-(148).

7 CONCLUSIONS

In this project we considered the thermodynamic aspects of the energy conversion process during the sudden thermal interaction between melt particles that are initially dispersed through a body of water. This work and its presentation have been evolutionary: they began with the simplest model of what occurs at the surface-water interface at the start of time (section 2), and continued with more complex models that recommended themselves in light of the conclusions that emerged based on the simpler models (sections 3-6). For detailed conclusions, the reader is directed to the end of each section and, in particular, to sections 2.5, 3.4 and 4.6. In this closing section we review the main points covered in each section, and focus in greater detail on the message delivered by the entire study and, especially, sections 5 and 6.

In section 2 we showed that the immediate thermal contact between water and a very hot surface leads to high supercritical pressures at the interface. The pressure decays to subcritical levels during a time of order 10^{-6} s, when steam forms at the interface. Beyond this stage, the interaction is characterized by heat transfer across a growing and expanding layer of steam. This new feature—the steam—was incorporated in the dispersed mixture model of section 3, in which each hot particle was modeled as a sphere surrounded by a steam annulus and immersed in saturated liquid water. The mixture was one-dimensional, i.e., it expanded in one direction, away from a plane wall (Fig. 12). Through the numerical implementation of the model we wee able to document the effects of the most important physical parameters (e.g., particle size, melt mass fraction, mixture volume size) on overall mixture quantities such as maximum velocity and pressure, and energy conversion efficiency. For the physical parameters that were considered numerically, the efficiency fell

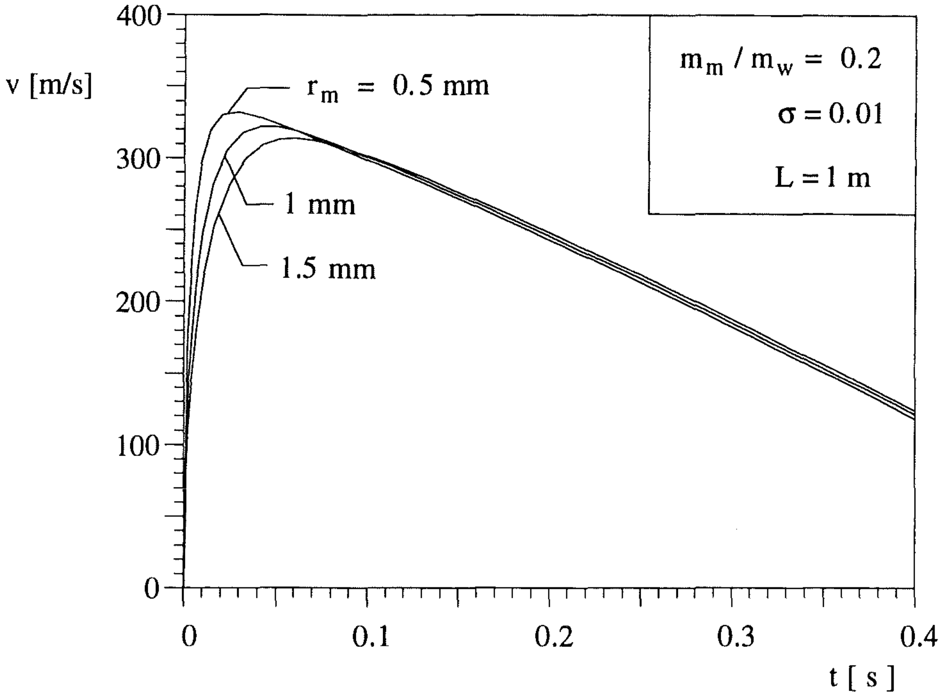

Figure 49. The ejection velocity as a function of time and hot particle size.

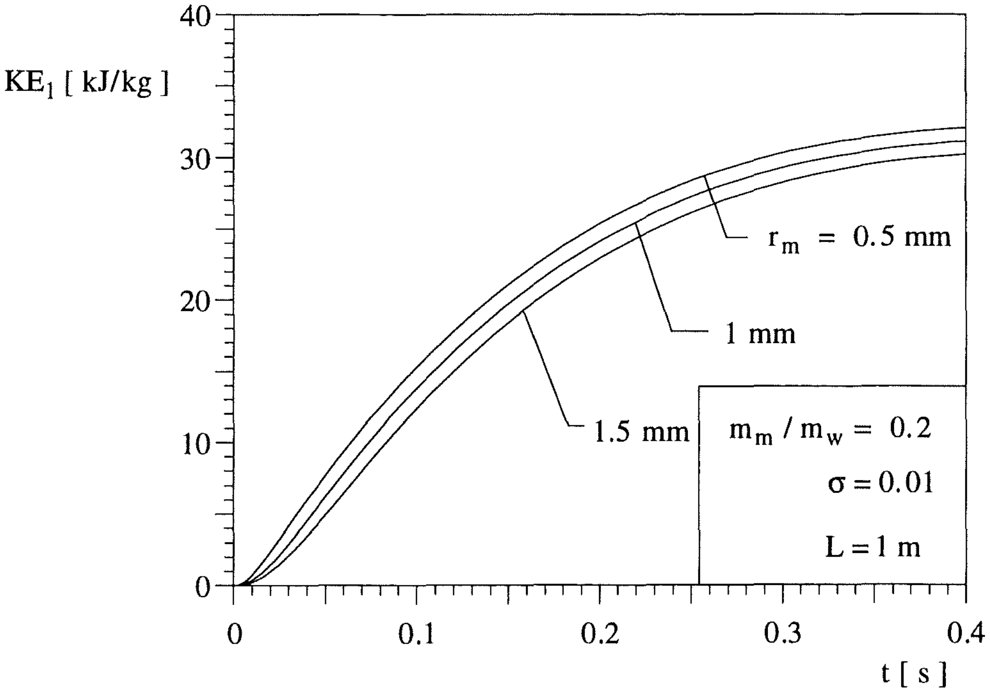

Figure 50. The specific kinetic energy as a function of time and hot particle size.

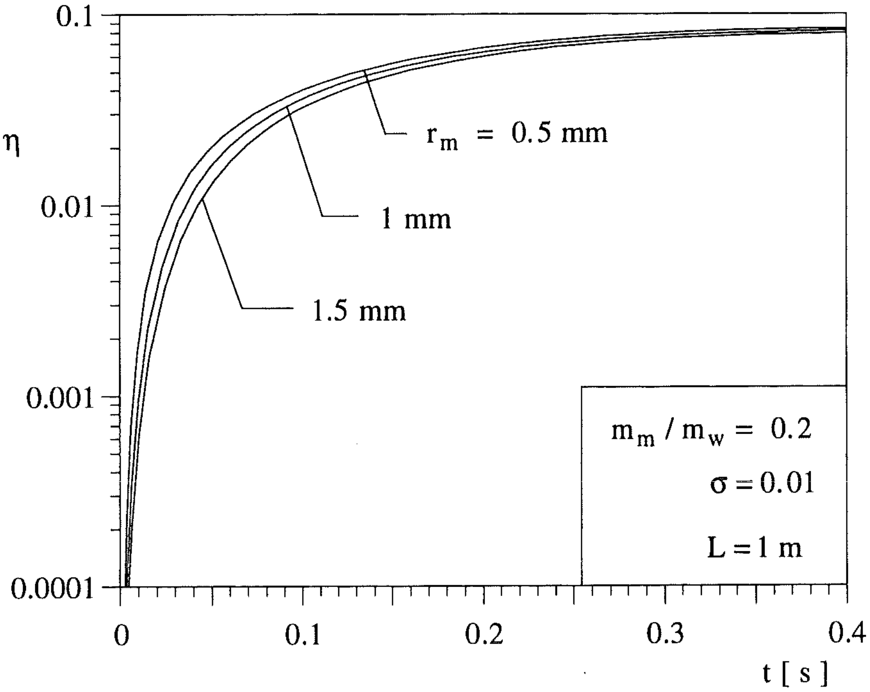

Figure 51. The energy conversion efficiency as a function of time and hot particle size.

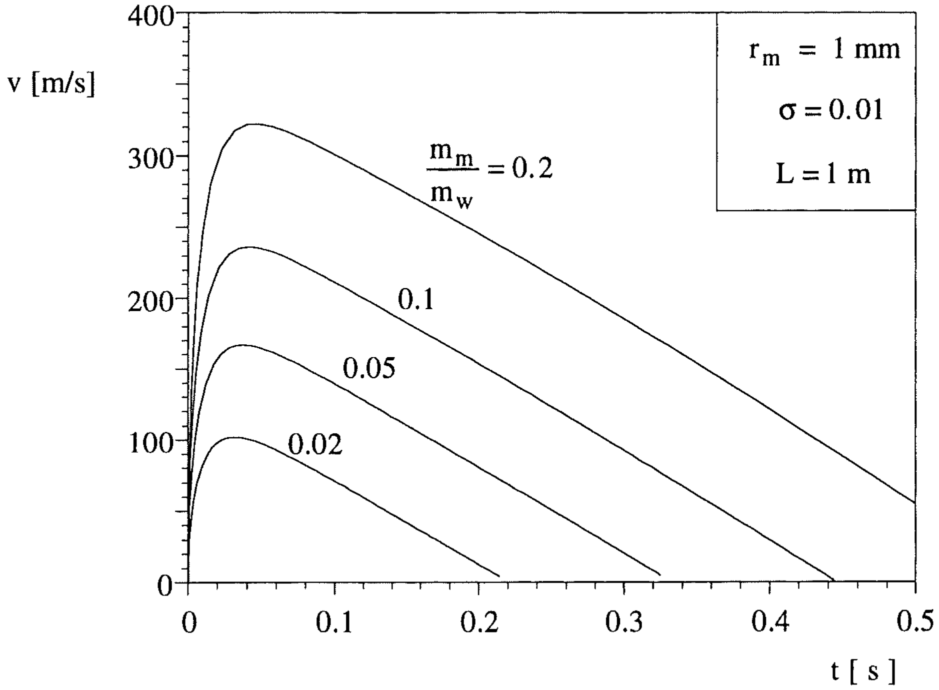

Figure 52. The effect of the mass fraction on the ejection velocity.

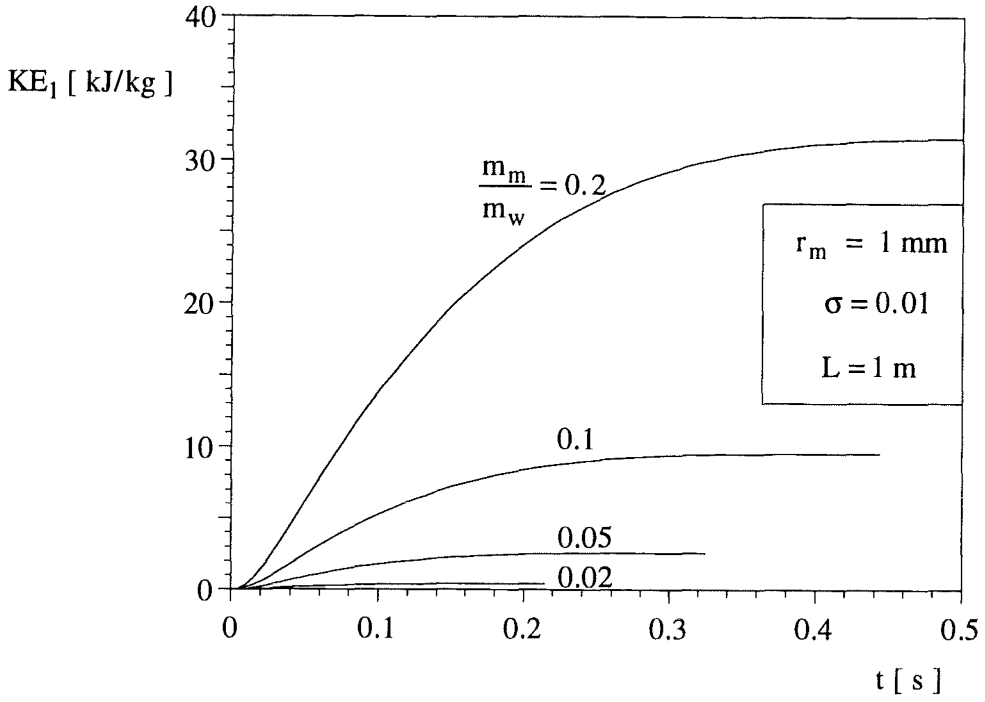

Figure 53. The effect of the mass fraction on the specific kinetic energy.

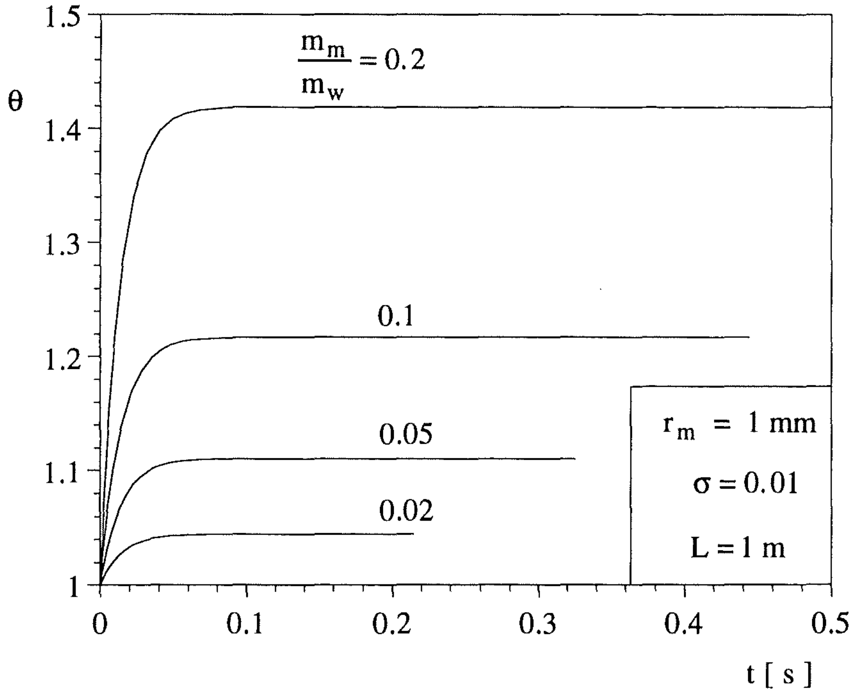

Figure 54. The effect of the mass fraction on the mixture temperature.

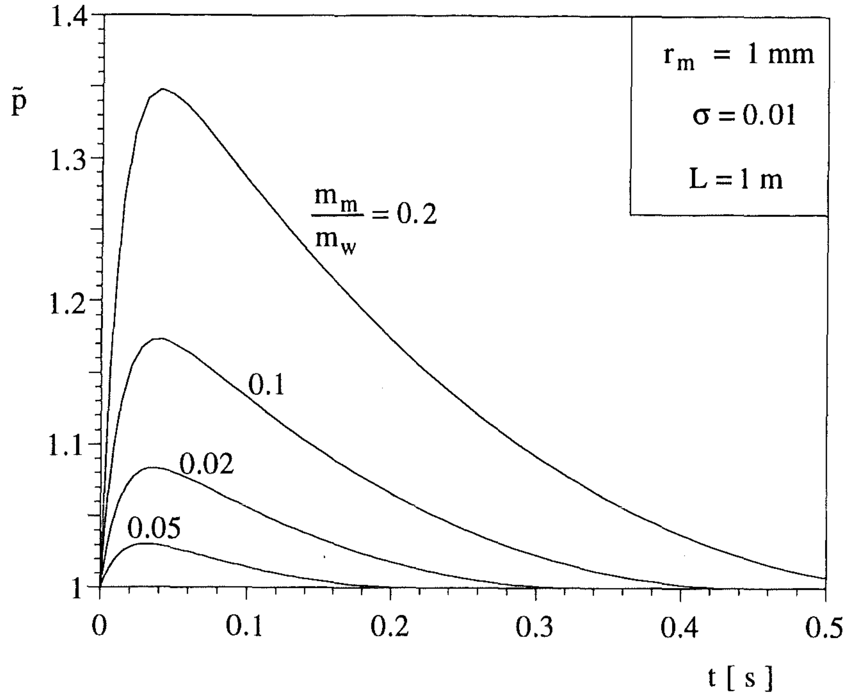

Figure 55. The effect of the mass fraction on the mixture pressure.

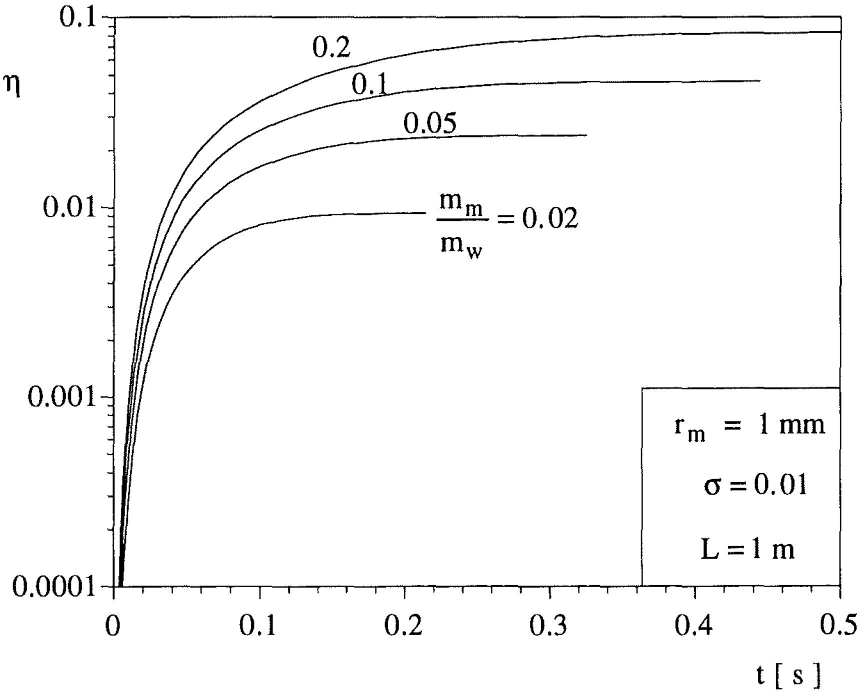

Figure 56. The effect of the mass fraction on the energy conversion efficiency.

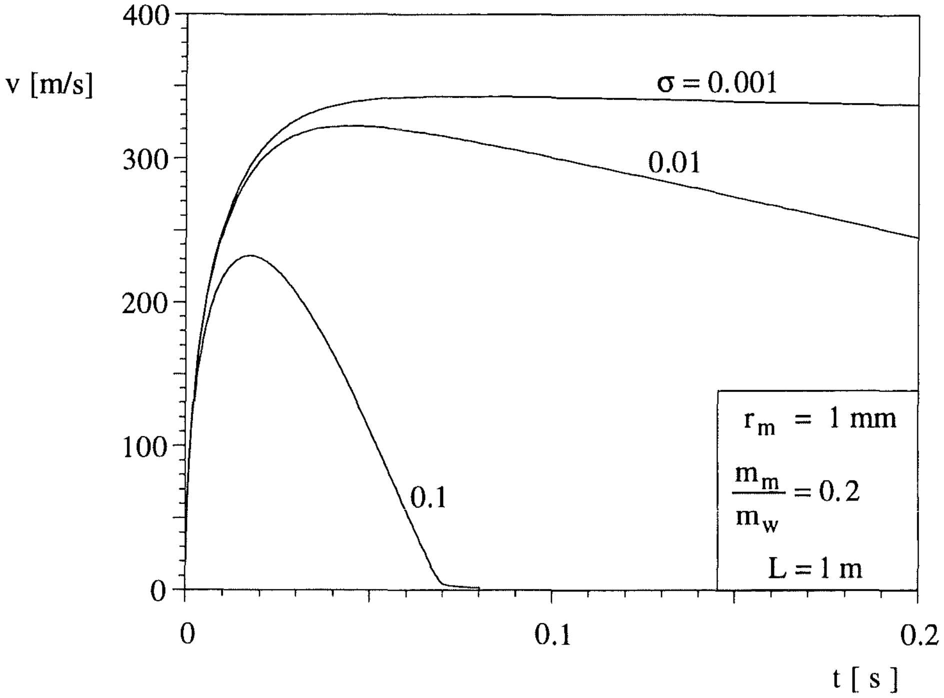

Figure 57. The effect of the area reduction ratio on the ejection velocity.

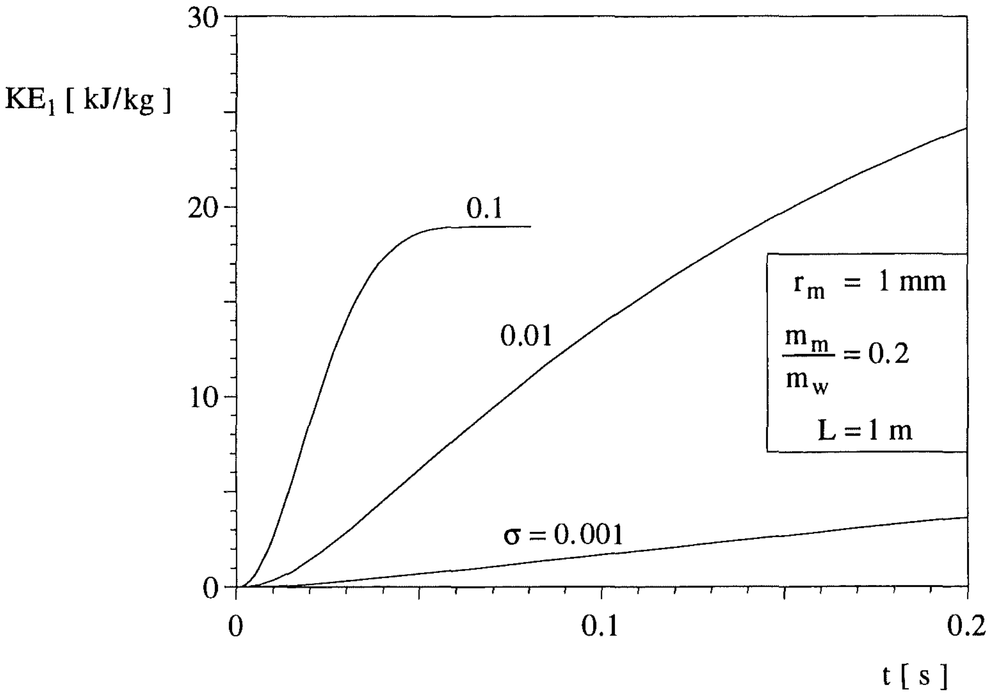

Figure 58. The effect of the area reduction ratio on the specific kinetic energy.

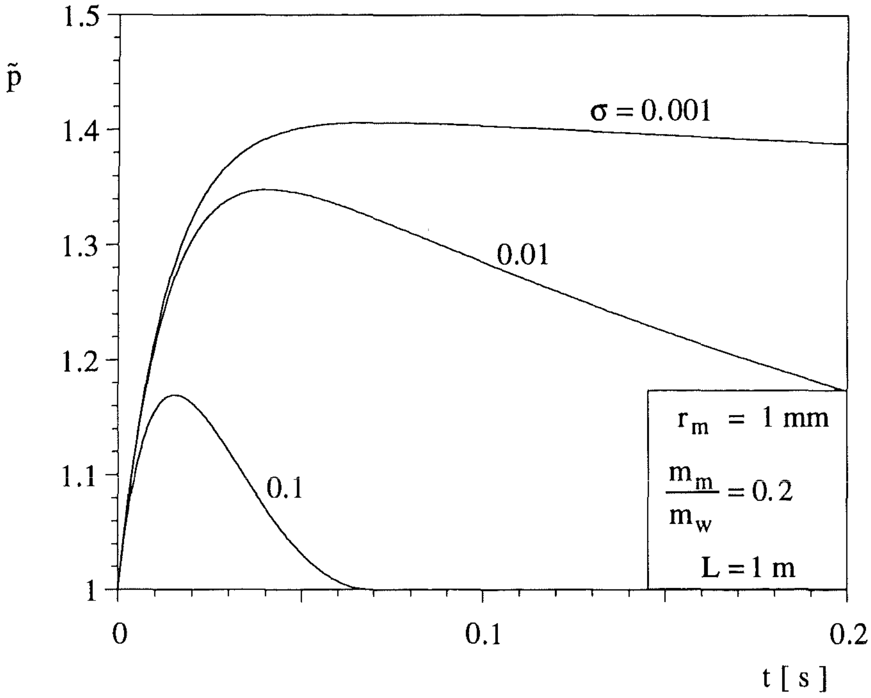

Figure 59. The effect of the area reduction ratio on the mixture pressure.

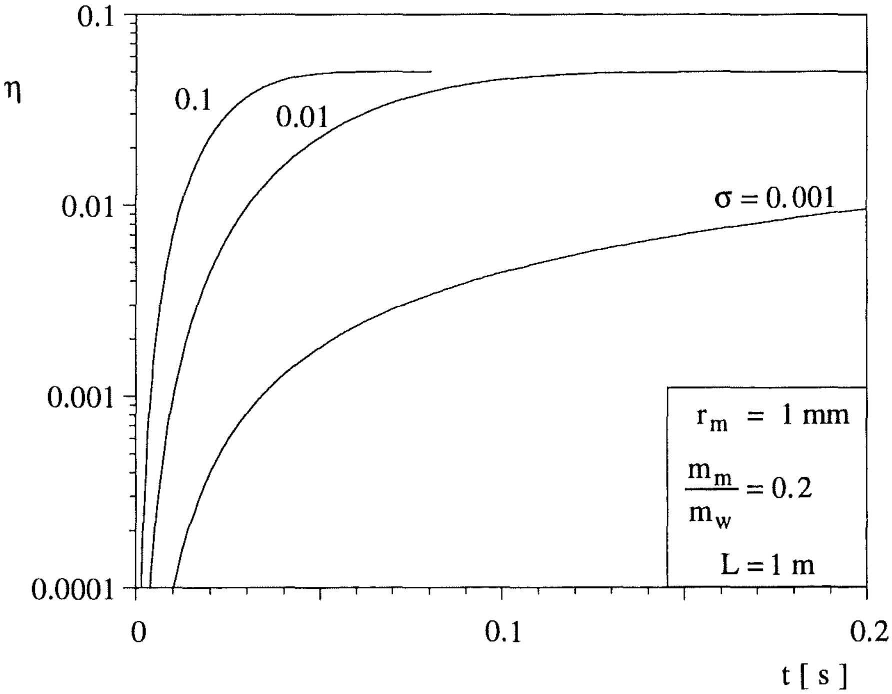

Figure 60. The effect of the area reduction ratio on the energy conversion efficiency.

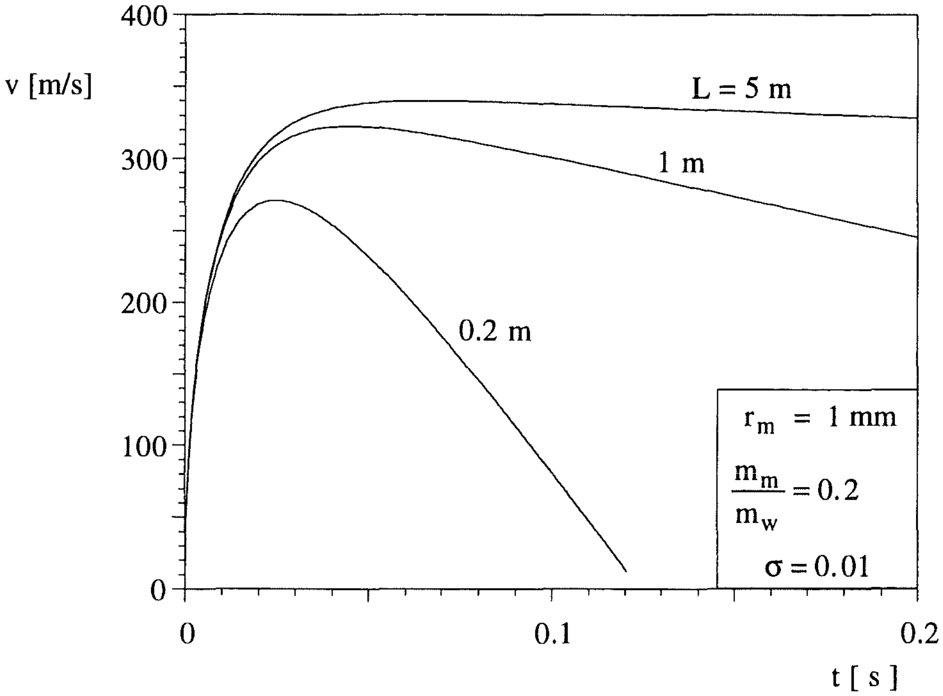

Figure 61. The effect of the system size on the ejection velocity.

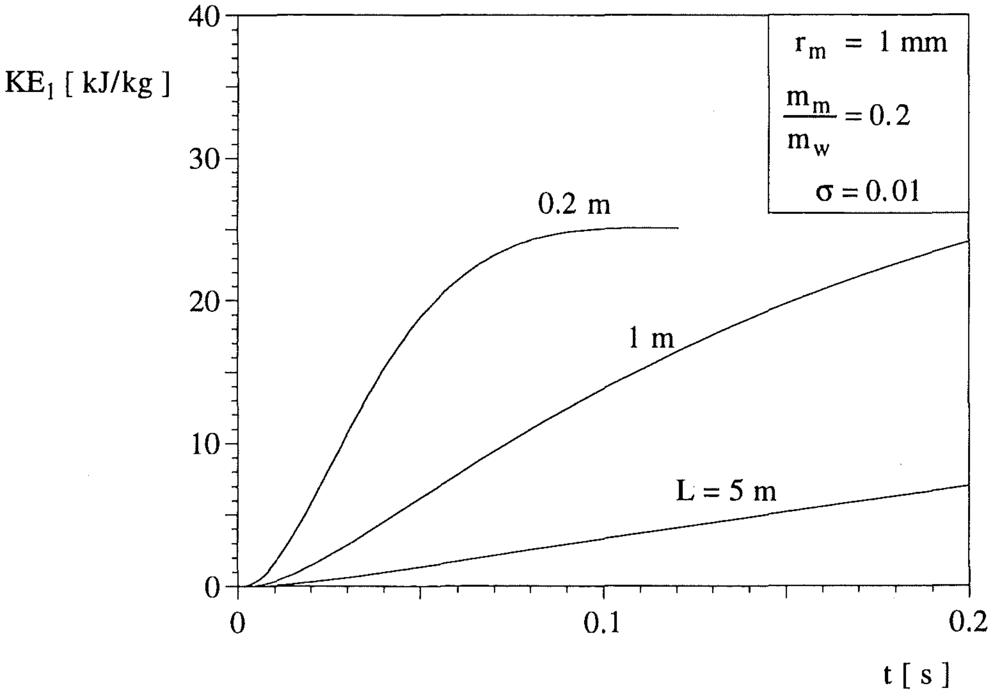

Figure 62. The effect of the system size on the specific kinetic energy.

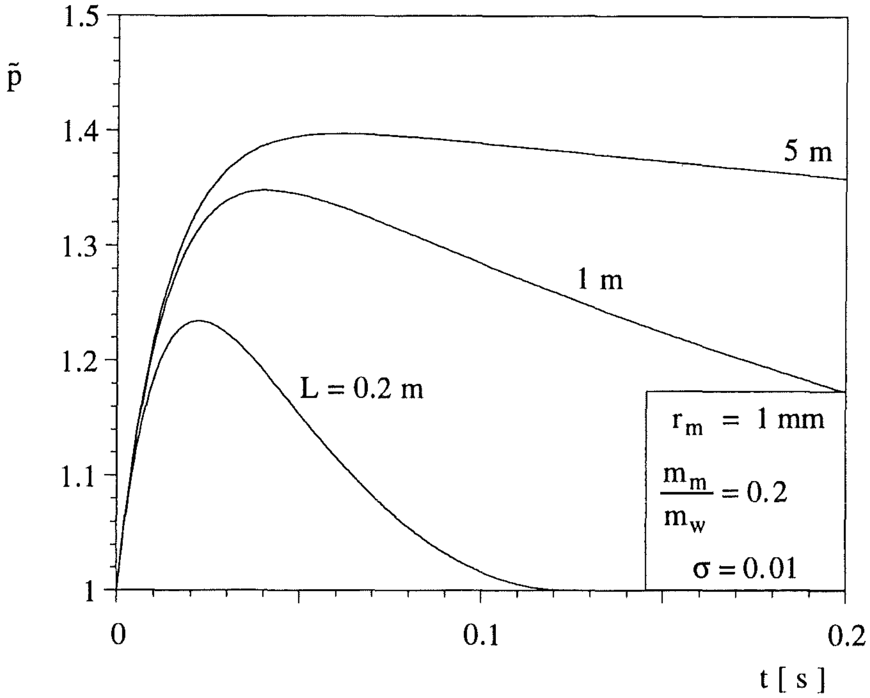

Figure 63. The effect of the system size on the mixture pressure.

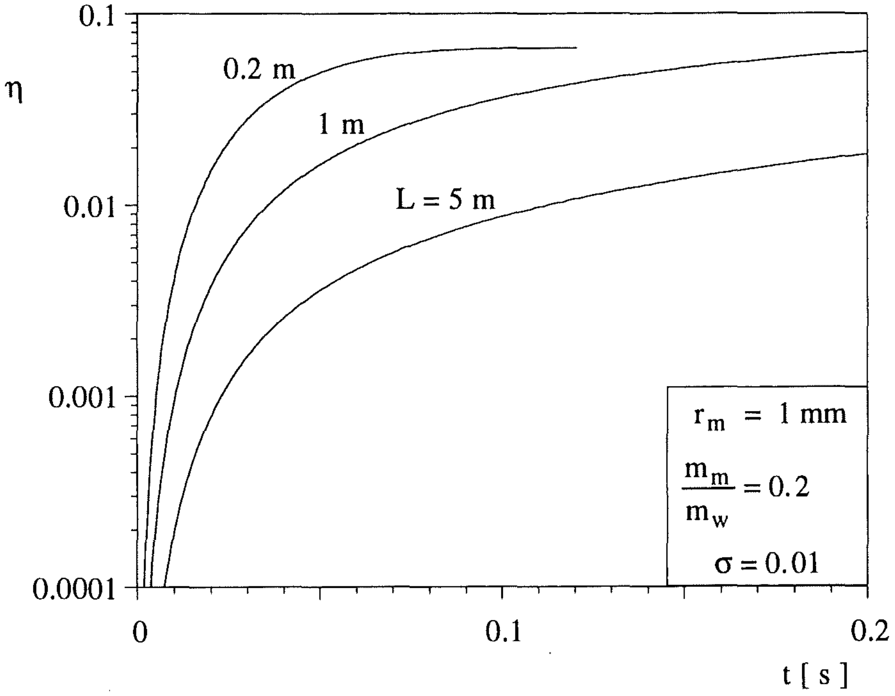

Figure 64. The effect of the system size on the energy conversion efficiency.

in the range $10^{-1} - 10^{-3}$. The efficiency was defined as the ratio of the total kinetic energy acquired by the mixture mass, divided by the total heat transferred from melt to water.

A more realistic model of the dispersed mixture model was implemented in section 4. The melt-steam-water mixture could expand in a space with cylindrical or spherical symmetry. The water volume was not occupied entirely by dispersed melt particles. In other words, the dispersed mixture was restricted to a small portion of the water pool, and expanded against the remaining amount of pure water. The numerical results, and the effect exhibited by physical parameters such as the melt particle size, strengthen the conclusions reached based on the unidrectional model of section 3.

In section 5 we departed from this line of inquiry, and focused purely on the effect of heat transfer irreversibility, which is by far the primary reason why the energy conversion efficiency is so much smaller than 1. We isolated the heat transfer irreversibility by assuming that the thermal interaction occurs without motion of fluid. We performed this portion of the study by using exergy analysis, in fact, this is the first time that exergy analysis was applied to the problem of energy conversion processes with regard to nuclear reactor safety. In section 6 we brought fluid motion (fluid-flow irreversibility) back into the model, by accounting for the escape of the expanding mixture through cracks in the confining vessel (Fig. 48).

The exergy analysis of the melt-water thermal interaction makes two contributions to the current view [4,41] on the ceiling value for the efficiency of energy conversion. First, exergy analysis leads to relatively simple (and, in some cases, analytical) estimates of the exergetic efficiency *without* requiring any assumption regarding the subsequent process in which the melt-water mixture expands. Because of their inherent irreversibility, all subsequent processes are bound to decrease the efficiency below the levels reported in Figs. 44-47.

The second contribution of exergy analysis is that it reveals the important role that is played by the mass ratio m_m/m_w. This local parameter deserves to be monitored closely in future experiments. As shown in Figs. 44-47, when the order of magnitude of the mass ratio is less than 1, the efficiency is of the same order as the mass ratio. This is an extremely important result, because the melt-water interaction leads to steam explosions only if the melt is mixed volumetrically with large amounts of water, which are required for rapid steam generation. In other words, steam explosions are associated with the $m_m/m_w << 1$ limit, and this means that the corresponding efficiency is orders of magnitude smaller than 1. For example, in the experiments documented in ref. [42] the ratio of the total melt and water masses at the start of the experiment was between 1 and 2 percent. The melt/ water mass ratio in the actual interaction zone is highly time dependent, and decreases in time.

The conclusion that $\eta \sim m_m/m_w << 1$ is important when viewed on the background of the current literature on thermodynamic models of melt-water interaction. The most influential model was the first [43], in which it was assumed that the mixed state (e) of the present model (Fig. 39) is followed by a reversible and adiabatic expansion executed by the water. The latter is illustrated as the process (e)-(2) in Fig. 65. The Hicks and Menzies model has led to efficiencies of the order of 30 percent, which are practically independent of the mass ratio m_m/m_w. This is why the 30-percent efficiency is mentioned in the literature without any reference to the value of m_m/m_w. For example, Turland and Dobson [41] remind us that the efficiency is given by the expression $1 - (P_0/P_2)^{(k-1)/k}$, where P_e and P_0 are the end pressures (Fig. 65) and $k = c_P/c_v$ in the ideal gas model used for water. If we substitute $P_e/P_0 \sim 10$ and $k = 1.18$ into this expression we obtain an efficiency of 0.3.

It pays to take an even closer look at the Hicks and Menzies model by using the notation employed in section 5. In Fig. 65 it is assumed that m_m is an incompressible substance that remains single-phase from T_i to T_e. The specific heat of this substance is c_m. The water behaves as an ideal gas with constant specific heats c_P and c_v during the entire process (i)-(e)-(2). According to this model, the first-law analysis of the process (i)-(e) yields

$$\frac{P_e}{P_0} = \frac{T_e}{T_0} = \frac{\mu \tau_i + 1}{\mu + 1} \tag{161}$$

where $\mu = m_m c_m/(m_w c_v)$ and $\tau_i = T_i/T_0$. The work performed on the environment by m_w during the reversible and adiabatic expansion (e)-(2) is

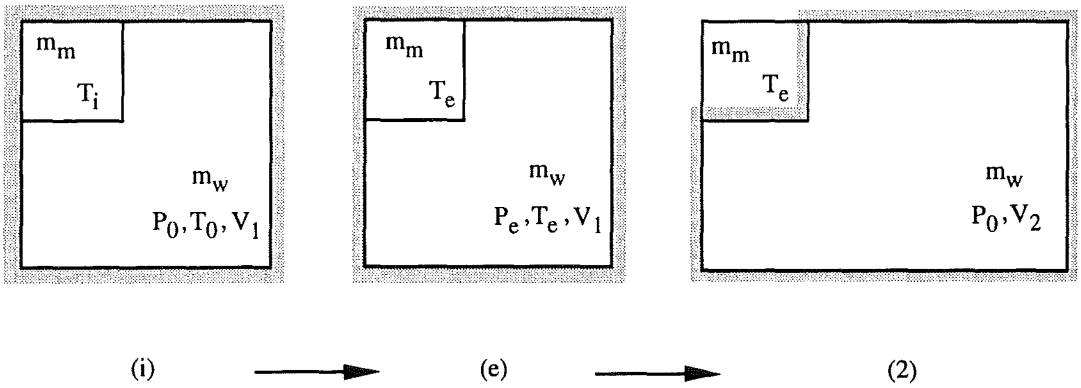

Figure 65. Model in which the water content expands isentropically and adiabatically beyond the thermal mixing modeled in Fig. 39.

$$W_{e-2} = \frac{m_w R T_e}{k-1}\left[1-\left(\frac{\mu+1}{\mu\tau_i+1}\right)^{(k-1)/k}\right] \tag{162}$$

The 30-percent efficiency mentioned above is defined by dividing W_{e-2} by the initial excess energy of the melt, $m_m c_m$ $(T_i - T_0)$. We make the observation that in view of the present exergy analysis it is more appropriate to define the Hicks and Menzies efficiency based on the initial exergy, which is all due to the melt at state (i), $\Xi_i = m_m c_m T_0(\tau_i - 1 - \ln \tau_i)$:

$$\eta'' = \frac{W_{e-2}}{\Xi_i} = \frac{\mu\tau_i+1}{\mu(\mu+1)(\tau_i-1-\ln\tau_i)}\left[1-\left(\frac{\mu+1}{\mu\tau_i+1}\right)^{(k-1)/k}\right] \tag{163}$$

This expression has been plotted in Fig. 66 for k = 1.3. Through the heat capacity ratio μ, the mass ratio m_m/m_w has practically no effect on η'' when $m_m/m_w << 1$. As pointed out by

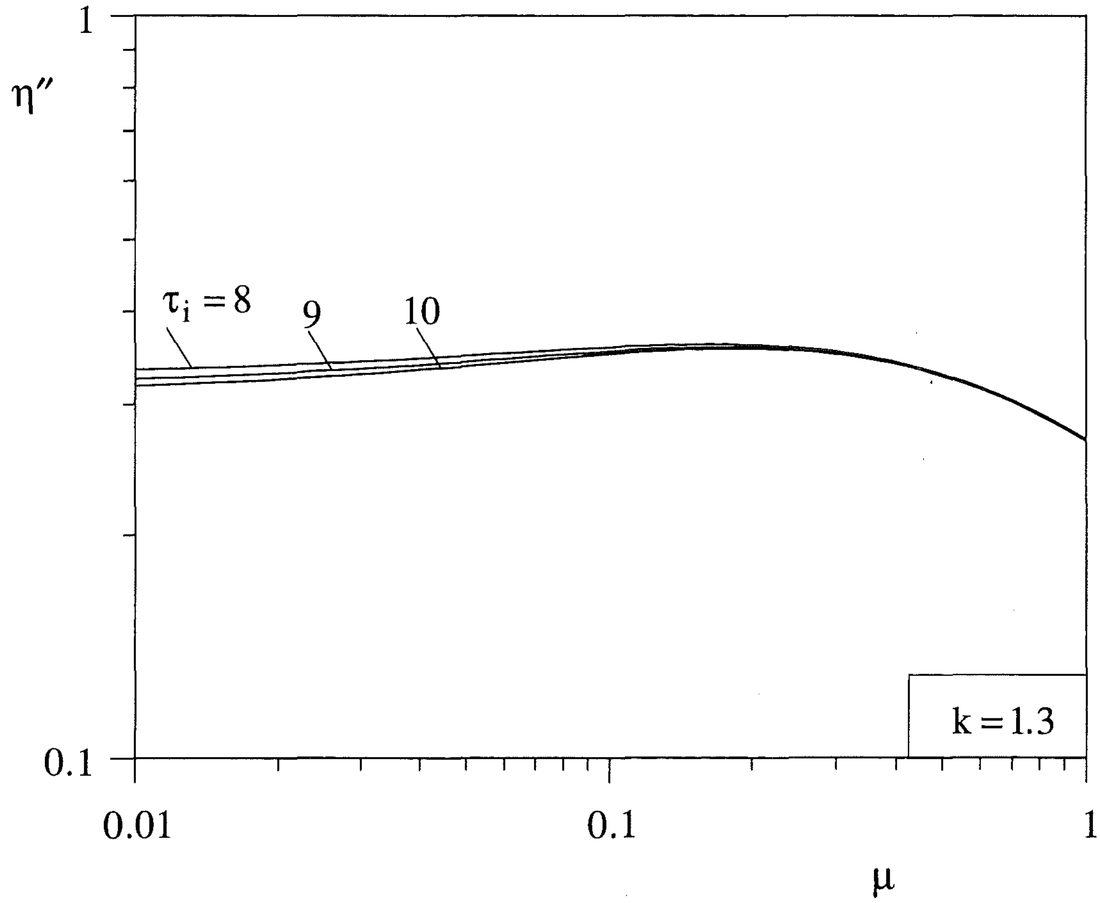

Figure 66. The energy conversion efficiency according to the model of Fig. 65.

Hall [44], the high values maintained by η'' in this range are due to the unrealistic assumption that the water expands isentropically from (e) to (2). This observation served as a starting point for more recent models [44, 45] that brought the efficiency curve down to values and trends comparable to those of Figs. 44-47 in the limit $m_m/m_w << 1$. Once again, exergy analysis led us not only to the theoretical ceiling, but also did away with the need to model the processes that may occur beyond state (e). Exergy analysis served the additional purpose of reminding us that the proper efficiency definition is the exergy-based Eq. (108), and that the definitions of efficiencies such as η'' vary in accordance with the assumed features of the model.

Publications

O. Craciunescu, A. Bejan, D. G. Cacuci and W. Schütz, Time-Dependent Interaction between Water at Supercritical Pressures and a Hot Surface, *Num. Heat Transfer, Part A*, vol. 30, pp. 535-553, 1996.

A. Bejan, N. Dan, D. G. Cacuci and W. Schütz, On the Thermodynamic Efficiency of Energy Conversion during the Expansion of a Mixture of Hot Particles, Steam and Liquid Water, *Energy—the Int. J.*, vol. 22, 1997, to appear.

N. Dan, A. Bejan, D. G. Cacuci and W. Schütz, The Evolution of a Mixture of Hot Particles, Steam and Water Immersed in a Water Pool, *Num. Heat Transfer, Part A*, vol. 32, 1998, submitted.

A. Bejan, N. Dan, D. G. Cacuci and W. Schütz, Exergy Analysis of Energy Conversion during the Thermal Interaction between Hot Particles and Water," *Energy—the Int. J.*, vol. 23, 1998, submitted.

REFERENCES

1. A. Inoue, M. Takahashi and M. Matsuzaki, Transient Film Boiling under Transient Conditions Related to Vapor Explosions (Effects of Transient Flow and Fragmentation under the Shock Pressure), *Proc. Int. Seminar Physics Vapor Explosions*, pp. 27-38, Tomakomai, Japan, Oct. 25-29, 1993.
2. C. C. Chu and M. L. Corradini, One-Dimensional Transient Fluid Model for Fuel/Coolant Interaction Analysis, *Nuclear Sci. Eng.*, vol. 101, pp. 48-71, 1989.
3. M. L. Corradini, B. J. Kim and M. D. Oh, Water Explosions in Light Water Reactors: A Review of Theory and Modeling, *Progr. Nuclear Energy*, vol. 22, pp. 1-117, 1988.
4. G. Berthoud, Progress Made in the Area of Molten Fuel Coolant Interaction, *FISA-95 Symposium, EU Research on Severe Accidents*, pp. 119-139, Luxemburg, Nov. 20-22, 1995.

5. F. Huber, A. Kaiser, W. Schütz, M. Steinbrück and H. Will, Experimental Investigation of the Premixing Behavior of a Hot Melt Poured into Water, *Thermophysics 95*, Obninsk, Russia, Nov. 21-24, 1995.

6. C. Hirsch, *Numerical Computation of Internal and External Flows*, Wiley, New York, 1991.

7. Y. Huang and H. Bau, Thermoacoustic Waves in a Semi-Infinite Medium, *Int. J. Heat Mass Transfer*, vol. 38, pp. 1329-1345, 1995.

8. R. Melnikoff and B. Plohr, The Riemann Problem for Fluid Flow of Real Materials, *Rev. Mod. Phys.*, vol. 68, pp. 75-130, 1989.

9. H. Steiner and W. Gretler, The Propagation of Spherical and Cylindrical Shock Waves in Real Gases, *Phys. Fluids*, vol. 6, pp. 2154-2164, 1994.

10. P. Glaister, An Efficient Flux Difference Splitting Algorithm for Unsteady Duct Flows of a Real Gas, *Appl. Num. Math.*, vol. 15, pp. 27-52, 1994.

11. D. Drikakis and S. Tsangaris, Real Gas Effect for Compressible Nozzle Flows, *J. Fluids Eng.*, vol. 115, pp. 115-120, 1993.

12. M. Murakami and K. Iwashita, Numerical Computation of a Thermal Shock Wave in He II, *Computers & Fluids*, vol. 19, pp. 443-451, 1991.

13. I. Toumi, A Weak Formulation of Roe's Approximate Riemann Solver, *J. Comp. Phys.*, vol. 102, pp. 360-373, 1992.

14. W. -T. Lee, Local Preconditioning of the Euler Equations, Ph.D. Thesis, University of Michigan, Ann Arbor, 1992.

15. P. Roe, Some Contributions to the Modelling of Discontinuous Flows, *Lectures Appl. Math.* vol. 22, pp. 163-191, 1985.

16. P. Roe, Characteristic-Based Schemes for the Euler Equations, *Annual Rev. Fluid Mech.*, vol. 18, pp. 337-365, 1986.

17. S. Osher and S. Chakravarthy, Upwind Schemes and Boundary Conditions with Applications to Euler Equations in General Geometries, *J. Comp. Phys.*, vol. 50, pp. 447-481, 1983.

18. P. W. Hemker and S. P. Spekreijse, Multiple Grid and Osher's Scheme for the Efficient Solution of the Steady Euler Equations, *Appl. Num. Math.*, vol. 2, pp. 475-493, 1986.

19. P. Sweby, High Resolution TVD Schemes Using Flux Limiters, *Lectures Appl. Math.*, vol. 22, pp. 2889-3009, 1985.

20. J. M. Corberan and M. L. Gascon, TVD Schemes for the Calculation of the Flow in Pipes of Variable Cross-Section, *Math. Comp. Modelling*, vol. 21, pp. 85-92, 1995.

21. M. Vinokur, Flux Jacobian Matrices and Generalized Roe Average for an Equilibrium Real Gas, NASA-CR-177512, 1988.

22. M. Vinokur and J. L. Montagne, Generalized Flux-Vector Splitting and Roe Average for an Equilibrium Real Gas, *J. Comp. Phys.* vol. 89, pp. 276-300, 1990.

23. P. Collela and H. M. Glaz, Efficient Solution for the Riemann Problem for Real Gases, *J. Comp. Phys.*, vol. 59, pp. 264-288, 1985.

24. J. L. Montagne, H. C. Lee and M. Vinokur, Comparative Study of High-Resolution Shock-Capturing Schemes for a Real Gas, *AIAA J.*, vol. 27, pp. 1332-1346 (1988).

25. R. Abgrall, An Extension of Roe's Upwind Scheme to Algebraic Equilibrium Real Gas Models, *Computers and Fluids*, vol. 19, pp. 171-182, 1991.

26. R. Saurel, M. Larini and J. C. Loraud, Exact and Approximate Riemann Solvers for Real Gases, *J. Comp. Phys.*, vol. 112, pp. 126-137, 1994.

27. L. Haar, J. Gallagher and G. Kell, *Steam Tables. Thermodynamic and Transport Properties and Computer Programs for Vapor and Liquid States of Water in SI Units*, Hemisphere, Washington, DC, 1984.

28. P. Dierckx, *Curve and Surface Fitting with Splines*, Clarendon Press, Oxford, 1993.

29. F. N. Fritsch and R. E. Carlson, Monotone Piecewise Cubic Interpolation, *SIAM J. Num. Analysis*, vol. 17, pp. 238-246, 1980.

30. F. N. Fritsch and J. Butland, A Method for Constructing Local Monotone Piecewise Cubic Interpolants, *SIAM J. Sci. Stat. Comp.*, vol. 5, pp. 300-304, 1984.

31. R. Seydel, Tutorial on Continuation, *Int. J. Bifurcation Chaos*, vol. 1, no. 1, pp. 3-11, 1991.

32. D. Kincaid and W. Cheney, *Numerical Analysis*, Brooks Cole Publishing Co., Pacific Grove, CA, 1990.

33. C. A. J. Fletcher, *Computational Techniques for Fluid Dynamics*, Springer Verlag, Berlin, 1991.

34. D. Poulikakos, *Conduction Heat Transfer*, Prentice Hall, Englewood Cliffs, NJ, 1994.

35. A. Bejan, *Heat Transfer*, Wiley, New York, 1993.

36. W. H. Press, S. A. Teukolsky, W. T. Vetterling, and B. P. Flannery, *Numerical Recipes in C*, University Press, Cambridge, UK, 1992.

37. T. Nakayama, A Computational Method for Simulating Transient Motions of an Incompressible Inviscid Fluid with a Free Surface, *Int. J. for Num. Methods in Fluids*, vol. 10, pp. 683-695, 1990.

38. D.A. Anderson, J.C. Tannehill, R.H. Pletcher, Computational Fluid Mechanics and Heat Transfer, Hemisphere, New York, 1984.

39. O. Craciunescu, A. Bejan, D. G. Cacuci and W. Schütz, Time-Dependent Interaction between Water at Supercritical Pressures and a Hot Surface, *Num. Heat Transfer, Part A*, vol. 30, pp. 535-553, 1996.

40. A. Bejan, *Advanced Engineering Thermodynamics*, Wiley, New York, 1988.

41. B. D. Turland and G. P. Dobson, *Molten Fuel Coolant Interactions: A State of the Art Report*, Report EUR 16874, European Commission, Luxembourg, 1996.

42. F. Huber, A. Kaiser, M. Steinbrück and H. Will, *PREMIX, Documentation of the Results of Experiments PM01 to PM06*, Report FZKA 5756, Forschungszentrum Karlsruhe, 1996.

43. E. P. Hicks and D. C. Menzies, Theoretical Studies on the Fast Reactor Maximum Accident, *Proc. Conf. Safety, Fuels, and Core Design in Large Fast Power Reactors*, Report ANL-7120, Argonne National Laboratory, Argonne, IL, pp. 654-670, 1965.

44. A. N. Hall, Outline of a New Thermodynamic Model of Energetic Fuel-Coolant Interactions, *Nuclear Eng. Design*, vol. 109, pp. 407-415, 1988.

45. D. D. Cline, L. T. Pong, D. F. Beck and M. Berman, An Equation of State Formulation for Hicks-Menzies FCI Efficiencies, *AIChE Symp. Ser. 269*, vol. 85, pp. 48-53, 1989.